Autre référence / Other reference :
HYDRA_LAPLACE
Type :
Rapport d'essai final/qualification/validation.
Description :
HAS2 electron test report
Titre du document / Title of document :
HAS2 electron test report

	Noms Names	Dates
Etabli par Prepared by	BEAUMEL Matthieu HERVE Dominique	07/10/2011
Vérifié par Checked by	MALARD Loic	10/10/2011
Approuvé par Approved by	HERVE Dominique ; TENAILLE Patrick	10/10/2011
Approbation client Customer approval	-	-

REPERTOIRE DES MISES A JOUR / *CHANGE RECORD*	
Revision	Description of change
A	First issue (sequence 8)
A	Second issue (sequence 12) - results after 12 weeks room temperature added (mean dark current and DSNU) - results after 12 weeks room temperature + 4 weeks at 50°C annealing added (mean dark current and DSNU)

TABLE OF CONTENTS

1. SCOPE AND APPLICABILITY 5
1.1. SCOPE 5
1.2. PURPOSE 5
2. REFERENCES 5
2.1. APPLICABLE DOCUMENTS 5
2.2. REFERENCE DOCUMENTS 5
3. ABBREVIATIONS 6
4. HAS2 PRESENTATION 7
5. TEST SETUP 8
5.1. FACILITY 8
5.2. DOSIMETRY 9
5.2.1. Cumulative irradiation 9
5.2.2. Rate of irradiation 10
5.3. TEST BENCH 13
6. CUMULATIVE EFFECTS TEST CAMPAIGN 15
6.1. TEST DESCRIPTION 15
6.2. TESTED SAMPLES 15
6.3. TESTED PARAMETERS 15
6.4. RUN LIST 15
6.5. TEST METHODS 16
6.5.1. Temporal noise DR and NDR mode 16
6.5.2. Offset in DR and NDR mode 17
6.5.3. Fixed Pattern Noise FPN global and local in DR mode 17
6.5.4. Fixed Pattern Noise FPN local in NDR mode 17
6.5.5. Mean Dark current 17
6.5.6. Dark signal non-uniformity (DSNU) 18
6.5.7. Distribution of hot pixels (spikes) 18
6.6. WINDOWED NDR MODE ADDRESSING SCHEME 18
6.7. SPECIFIC ISSUES 19
6.7.1. Dark current gradient 19
6.7.2. Annealing 19
6.7.3. Temporal noise and FPN performances 19
6.8. CUMULATIVE TEST RESULTS SUMMARY 20
6.9. DETAILED TEST RESULTS 21
6.9.1. NDR reference level 21
6.9.2. Temporal noise NDR 22
6.9.3. FPN NDR 23
6.9.4. Column FPN NDR 24

6.9.5. Pixel FPN NDR 25
6.9.6. Mean offset DR 26
6.9.7. Temporal noise DR 27
6.9.8. Global FPN DR 28
6.9.9. Local FPN DR 29
6.9.10. Local column FPN DR 30
6.9.11. Mean even - Mean odd DR 31
6.9.12. Local pixel FPN DR 32
6.9.13. Column FPN corrected pre-rad 33
6.9.14. Local DSNU 35
6.9.15. Global DSNU 36
6.9.16. Mean dark current 37
6.9.17. Dark current images and histograms in full frame DR mode 38

7. SINGLE EVENT EFFECTS TEST CAMPAIGN 53

7.1. TESTED SAMPLES 53
7.2. RUN LIST 53
7.3. SINGLE EVENT TRANSIENTS 56
7.3.1. Methodology 56
7.3.2. Experimental data 57
7.3.3. Analysis 67
7.4. SECONDARY PHOTONIC EFFECTS 91
7.4.1. Methodology 91
7.4.2. Order of magnitude of the expected signal 93
7.4.3. Experimental data and analysis 95

8. CONCLUSIONS 96

1. SCOPE AND APPLICABILITY

1.1. Scope

This test report presents the result of the electron irradiation of the HAS2 CMOS image sensor. The study is aimed at evaluating the robustness of HAS2 detector to the radiation environment of Laplace mission STR. The radiation test campaign is performed in the frame of ESA contract N°40001011530/10/NL/AF.

1.2. Purpose

Two radiation aspects are addressed:

- Electron-induced cumulative effects (Total Ionizing Dose and Displacement Damage Dose),
- Electron-induced single event effects (transient effects and secondary photonic effects).

The analysis of the transient effects test results is supported by simulations based on analytical and Monte-Carlo transport code.

2. REFERENCES

2.1. Applicable documents

[AD 1] HAS Electron Test Plan, PE__00005191, A

2.2. Reference documents

[RD 1] ON Semiconductor HAS Detailed Specification ICD, v. 3.6
APS2-CY-FOS-06-004
STA_00001151, A

[RD 2] HYDRA_LAPLACE D2 - STR model / Simulator Description
RP__00001767, A

[RD 3] HYDRA_LAPLACE D4 - Single Event Phenomena Effects on the STR
RP__00001732, A

[RD 4] NIST ESTAR – stopping power and range tables for electrons, http://physics.nist.gov/PhysRefData/Star/Text/ESTAR.html

3. ABBREVIATIONS

AD	Applicable Document
APS	Active Pixel Sensor
CDS	Correlated Double Sampling
CMOS	Complementary Metal-Oxide Semiconductor
DC	DateCode
DDD	Displacement Damage Dose
DR	Destructive Readout
DS	Double Sampling
DSNU	Dark Signal Non Uniformity
ECSS	European Cooperation for Space Standardization
EOL	End Of Life
PFA	Focal Plane Array
FPN	Fixed Pattern Noise
HAS2	High Accuracy STR 2
LSB	Least Significant Bit
N/A	Not Applicable
NIEL	Non-Ionizing Energy Loss
NDR	Non-Destructive Readout
PCB	Printed Circuit Board
RD	Reference Document
SEE	Single Event Effect
SET	Single Event Transient
SEU	Single Event Upset
STR	Star TrackeR
TID	Total Ionizing Dose
UM	Monitor Unit (Unité Moniteur)

4. HAS2 PRESENTATION

The Accuracy STR 2 sensor (HAS2) is a 1024 x 1024 pixel rolling shutter Active Pixel Sensor (APS), featuring a programmable (gain and offset) output amplifier (PGA) and an internal 12 bits ADC. The CMOS image was sensor designed and manufactured by ON Semiconductor[1] under ESA contract 17235/03/NL/FM for star tracker applications. The simplified block diagram of HAS2 is presented in Figure 4-1.

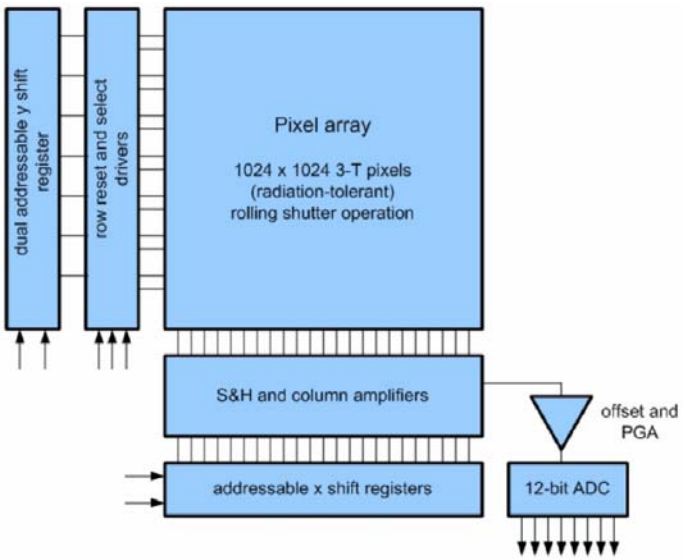

Figure 4-1 : HAS2 block diagram

Pixel design is based on a photodiode coupled with a three transistor readout circuit. The HAS2 is the descendant from a lineage radiation-hardened by design sensors from ON Semiconductor: the photodiodes includes a doped surface protection layer to prevent the depleted area from reaching the field oxide interface, while the CMOS readout circuitry is designed using enclosed geometry transistor layouts. The wafers are produced by Plessey Semiconductors[2] on the standard XC035P311 CMOS process (0.35 µm).

In order to reduce the variation in signal offset from pixel to pixel (known as Fixed Pattern Noise, or FPN) typically seen on APS, the HAS2 implements two different noise reduction techniques: Double Sampling (DS) also called Destructive Readout (DR) and Correlated Double Sampling (CDS) also called Non Destructive Readout (NDR). In DR mode, the pixel is reset at the end of the signal integration time in order to sample the pixel reference level. The reference level is subtracted from the signal level in order to cancel the pixel offset. This internal analog operation is performed before digitization. In NDR mode, two images are sampled and digitized: a reference image at the beginning of the integration time, and a signal image at its end. Offset correction must be performed off-chip by subtracting these two images.

A temperature sensor is also integrated on chip, which can be addressed through an internal multiplexer.

[1] Formerly Cypress BVBA and Fillfactory.
[2] Formerly X-FAB.

5.TEST SETUP

5.1.Facility

The irradiations in this study were performed with the CLINAC 1 medical radiation therapy machine from the Curie Institute in Paris. The institute is exclusively devoted to the research and the treatment of cancer via nuclear medicine.

The CLINAC 1 is a CLINAC 2300 C/D linear accelerator from Varian. The accelerator can be configured to provide pulsed electron beams of various energies, or X-rays generated by a Bremsstrahlung process.

The accelerator can be freely tilted around its X-axis.

Figure 5-1 : CLINAC 1 irradiation chamber (horizontal beam)

The figure hereafter presents the geometry of the electron accelerator:

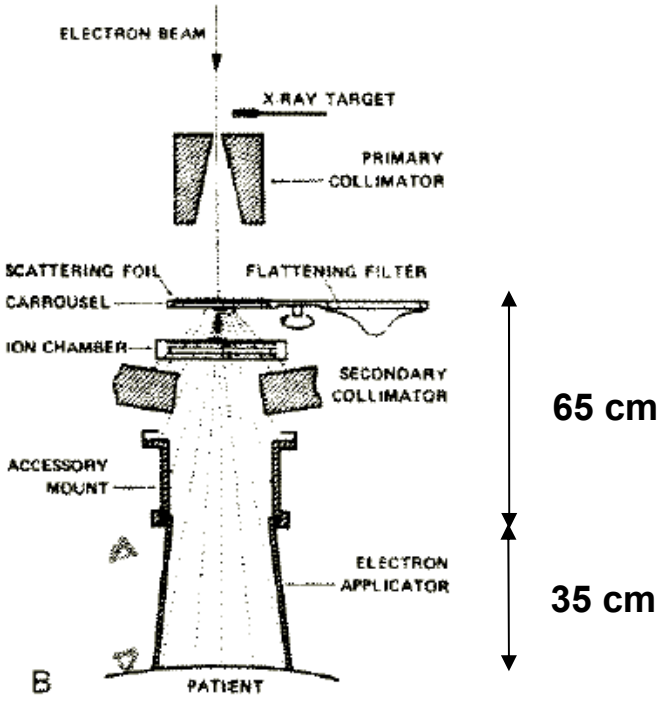

Figure 5-2 : Geometry of the electron accelerator

After being accelerated, the initial narrow electron beam is scattered by a lead foil. The point of impact of the electrons on the lead foil acts as a source point for the scattered beam.

Several elements collimate the scattered beam:
- a secondary collimator
- a removable applicator with different field sizes

The distance between the scattering foil and the end of the applicator is 95 cm. The patient is positioned 5 cm away from the applicator end.

Two ionization chambers are used to control in real-time the applied dose.

In this study, a 10 x 10 cm applicator was used, along with 12 MeV and 22 MeV electron beams. The applied dose rates were a dose rate of 1 Gy[water]/min or 10 Gy[water]/min.

5.2.Dosimetry

5.2.1.Cumulative irradiation

The CLINAC 1 is calibrated to deliver the intended dose level at a reference depth in a water phantom. This reference depth corresponds to the position at which the deposited dose reaches its peak. The dosimetry reported back by the CLINAC monitoring instruments is directly valid only in this position.

The calibration of the CLINAC 1 is carefully controlled to ensure the safety of the patients. Every day, a check is performed before the start of the medical treatments. The procedure consists in irradiating an ionization chamber in reference conditions, and comparing the

measurements with the output of the accelerator monitoring instruments. The cumulative dosimetry of the accelerator is therefore considered to be known with a high accuracy, within 2%.

As the human body is mostly made of water, dosimetry at the Curie institute is always made in a water medium. The units used are:

- Gy[water]/min (100 rad[water]/min)
- Monitor Units (UM). 1 UM corresponds to 0.01 Gy[water] (1 rad[water])

These units need to be converted to an electron fluence on the sensors positioned 5 cm away from the applicator end. The full conversion process is described in [AD 1], and gives the following results:

	12 MeV beam	22 MeV beam
CLINAC 1 dosimetry report	1 UM	1 UM
Deposited dose at peak in water	0.01 Gy[water]	0.01 Gy[water]
Deposited dose at peak in silicon	0.00937 Gy[Si]	0.00937 Gy[Si]
Fluence at detector surface	2.67×10^7 e-/cm^2	2.63×10^7 e-/cm^2
Flux uncertainty	± 11.7 %	± 11.1 %

Table 5-1: CLINAC 1 dosimetry conversion

The presented uncertainty includes the initial CLINAC 1 calibration accuracy, bias errors in the unit conversion process, and the effect of beam non-uniformity. It should be considered as a worst case.

5.2.2.Rate of irradiation

Depending on the beam energy and dose rate, the electron flux produced by the CLINAC 1 is pulsed at a frequency between 15 and 180 Hz, with a varying duty cycle. While the dose rate can be set, there is no direct feedback on the pulse rate and electron fluence per pulse.

In order to control the dose rate and the pulse frequency, we performed several preliminary calibration runs with HAS2 sensors exposed to the electron beam. The rolling shutter integration scheme of the sensor gives temporal information on the beam.

In full frame DR mode, the rolling shutter scans the image in 271.3 ms (265.05 µs per line). Beam pulses will appear as horizontal stripes on the recorded images. The number of lines between the start of two stripes correspond to the time duration between two pulses. The width of the stripes corresponds to the integration time used. An example of the recorded images at 1 Gy/min is presented in Figure 5-3 for an integration time of 130 lines (34.5 ms). It can be seen that the pulse rate is roughly the same for 12 and 22 MeV beams (same number of lines between two pulses), while the duty cycle of the accelerator is different (there is a missing pulse on the 22 MeV image).

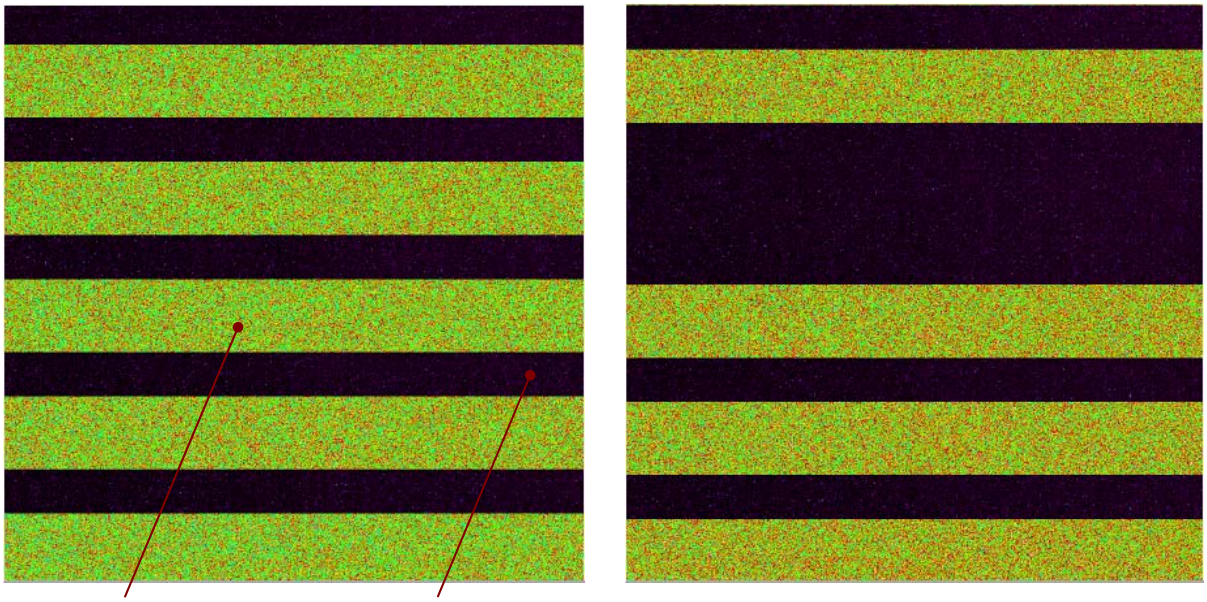

Figure 5-3: Full frame DR image 100 UM/min at 12 MeV (left side), 22 MeV (right side)

The first verification is to control the average dose rate, which can be assessed from the precise measurement of the beam time. The measurement has been performed for every run aimed at the characterization of single event effects. The results show an excellent stability of the average dose rate between irradiations, as presented in Table 5-2:

	Dose rate set-up	Dose set-up	Energy	Measured beam time	Computed dose rate
RUN 28, 0° tilt	100 UM/min	10 UM	12 MeV	6.16 s	97.4 UM/min
RUN 31, 0° tilt	100 UM/min	10 UM	22 MeV	6.03 s	99.5 UM/min
RUN 34, 28.8° tilt	100 UM/min	10 UM	12 MeV	5.90 s	101.7 UM/min
RUN 37, 28.8° tilt	100 UM/min	10 UM	22 MeV	6.03 s	99.5 UM/min
RUN 32, 0° tilt	1000 UM/min	100 UM	12 MeV	6.00 s	1000 UM/min
RUN 33, 0° tilt	1000 UM/min	100 UM	22 MeV	5.99 s	1001.7 UM/min
RUN 38, 28.8° tilt	1000 UM/min	100 UM	12 MeV	5.98 s	1003.3 UM/min
RUN 39, 28.8° tilt	1000 UM/min	100 UM	22 MeV	5.97 s	1005 UM/min

Table 5-2: CLINAC 1 beam time and dose rate in different configurations (expected beam time: 6.00s)

The CLINAC 1 dose rate setting is consistent with the average dose rate measured by 1.23 % (1 σ). It can be directly used without further analysis.

The analysis of the signal in the different stripes gives information on the delivered fluence during each electron pulse. At the beginning of an irradiation, the pulse intensity quickly rises up to a constant plateau. Typically, the 10 first pulses are weaker than the other ones, as can be seen in Figure 5-4. These abnormal pulses have been excluded from the analysis.

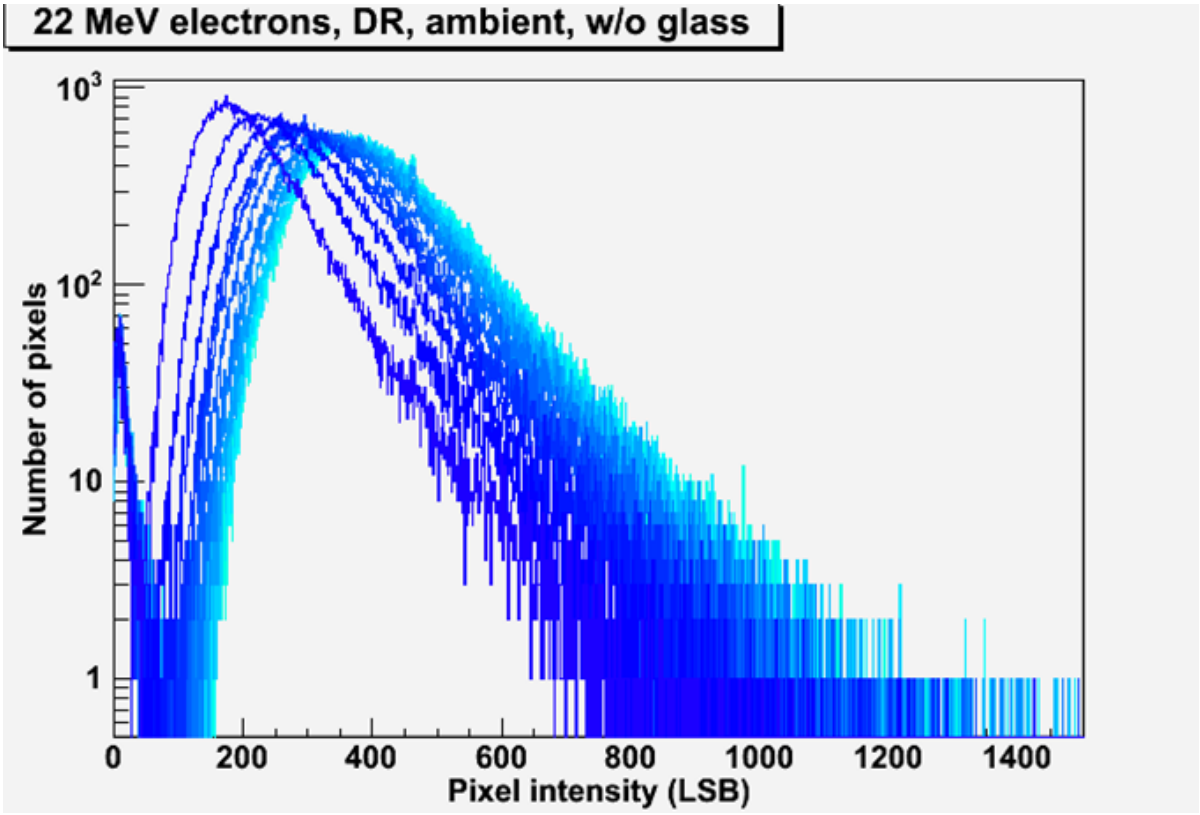

Figure 5-4 : Pulse ramp-up at 22 MeV. First pulses in violet/dark blue

Finally, we can compute the electron fluence per pulse delivered by the accelerator when the plateau is reached. The average time number of lines between two pulses is computed on a six second run (lasting about 23 images). This allows us to assess:

- the average time between two pulses: $T = N_{lines} \times 265.05\ \mu s$
- the electron fluence in a pulse: $F = \Phi \times T$

in which Φ is the average electron flux, computed from the results presented in Table 5-1 (number of electrons per UM) and Table 5-2 (UM per minute).

This operation allows an accurate assessment of the average number of electron hits per pixel and per pulses. It has been performed for the different accelerator configurations used in the study. The numbers in Table 5-3 are valid for a device under test positioned 5 cm away from the applicator end.

	Dose rate set-up	Energy	Average time between pulses	Fluence per pulse
RUN 3	100 UM/min	12 MeV	56.4 ms	2.51E6 e-/cm²
RUN 4	100 UM/min	22 MeV	62.0 ms	2.72E6 e-/cm²
RUN 5	1000 UM/min	12 MeV	6.2 ms	2.76E6 e-/cm²
RUN 7	1000 UM/min	22 MeV	6.4 ms	2.81E6 e-/cm²

Table 5-3: CLINAC 1 electron fluence per pulse for different configurations

5.3.Test bench

The test bench used for this study was designed by ON Semiconductor on specifications from Sodern. The test equipment is made to operate the sensors directly under the electron beam, as shown in the following figure:

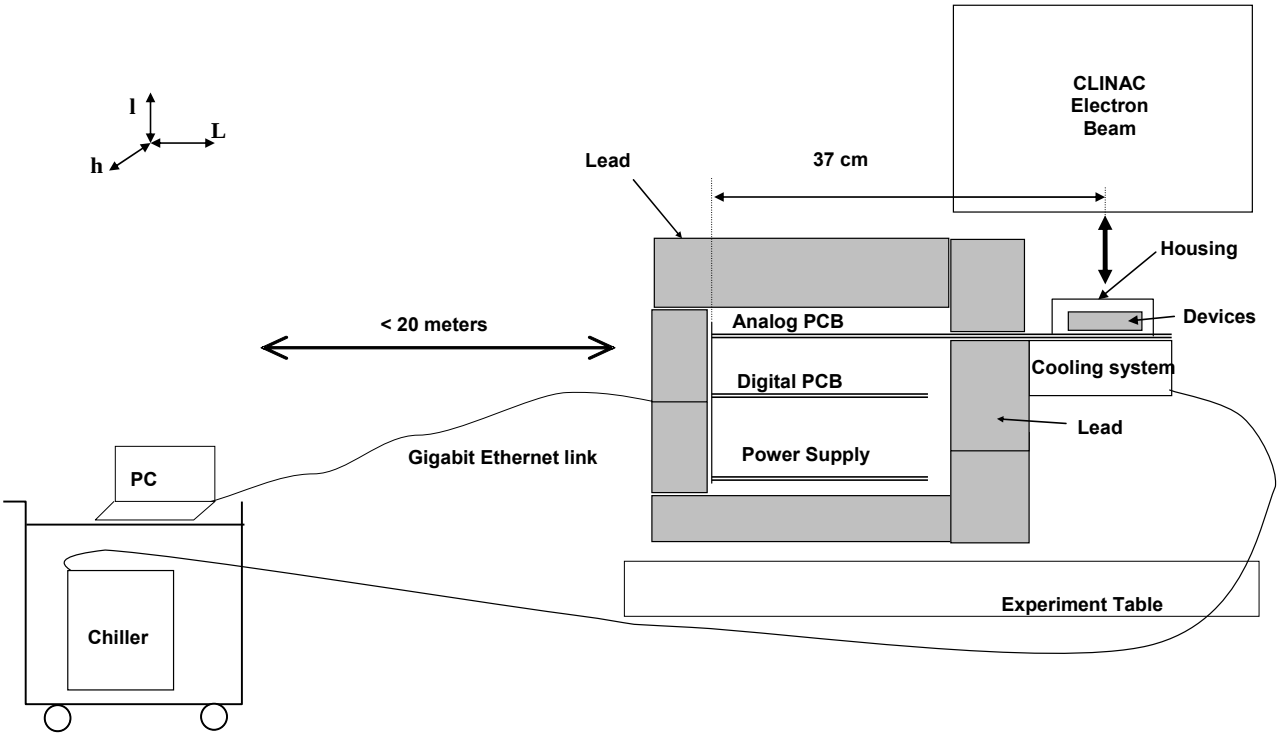

Figure 5-5: Overview of the test bench

This tester has the capabilities to drive 3 samples in parallel. Therefore, up to 3 samples can be submitted to irradiation at the same time. The output data from the samples are buffered so that the 3 devices under test can be characterized separately. The pixel reset is performed according to Hard To Soft timing control. The detector can be operated whether in DR mode of NDR mode. The digitized output is given on 12 bits. The conversion factor between the ADC output and the amount of electron generated inside the pixel is 20 electrons/LSB.

Live images can be grabbed while electron beam is ON (~ 4Hz frame rate acquisition in full frame DR mode). For cumulative testing, characterization of offsets and dark current parameters can be performed in darkness right after turning OFF the beam flux according to automatic sequences applied by the tester.

The cooling system is based on Peltier modules connected to a base plate via aluminium fingers. The base plate itself is cooled with a low temperature fluid pumped by a chiller.

The cable between the control computer and the test bench is a 20 meter long Ethernet link.

The test equipment was surrounded by lead bricks to protect the unhardened driving electronics. The shield was 10 cm thick on the side exposed to the beam, and 5 cm thick on the other sides. For reference, the gamma attenuation factor is 1000 for a lead shield of 10 cm. A wall close to the experiment table was protecting the autonomous power supply and the chiller.

The emerging part with the detector sockets was placed in front of the beam axis represented by a laser pattern. The set-up is presented in the following figure:

Figure 5-6 : Test bench irradiated with a normal (left) and 28.2° tilted (right) electron beam

The whole test chamber was placed in darkness to avoid any perturbation of the electro-optical measurements.

6.CUMULATIVE EFFECTS TEST CAMPAIGN

6.1.Test description

Inputs for this work are the electron TID and DDD worst case levels calculated for Laplace mission including an RDM of 2.

Three HAS devices have been irradiated at room temperature using 12 MeV electron beam up to 340 Gy[Si] (34 krad) with intermediate characterization steps performed on site at 40, 100, 200 Gy[Si]. Irradiation dose rate was around 4.5e+08 electrons/cm²/s which corresponds to a dose rate of 9.37 Gy[Si]/min.

During irradiation, the HAS devices are operated in NDR mode (nominal mode of operation when STR is in tracking mode). The characterisations are performed on site in darkness after putting off the electron beam. No test under illumination are performed (previous proton and total dose testing performed in the frame of ESA evaluation contract have shown that photo response related parameters were not affected by irradiation).

Annealing behavior is investigated by characterizing the 3 detectors during 8 weeks after irradiation at SODERN. Annealing is performed at room temperature (19°C) with parts running in NDR mode, except one part which has been biased OFF after 62 hours anneal.

6.2.Tested samples

The 3 devices are HAS2 Engineering Models of Date Code DC1102 (wafer lot P29506.1). The parts are all from the same wafer lot. Serial numbers of the devices are #589 (named detector D1), #595 (named detector D2), #605 (named detector D3).

6.3.Tested parameters

The measured parameters in both DR and NDR mode are listed below (automated characterization sequence for the 3 devices):

- Internal temperature sensor output
- Temporal noise in DR and NDR mode
- Offsets in DR and NDR mode
- FPN local and global in DR mode
- FPN local in NDR mode
- Dark current in NDR mode
- DSNU local and global in DR mode
- Distribution of hot pixels - dark current histogram

Radiation test and characterization are performed at room temperature (19°C).

6.4.Run list

For cumulative effects characterization, the runs presented in Table 7-1 were performed.

In the table, every run listed as “auto” mode used the automated test sequence described in section 6.3. Two additional runs (2 and 3) were made in DR mode to measure the beam spatial uniformity.

Last annealing step (4 weeks) was performed with parts stored at 50°C.

Run	DUT	Mode	Integ. Time	Image #	Temp. (°C)	Energy (MeV)	Dose rate (UM/min)	Dose (UM)	Cumulated (UM)	Tilt (°)	Comments
1	All	Auto	Auto	Auto	19	-	-	-	-	-	Charac. at Sodern
2	All	Auto	Auto	Auto	19	12	100	10	10	0	Charac. at Curie
3	1	DR	130	40	19	22	100	10	20	0	Uniformity mes.
4	1	DR	130	40	19	12	100	10	30	0	Uniformity mes.
5	All	Auto	Auto	Auto	19	12	100	4270	4300	0	
6	All	Auto	Auto	Auto	19	12	100	6400	10700	0	
7	All	Auto	Auto	Auto	19	12	100	10600	21300	0	
8	All	Auto	Auto	Auto	19	12	100	15000	36300	0	
9	All	Auto	Auto	Auto	19	-	-	-	36300	-	anneal 20 h
10	All	Auto	Auto	Auto	19	-	-	-	36300	-	anneal 42 h
11	All	Auto	Auto	Auto	19	-	-	-	36300	-	anneal 62 h
12	All	Auto	Auto	Auto	19	-	-	-	36300	-	anneal 1 week
13	All	Auto	Auto	Auto	19	-	-	-	36300	-	anneal 2 weeks
15	All	Auto	Auto	Auto	19	-	-	-	36300	-	anneal 3 weeks
16	All	Auto	Auto	Auto	19	-	-	-	36300	-	anneal 4 weeks
17	All	Auto	Auto	Auto	19	-	-	-	36300	-	anneal 6 weeks
18	All	Auto	Auto	Auto	19	-	-	-	36300	-	anneal 8 weeks
19	All	Auto	Auto	Auto	19	-	-	-	36300	-	anneal 10 weeks
20	All	Auto	Auto	Auto	19	-	-	-	36300	-	anneal 10.3 weeks
22	All	Auto	Auto	Auto	19	-	-	-	36300	-	anneal 11 weeks
23	All	Auto	Auto	Auto	19	-	-	-	36300	-	anneal 12 weeks
28	All	Auto	Auto	Auto	19	-	-	-	36300	-	anneal 16 weeks (4 weeks at 50°C at ESTEC facility)

Table 6-1: Run list for cumulative effects characterization

6.5.Test methods

6.5.1.Temporal noise DR and NDR mode

In DR mode, full frame images are acquired (25 frames grabbed and stored).

In NDR mode, windowed images are acquired (5 windows of 50x50 pixels). 100 frames of black levels and signal levels are grabbed and stored. Subtraction of the signal levels by the corresponding black levels is performed to form 50 successive images.

The noise of the different pixels is considered not correlated, i.e. the pixel values can be corrected for correlated noise (FPN mainly). From two successive images, a pixel-per-pixel subtraction is performed. The noise figure is the root square of the standard deviation of all the pixel values in the FPN-corrected image.

Integration time is 5 ms in both DR and NDR mode.

6.5.2.Offset in DR and NDR mode

Full frame images are acquired in DR mode (25 frames grabbed and stored). Mean signal is calculated in electrons for each images on the whole FPA, on odd columns, and on even columns.

In NDR mode, windowed images are acquired (5 windows of 50x50 pixels). 100 frames of black levels and signal levels are grabbed and stored. Offset is calculated from the mean signal measured on the black levels.

Integration time is 5 ms in both DR and NDR mode.

6.5.3.Fixed Pattern Noise FPN global and local in DR mode

The global Fixed Pattern Noise in DR mode is the standard deviation, calculated on all pixels of the FPA. The local FPN is the average of the standard deviations, calculated inside local windows distributed over the FPA area. Local pixel FPN is the average of the standard deviations, calculated inside local columns distributed over the FPA area. Local column FPN is the average of the local windows standard deviations, calculated with the column mean signal.

Full frame images are acquired in DR mode (25 frames grabbed and stored). The acquired images are averaged in one in order to remove temporal noise. Global FPN, local FPN, pixel and column local FPN are calculated on the resulting image. Local window size is 15x15 pixels.

Integration time is 5 ms.

6.5.4.Fixed Pattern Noise FPN local in NDR mode

Windowed images are acquired in NDR mode. 100 frames of black levels and signal levels are grabbed and stored. After subtraction of the signal level by the corresponding black levels, the 50 resulting images are averaged in one in order to remove temporal noise. Pixel FPN is the average of the standard deviations calculated inside the columns of each window. Column FPN is the average of the each window standard deviations calculated with the columns mean signal.

Integration time is 5 ms.

6.5.5.Mean Dark current

Mean Dark Current is measured in NDR mode with 200 ms integration time. 20 frames of black levels and signal levels are grabbed and stored. After subtraction of the signal level by the corresponding black levels, the 6 resulting images are averaged.

NDR mode is preferred compared to DR mode for measuring this parameter. The reason is that offset correction of DR images (images taken at long integration time corrected with images taken at short integration time) is not resulting in an accurate estimation for irradiated parts.

6.5.6. Dark signal non-uniformity (DSNU)

Dark Signal Non Uniformity measurement consists in measuring the output signal of a large number of pixels in a dark image.

The global DSNU is the standard deviation, calculated on all pixels of the FPA. The local DSNU is the average of the standard deviations, calculated on local windows distributed over the FPA area. The DSNU Local window size is 15x15 pixels.

DSNU measurement is performed in DR mode. Full frame images are acquired. Four full frame images are grabbed and stored at a long integration time of 1.5 seconds.

6.5.7. Distribution of hot pixels (spikes)

The dark current histogram is obtained by measuring the output signal of a large number of pixels in a dark image. Measurement is performed in DR mode. Four full frame images are grabbed and stored at a long integration time of 1.5 seconds.

6.6.Windowed NDR mode addressing scheme

Multiple windows addressing in NDR mode has been set to 5 windows of 50x50 pixels. The selected addresses for each window are detailed below.

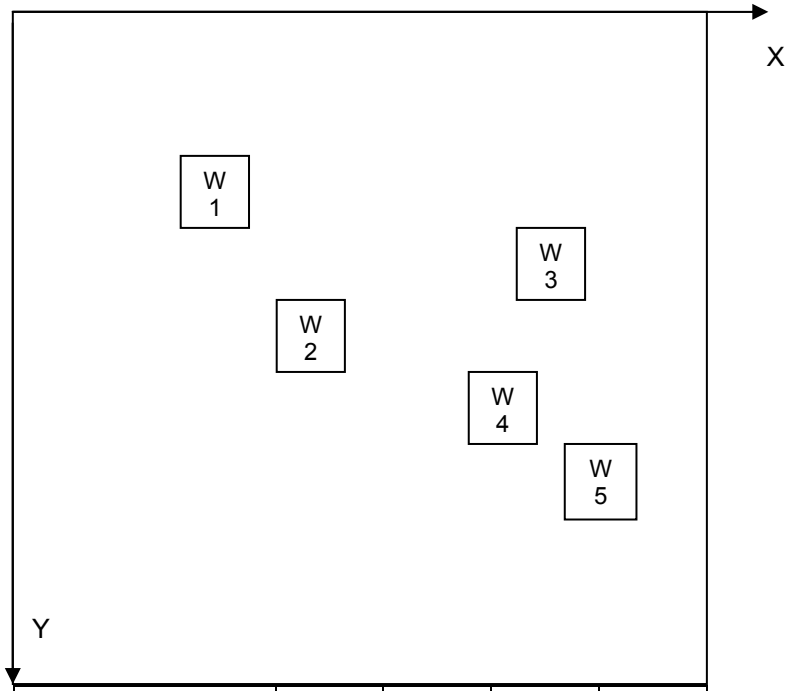

	Xmin	Ymin	Xmax	Ymax
Sub-image 1	315	386	364	435
Sub-image 2	385	486	434	535
Sub-image 3	750	436	799	485
Sub-image 4	727	536	776	585
Sub-image 5	797	586	846	635

Figure 6-1: NDR windows coordinates

6.7.Specific issues and comments

6.7.1. Dark current gradient

Prior to irradiation, the sensors are systematically affected by a gradient within the image. The gradient shape depends on the socket in which the samples are plugged, instead of a specific issue on the samples. The gradient is directly proportional to integration time. At short integration time, this effect is hardly detected.

This behavior cannot be explained by temperature gradient as from column to column rapid variation is observed. In addition, the gradient disappears with irradiation while we should expect the opposite with radiation induced dark current increase.

Further discussion with ON Semiconductor has led to invoke rather a charge injection from the peripheral circuitry toward the pixel array. For instance, a small undershoot on CLK_ADC input could be at the origin of the local signal observed. Difference between the sockets could be explained by a difference in the routing of the PCB and different undershoots between the sockets. Radiation may induce a smoothing effect that could limit the undershoots in the internal circuitry.

Further investigation has not been performed as the impact on performance is small (DSNU performance measured on the tester is close to those obtained on the production tester).

6.7.2.Annealing

The parts have been stored at room temperature biased OFF right after irradiation during 20 hours and then biased ON during 42 additional hours.

Then detector D3 has been switched OFF during 9 weeks.

Then detector D3 has been switched ON and D1 and D2 have been switched OFF during 2 weeks.

For the last step (4 additional weeks at ESTEC facility), the parts have been stored at 50°C with D3 biased OFF and D1-D2 biased ON.

6.7.3.Temporal noise and FPN performances

The temporal noise and FPN performance depends on the socket used for the measurement rather than the samples. This is likely due to the difference in the routing of the PCB which differs between sockets. The FPN performance itself is beyond specification in some cases. However, this does not impact the purpose of the test which is to check radiation induced changes.

6.8.Cumulative test results summary

The cumulative radiation test results are detailed in section 6.9. The gathered data are in line with radiation hardness properties of the HAS2 sensor.

No significant evolution has been observed on:
- Temporal noise,
- FPN (except FPN affected by odd and even offset increase),
- Internal temperature sensor output.

The parameters affected by irradiation are the following
- Dark current,
- Dark current Non Uniformities,
- Odd even offset increase in DR mode,
- Mean offsets.

Mean dark current increase is 121.4 e/s/krad (to be compared with 166 e/s/krad obtained for wafer lot P20291.1 at 25°C).

Dark current Non Uniformities increase is 23.6 e/s/krad (to be compared with 20.2 e/s/krad obtained for wafer lot P20291.1 at 25°C).

A few additional hot pixels appear in the dark current histograms during irradiation. The density generated by electron irradiation is negligible compared to the initial one. Displacement damage contribution of the electron irradiation has a negligible effect on spike density.

Concerning annealing results, no significant effect has been observed except on the mean dark current and full frame DR dark current images. A reverse annealing is observed when parts are biased OFF. Mean dark current continues to increase slightly. Reduction is observed when parts are biased ON. In addition, as annealing is performed in NDR mode with a partial addressing of the FPA, addressed lines exhibit a quicker annealing compared to unaddressed lines. After one month at 50°C, enhanced annealing is observed on parts biased ON (likely due shorter time constant), while reverse annealing is observed on part biased OFF. Reverse annealing effect remains negligible on DSNU.

Odd/even offset in DR mode is sensitive to irradiation. Drift is not negligible and depends on the part considered. A variation of 150 electrons is to be considered for EOL mission performances. This drift has an impact on acquisition mode, not in tracking mode (DR mode not used in tracking). The variability between parts is difficult to explain. Detector D3 exhibits a positive drift while all the other parts have a negative drift. The reason of this behaviour remains obscure. The only specificity found on D3 is that this part needs a register value (to match odd even column offset) which is the lowest compared to the other parts.

Mean offsets drift observed in DR and NDR mode are without impact on STR application.

6.9.Detailed test results

6.9.1.NDR reference level

NDR reference level (electrons) – Parts irradiated and annealed biased ON (except D3 biased OFF after 62 hours anneal)

Mean_black	D1	D2	D3
0 krad	20048	20358	19522
4.0 krad	20100	20388	19542
10 krad	20085	20402	19559
20 krad	20154	20424	19603
34 krad	20206	20472	19637
stop+anneal 20h	20246	20414	19658
+ anneal 42h	20246	20427	19670
+ anneal 62h	20245	20424	19674
+ anneal 1 week	20210	20420	19611
+ anneal 2 weeks	20208	20446	19633
+ anneal 3 weeks	20203	20417	19602
+ anneal 4 weeks	20198	20431	19631
stop+ anneal 6 weeks	20200	20471	19605
stop+ anneal 8 weeks	20233	20477	19647

Table 6-2: NDR reference level measurements

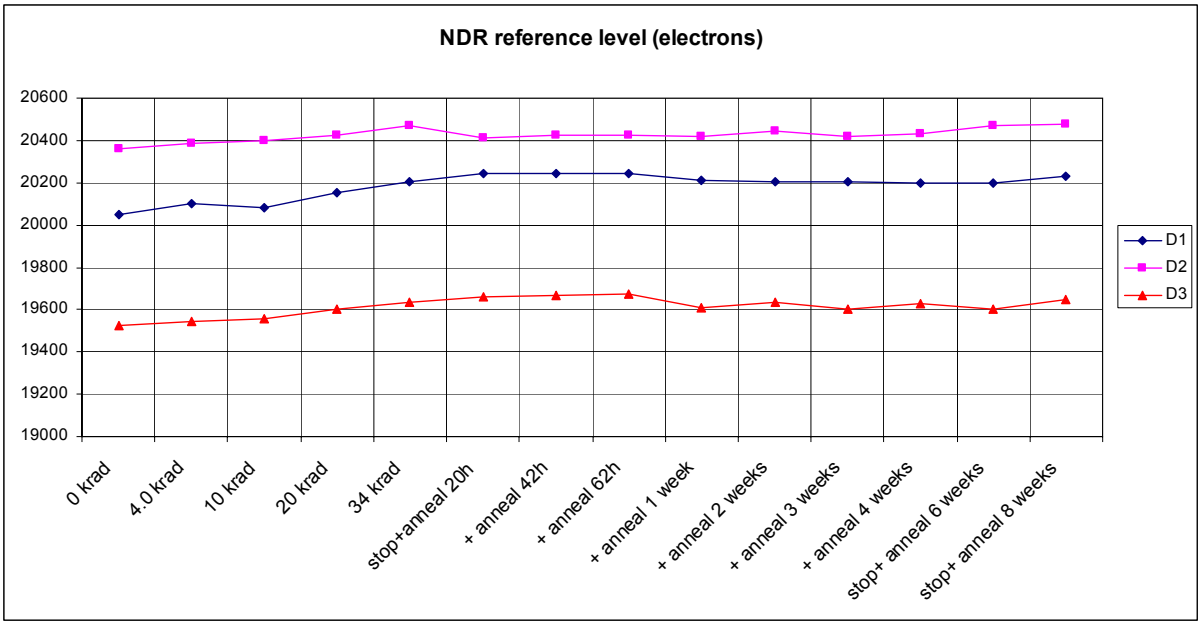

Figure 6-2 : NDR reference level evolution with irradiation

6.9.2.Temporal noise NDR

Temporal noise NDR (electrons) – Parts irradiated and annealed biased ON (except D3 biased OFF after 62 hours anneal)

	D1	D2	D3
0 krad	80	79	97
4.0 krad	80	77	96
10 krad	80	77	96
20 krad	79	78	95
34 krad	80	79	95
stop+anneal 20h	82	84	108
+ anneal 42h	83	85	109
+ anneal 62h	82	85	109
+ anneal 1 week	82	85	105
+ anneal 2 weeks	83	84	104
+ anneal 3 weeks	83	86	108
+ anneal 4 weeks	82	83	105
stop+ anneal 6 weeks	88	79	115
stop+ anneal 8 weeks	76	85	118

Table 6-3: Temporal noise NDR measurements

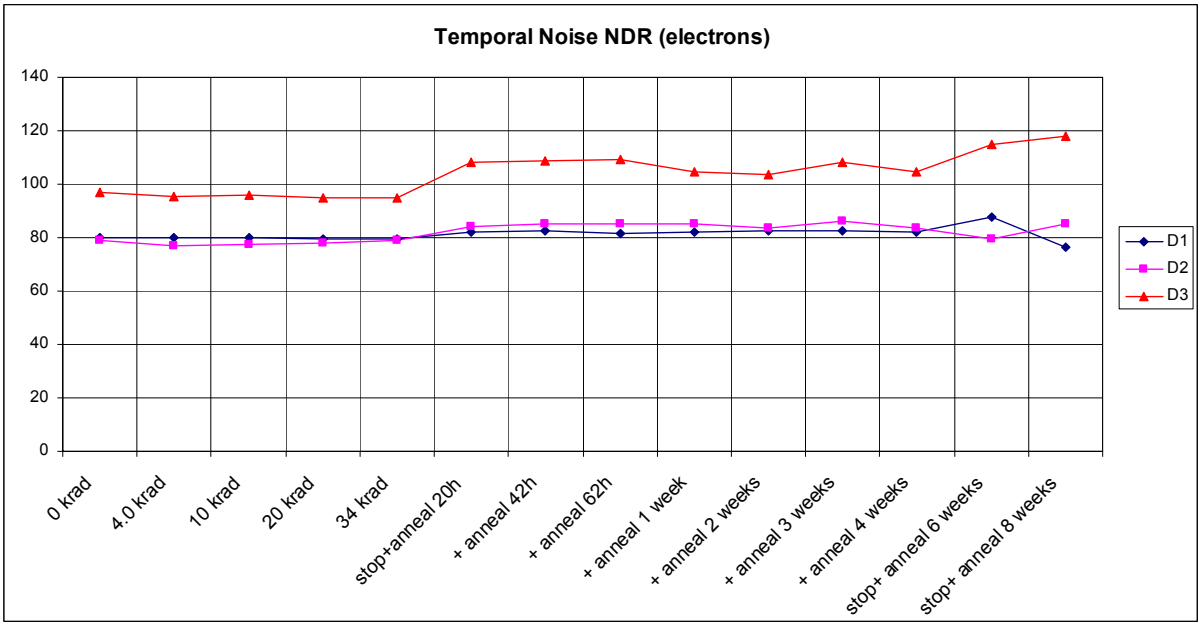

Figure 6-3 : Temporal noise NDR evolution with irradiation

6.9.3.FPN NDR

FPN NDR (electrons) – Parts irradiated and annealed biased ON (except D3 biased OFF after 62 hours anneal)

FPN NDR	D1	D2	D3
0 krad	21	19	23
4.0 krad	20	19	23
10 krad	20	19	23
20 krad	20	20	23
34 krad	22	21	24
stop+anneal 20h	22	23	27
+ anneal 42h	21	23	27
+ anneal 62h	21	22	27
+ anneal 1 week	21	22	26
+ anneal 2 weeks	21	21	26
+ anneal 3 weeks	21	22	27
+ anneal 4 weeks	20	21	27
stop+ anneal 6 weeks	22	21	27
stop+ anneal 8 weeks	19	22	30

Table 6-4: FPN NDR measurements

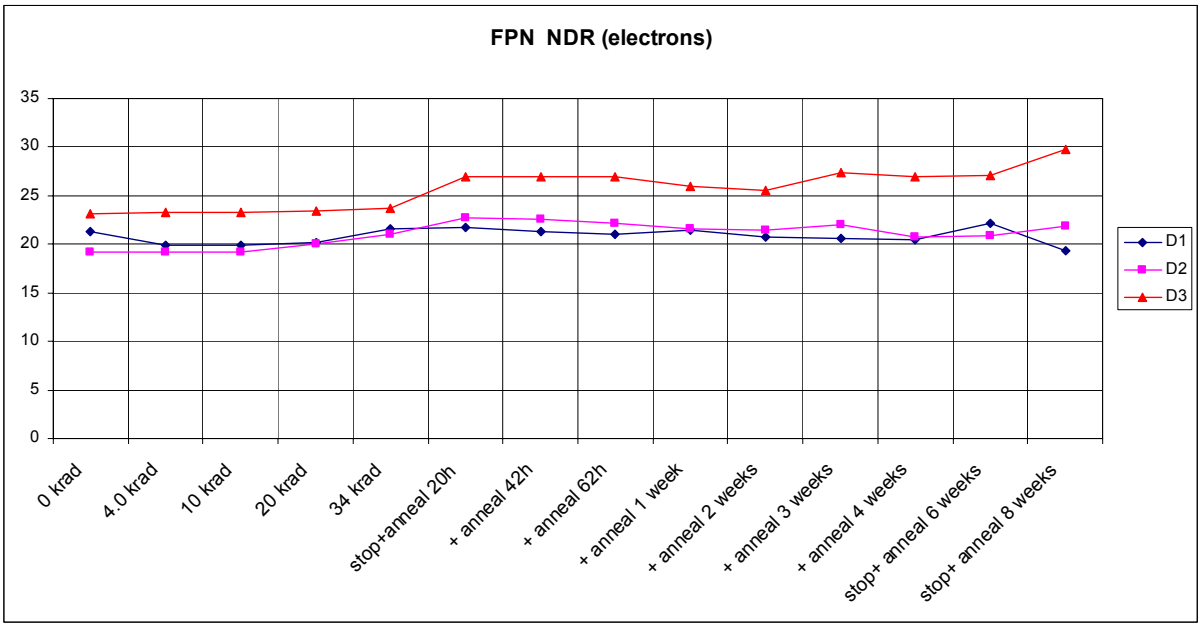

Figure 6-4 : FPN NDR evolution with irradiation

6.9.4.Column FPN NDR

Column FPN NDR (electrons– Parts irradiated and annealed biased ON (except D3 biased OFF after 62 hours anneal)

	D1	D2	D3
0 krad	3.5	3.7	4.2
4.0 krad	3.5	3.7	4.1
10 krad	3.6	3.6	4.4
20 krad	3.8	3.6	4.3
34 krad	3.7	4.0	4.6
stop+anneal 20h	3.7	4.2	4.9
+ anneal 42h	3.8	4.5	4.8
+ anneal 62h	3.8	4.2	4.9
+ anneal 1 week	3.7	4.3	4.8
+ anneal 2 weeks	3.6	4.4	4.8
+ anneal 3 weeks	3.4	4.3	5.1
+ anneal 4 weeks	3.7	3.7	4.9
stop+ anneal 6 weeks	3.8	3.8	5.2
stop+ anneal 8 weeks	3.6	4.2	5.3

Table 6-5: Column FPN NDR measurements

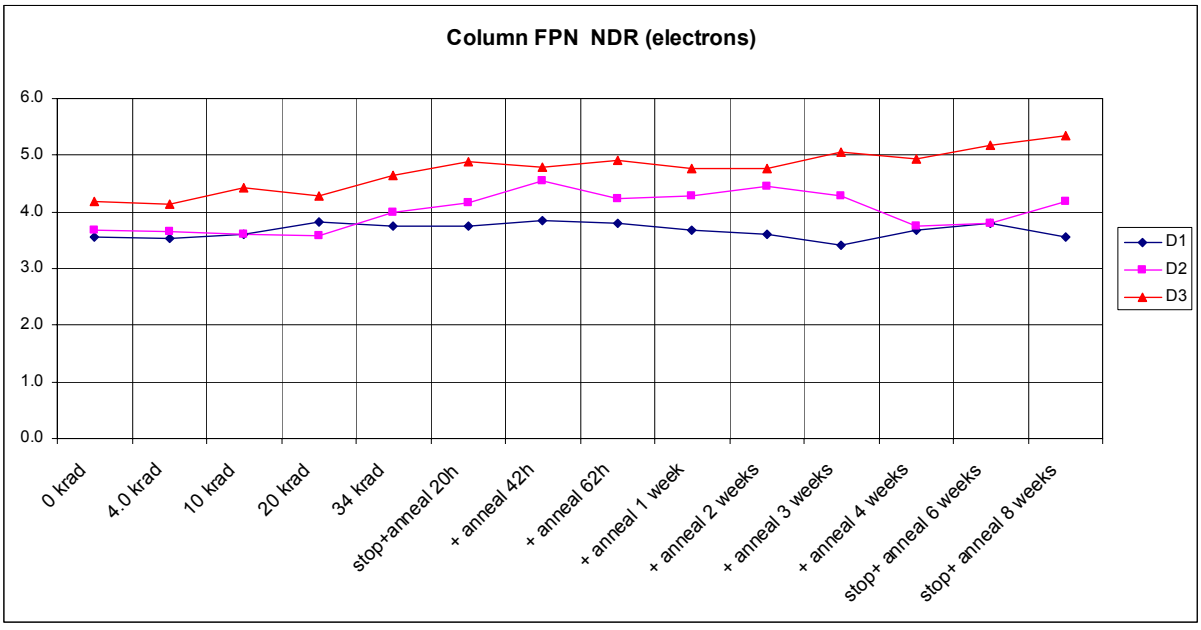

Figure 6-5 : Column FPN NDR evolution with irradiation

6.9.5.Pixel FPN NDR

Pixel FPN NDR (electrons) – Parts irradiated and annealed biased ON (except D3 biased OFF after 62 hours anneal)

	D1	D2	D3
0 krad	21	19	23
4.0 krad	19	19	23
10 krad	19	19	23
20 krad	20	19	23
34 krad	21	20	23
stop+anneal 20h	21	22	26
+ anneal 42h	21	22	26
+ anneal 62h	20	21	26
+ anneal 1 week	21	21	25
+ anneal 2 weeks	20	21	25
+ anneal 3 weeks	20	21	27
+ anneal 4 weeks	20	20	26
stop+ anneal 6 weeks	22	20	26
stop+ anneal 8 weeks	19	21	29

Table 6-6: Pixel FPN NDR measurements

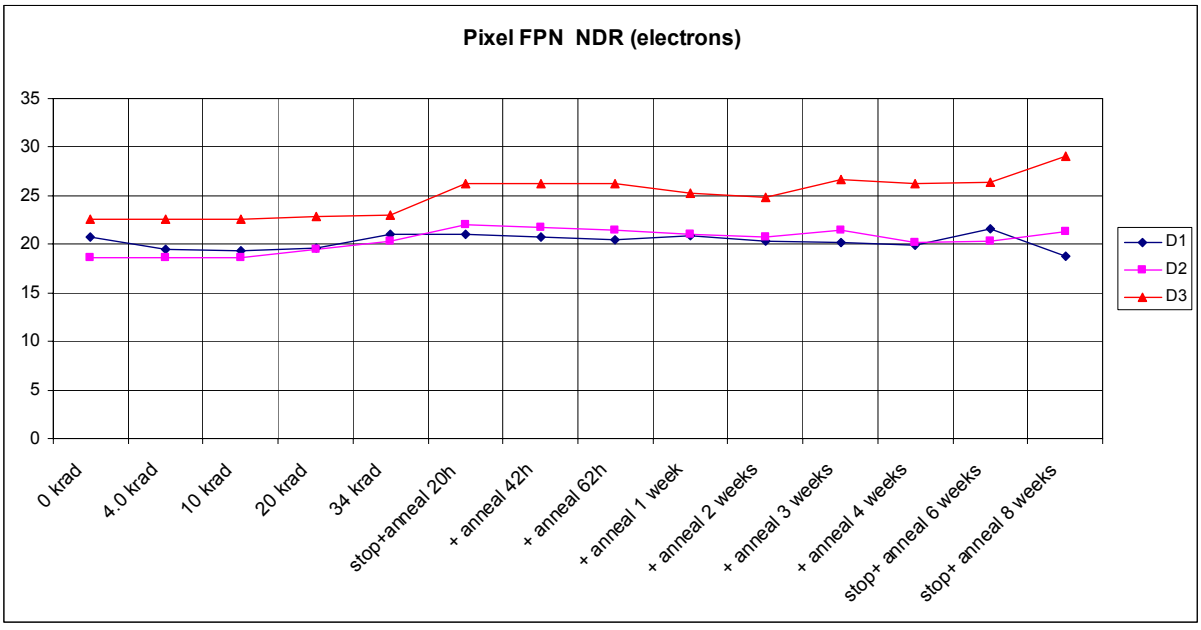

Figure 6-6 : Pixel FPN NDR evolution with irradiation

6.9.6.Mean offset DR

Mean offset DR (electrons– Parts irradiated and annealed biased ON (except D3 biased OFF after 62 hours anneal)

	D1	D2	D3
0 krad	4940	5139	5033
4.0 krad	4997	5191	5063
10 krad	5015	5243	5101
20 krad	5122	5310	5187
34 krad	5220	5406	5251
stop+anneal 20h	5295	5423	5275
+ anneal 42h	5289	5426	5279
+ anneal 62h	5284	5414	5280
+ anneal 1 week	5257	5391	5240
+ anneal 2 weeks	5225	5375	5236
+ anneal 3 weeks	5239	5380	5230
+ anneal 4 weeks	5230	5369	5236
stop+ anneal 6 weeks	5240	5322	5227
stop+ anneal 8 weeks	5241	5382	5248

Table 6-7: Mean offset DR measurements

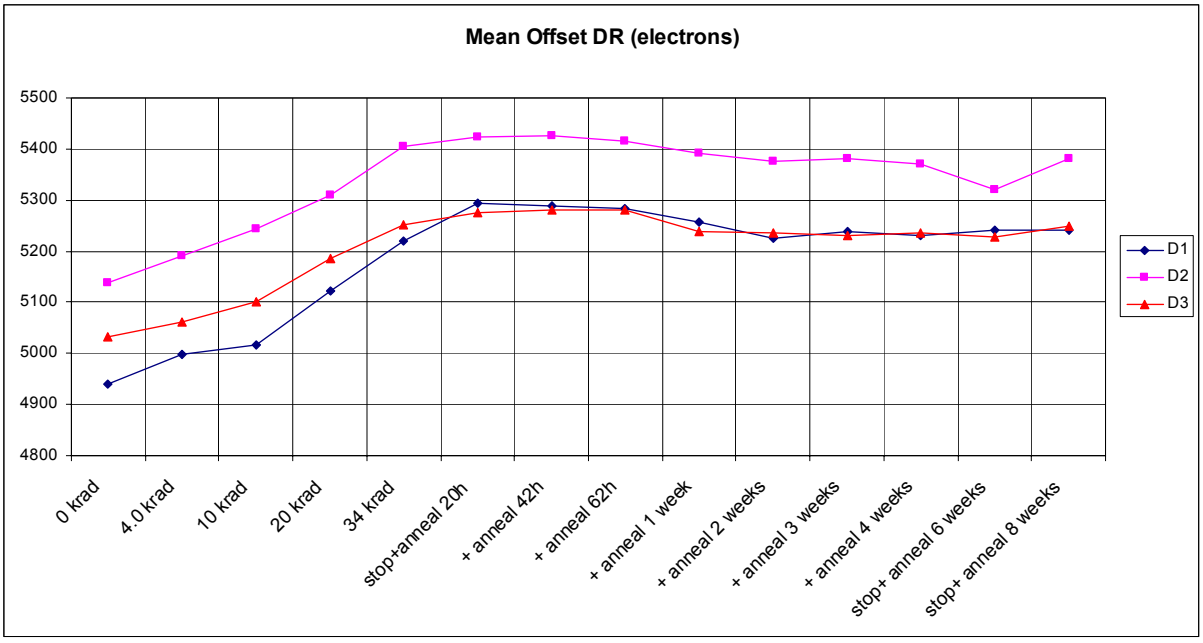

Figure 6-7 : Mean offset DR evolution with irradiation

6.9.7.Temporal noise DR

Temporal noise DR (electrons) – Parts irradiated and annealed biased ON (except D3 biased OFF after 62 hours anneal)

	D1	D2	D3
0 krad	74	75	84
4.0 krad	73	74	84
10 krad	73	74	84
20 krad	73	74	85
34 krad	73	74	84
stop+anneal 20h	74	77	92
+ anneal 42h	75	78	92
+ anneal 62h	74	78	92
+ anneal 1 week	73	77	90
+ anneal 2 weeks	74	76	89
+ anneal 3 weeks	74	77	92
+ anneal 4 weeks	74	76	90
stop+ anneal 6 weeks	75	73	93
stop+ anneal 8 weeks	73	78	90

Table 6-8: Temporal noise DR measurements

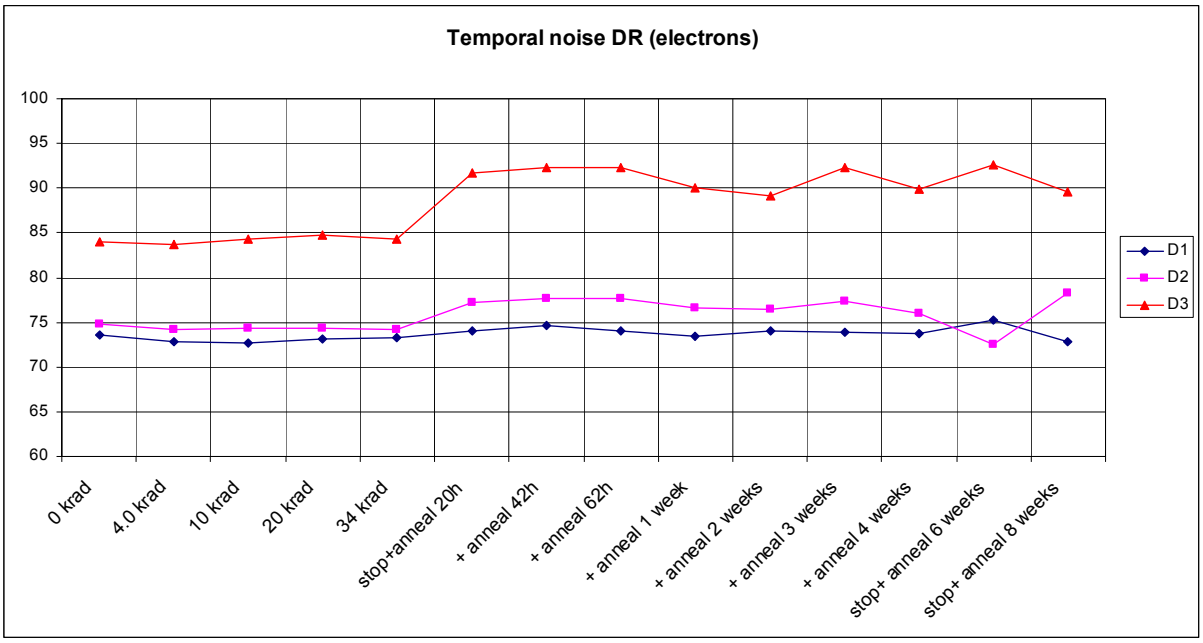

Figure 6-8 : Temporal noise DR evolution with irradiation

6.9.8.Global FPN DR

Global FPN DR (electrons) – Parts irradiated and annealed biased ON (except D3 biased OFF after 62 hours anneal)

	D1	D2	D3
0 krad	206	178	124
4.0 krad	215	185	130
10 krad	221	190	140
20 krad	227	197	152
34 krad	227	203	170
stop+anneal 20h	227	204	172
+ anneal 42h	229	203	172
+ anneal 62h	228	203	173
+ anneal 1 week	226	202	169
+ anneal 2 weeks	225	200	167
+ anneal 3 weeks	226	201	170
+ anneal 4 weeks	225	200	167
stop+ anneal 6 weeks	226	201	167
stop+ anneal 8 weeks	225	201	168

Table 6-9: Global FPN DR measurements

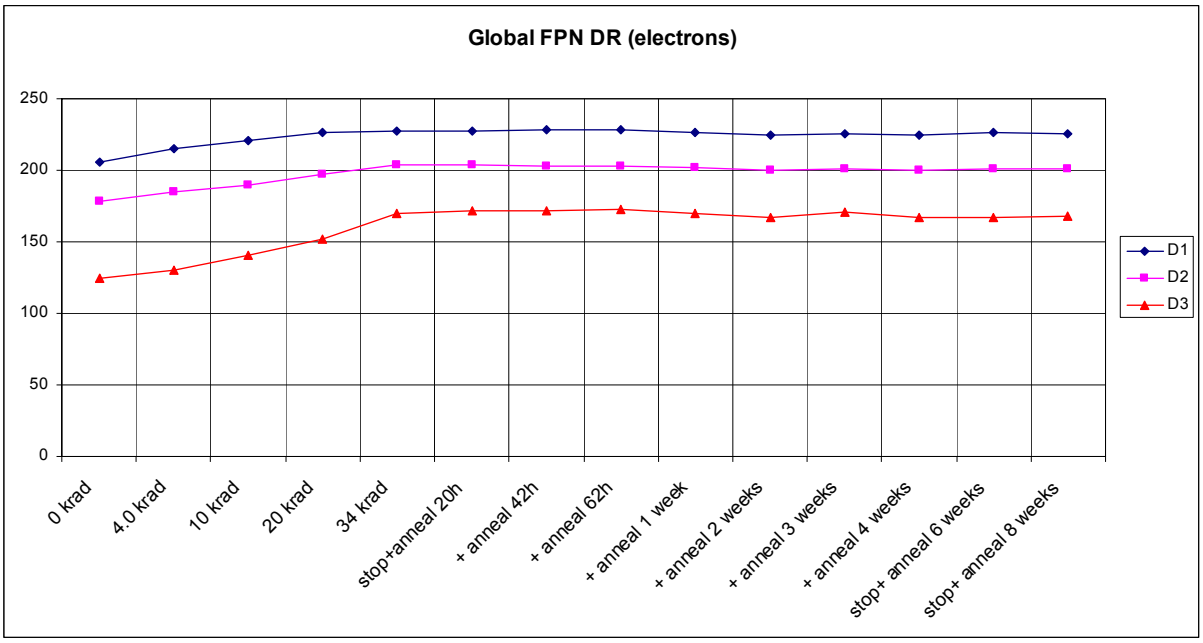

Figure 6-9 : Global FPN DR evolution with irradiation

6.9.9.Local FPN DR

Local FPN DR (electrons) – Parts irradiated and annealed biased ON (except D3 biased OFF after 62 hours anneal)

	D1	D2	D3
0 krad	189	166	109
4.0 krad	198	172	115
10 krad	203	177	123
20 krad	209	184	133
34 krad	210	190	151
stop+anneal 20h	210	190	151
+ anneal 42h	211	189	151
+ anneal 62h	210	189	152
+ anneal 1 week	209	188	150
+ anneal 2 weeks	207	186	148
+ anneal 3 weeks	208	187	152
+ anneal 4 weeks	207	186	148
stop+ anneal 6 weeks	208	187	146
stop+ anneal 8 weeks	208	188	149

Table 6-10: Local FPN DR measurements

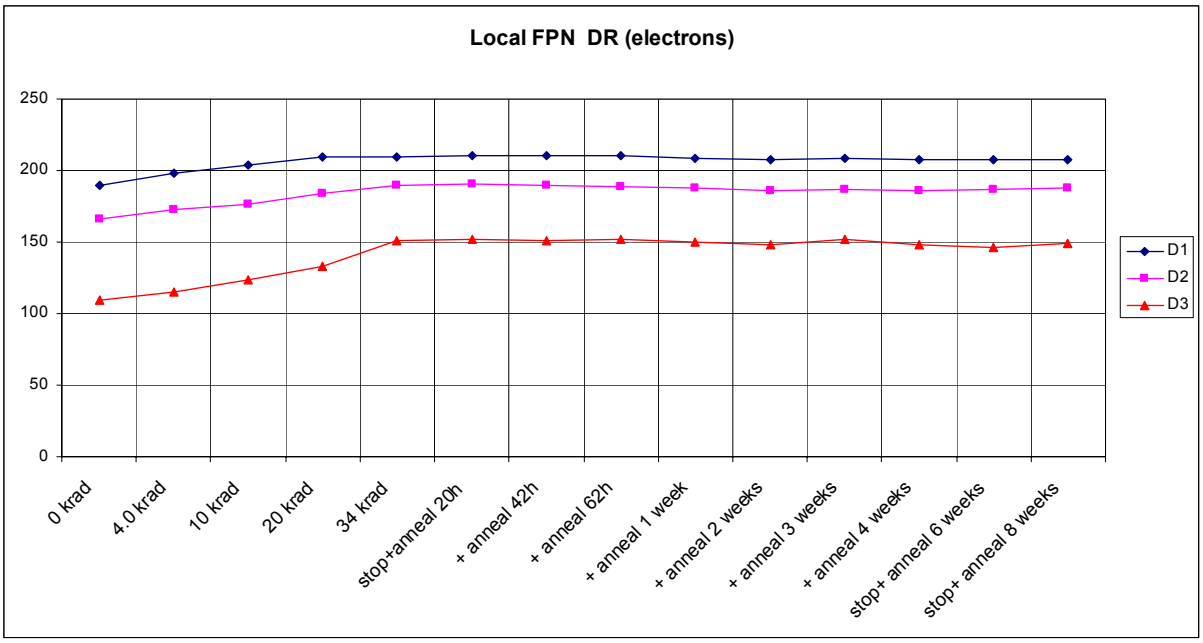

Figure 6-10 : Local FPN DR evolution with irradiation

6.9.10.Local column FPN DR

Local column FPN DR (electrons) – Parts irradiated and annealed biased ON (except D3 biased OFF after 62 hours anneal)

	D1	D2	D3
0 krad	54	50	39
4.0 krad	57	51	40
10 krad	58	52	47
20 krad	62	58	54
34 krad	59	66	77
stop+anneal 20h	60	64	71
+ anneal 42h	60	60	71
+ anneal 62h	59	59	74
+ anneal 1 week	59	62	74
+ anneal 2 weeks	60	62	74
+ anneal 3 weeks	59	62	78
+ anneal 4 weeks	58	63	74
stop+ anneal 6 weeks	59	63	70
stop+ anneal 8 weeks	59	65	72

Table 6-11: Local column FPN DR measurements

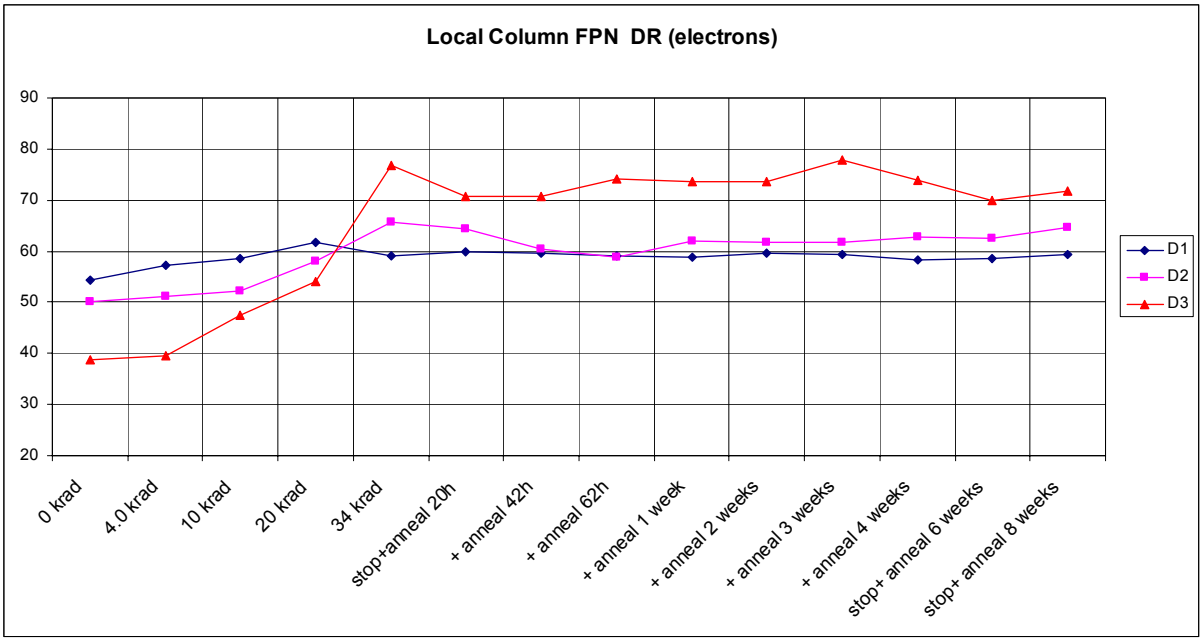

Figure 6-11 : Local column FPN DR evolution with irradiation

6.9.11.Mean even - Mean odd DR

Mean even - mean odd DR (electrons) – Parts irradiated and annealed biased ON (except D3 biased OFF after 62 hours anneal)

	D1	D2	D3
0 krad	1	-7	7
4.0 krad	22	-1	3
10 krad	-24	3	49
20 krad	-40	-46	68
34 krad	-13	-75	127
stop+anneal 20h	-23	-70	111
+ anneal 42h	-20	-53	110
+ anneal 62h	-13	-48	120
+ anneal 1 week	-17	-62	119
+ anneal 2 weeks	-27	-63	120
+ anneal 3 weeks	-22	-63	129
+ anneal 4 weeks	-9	-66	120
stop+ anneal 6 weeks	-12	-66	110
stop+ anneal 8 weeks	-24	-73	115

Table 6-12: Mean even – mean odd DR measurements

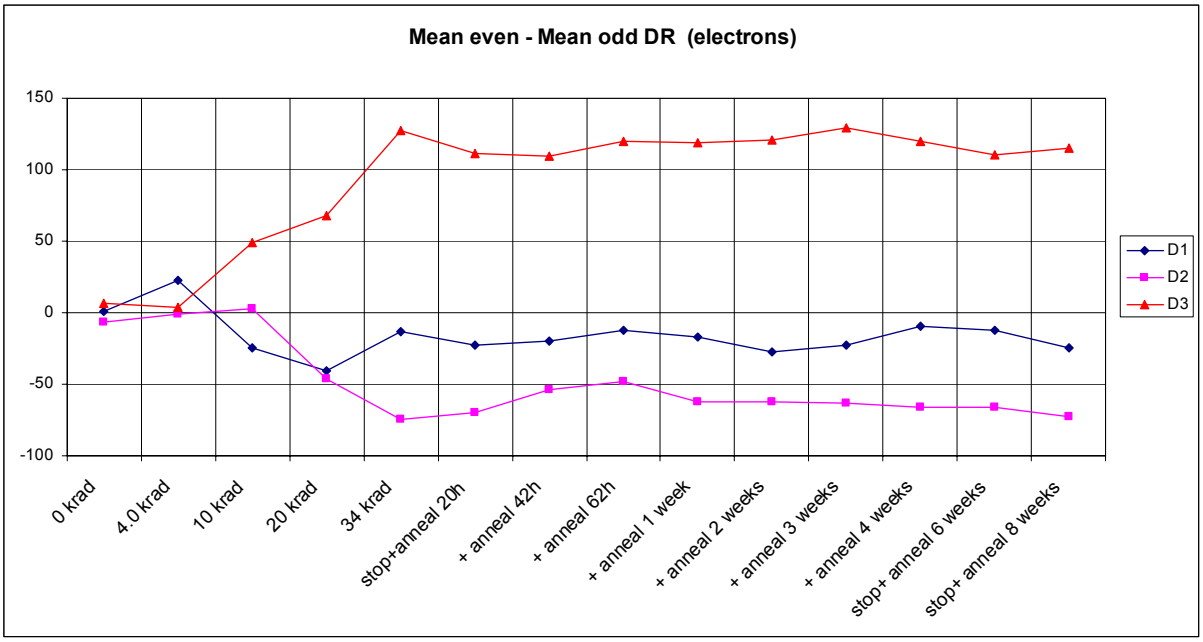

Figure 6-12 : Mean even – mean odd DR evolution with irradiation

6.9.12.Local pixel FPN DR

Local pixel FPN DR (electrons) – Parts irradiated and annealed biased ON (except D3 biased OFF after 62 hours anneal)

	D1	D2	D3
0 krad	179	156	98
4.0 krad	187	162	104
10 krad	193	166	110
20 krad	198	172	118
34 krad	199	176	126
stop+anneal 20h	199	177	130
+ anneal 42h	200	177	130
+ anneal 62h	200	177	129
+ anneal 1 week	198	175	127
+ anneal 2 weeks	196	173	124
+ anneal 3 weeks	197	174	126
+ anneal 4 weeks	197	173	124
stop+ anneal 6 weeks	197	174	125
stop+ anneal 8 weeks	197	174	126

Table 6-13: Local pixel FPN DR measurements

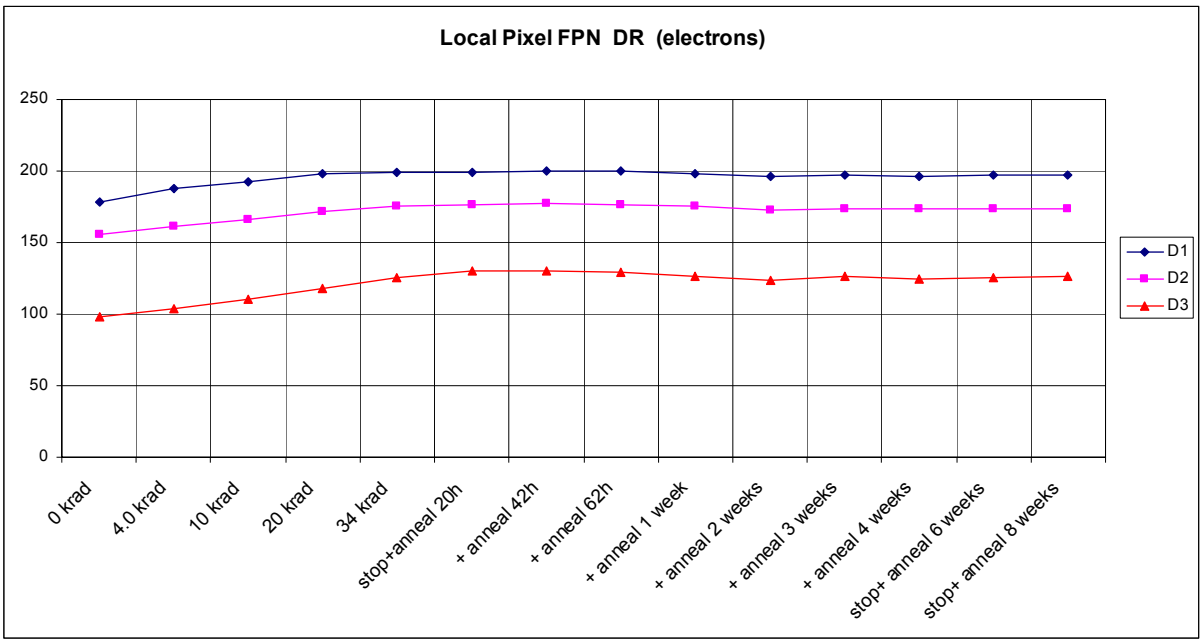

Figure 6-13 : Local pixel FPN DR evolution with irradiation

6.9.13.Column FPN corrected pre-rad

Even Column FPN corrected pre-rad (electrons) – Parts irradiated and annealed biased ON (except D3 biased OFF after 62 hours anneal)

Odd and even column FPN is calculated after correction with the pre-rad column offset (image post processing)

	D1	D2	D3
0 krad	0.31	0.32	0.35
10 krad	2.74	2.49	4.85
34 krad	5.76	5.85	12.03
stop+anneal 20h	6.33	6.29	12.70
+ anneal 1 week	5.77	5.49	12.61
stop+ anneal 8 weeks	5.37	5.00	11.43

Table 6-14: Even column FPN corrected pre-rad measurements

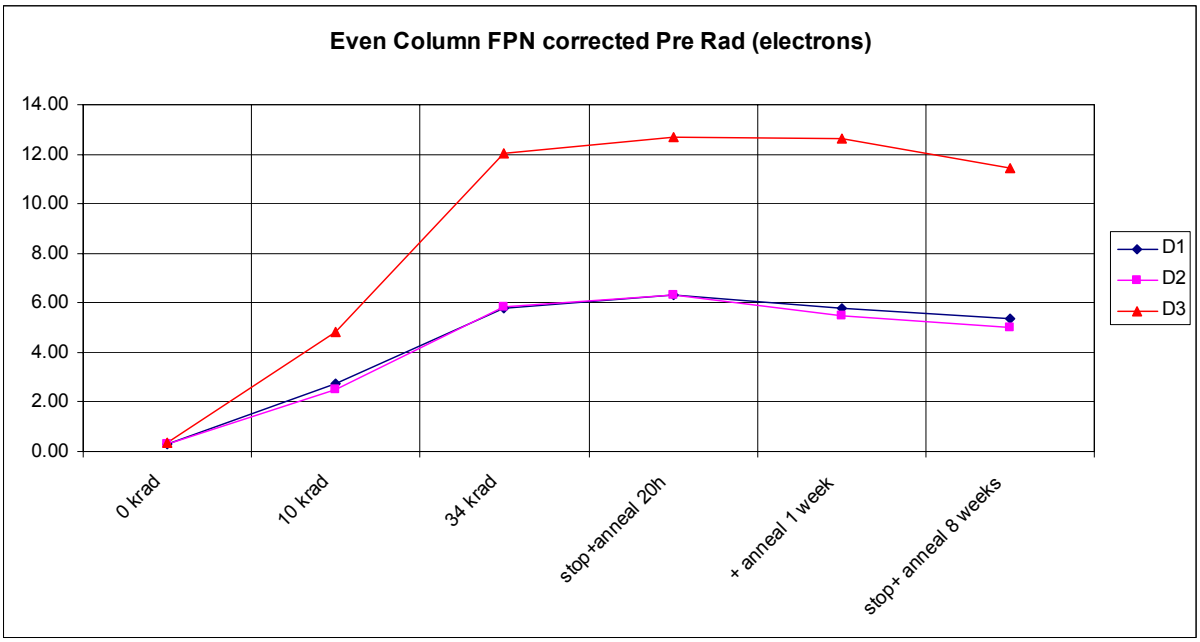

Figure 6-14 : Even column FPN corrected pre-rad evolution with irradiation

Odd Column FPN corrected Pre Rad (electrons) – Parts irradiated and annealed biased ON (except D3 biased OFF after 62 hours anneal)

	D1	D2	D3
0 krad	0.33	0.35	0.36
10 krad	2.64	2.53	4.56
34 krad	5.39	6.27	10.38
stop+anneal 20h	5.89	6.73	11.36
+ anneal 1 week	5.48	5.91	11.23
stop+ anneal 8 weeks	5.06	5.31	10.13

Table 6-15: Odd column FPN corrected pre-rad measurements

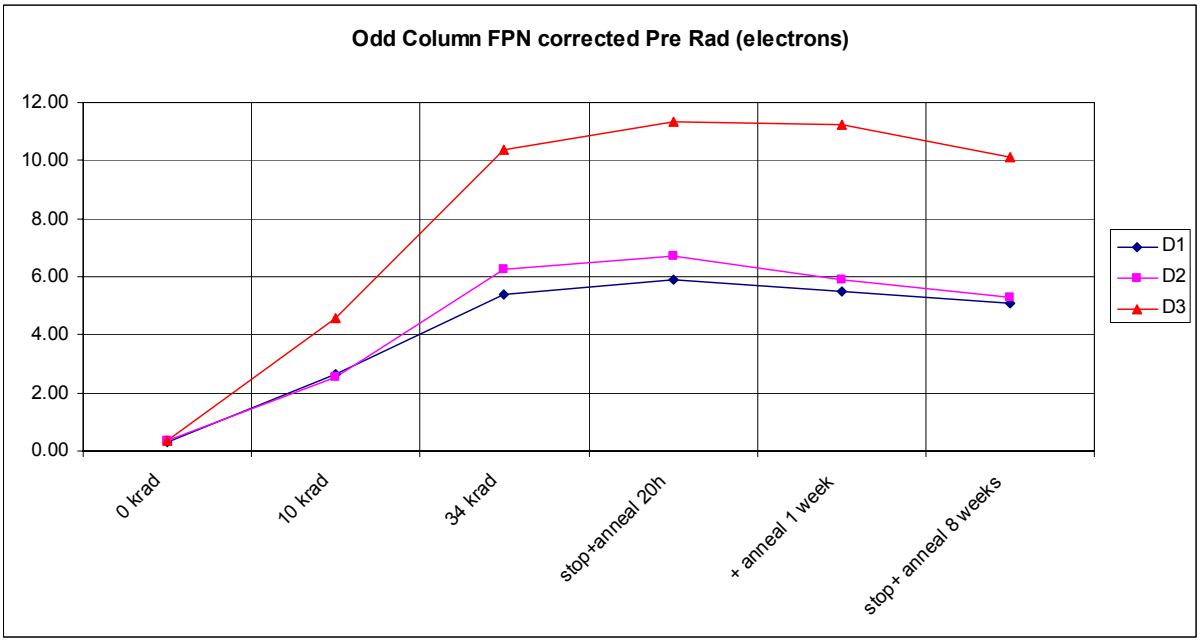

Figure 6-15 : Odd column FPN DR evolution with irradiation

6.9.14.Local DSNU

Local DSNU (electron) – Parts irradiated and annealed biased ON (except D3 biased OFF after 62 hours anneal)
Note: **integration time is 1.5 second** (all figures to be divided by 1.5 to obtain DSNU in electron/s)

	D1	D2	D3
0 krad	373	382	362
4.0 krad	608	627	600
10 krad	861	891	851
20 krad	1188	1242	1182
34 krad	1545	1637	1544
stop+anneal 20h	1655	1789	1633
+ anneal 42h	1618	1764	1600
+ anneal 62h	1607	1744	1592
+ anneal 1 week	1585	1704	1625
+ anneal 2 weeks	1547	1643	1613
+ anneal 3 weeks	1547	1661	1636
+ anneal 4 weeks	1534	1631	1622
stop+ anneal 6 weeks	1558	1666	1654
stop+ anneal 8 weeks	1516	1598	1625
+ anneal 12 weeks	1511	1573	1547
+ anneal 16 weeks (4 weeks @ 50°C)	972	1016	1624

Table 6-16: Local DSNU measurements

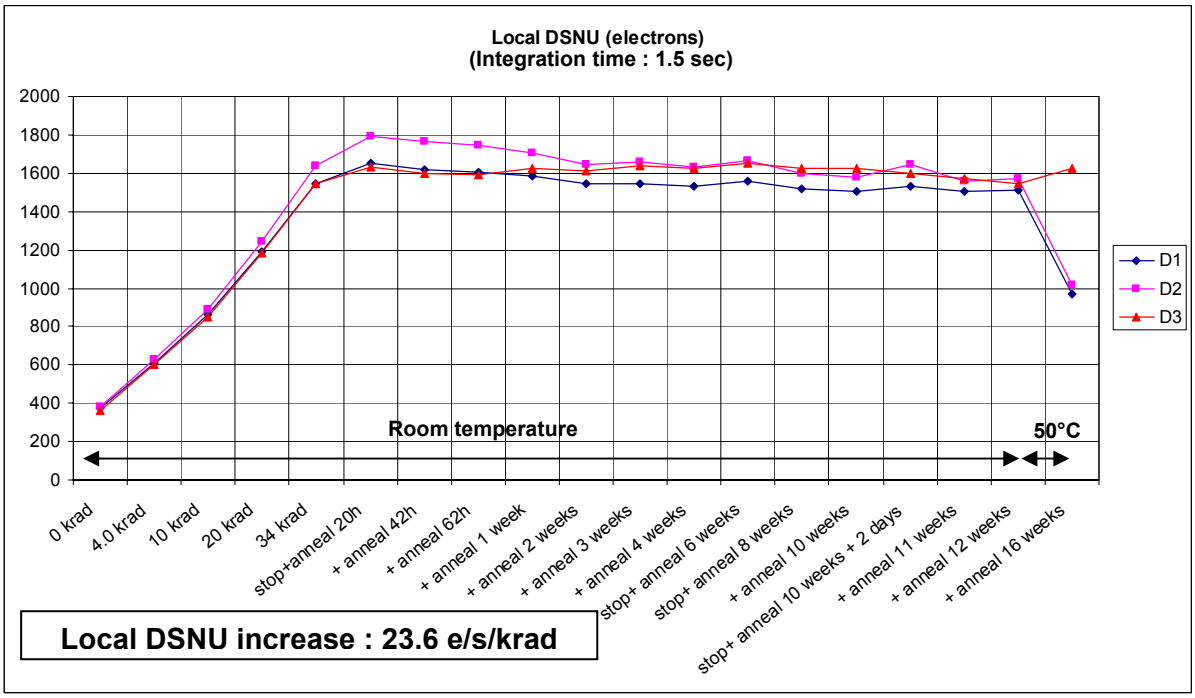

Figure 6-16 : Local DSNU evolution with irradiation

6.9.15.Global DSNU

Global DSNU (electron) – Parts irradiated and annealed biased ON (except D3 biased OFF after 62 hours anneal)
Note: **integration time is 1.5 second** (all figures to be divided by 1.5 to obtain DSNU in electron/s)

	D1	D2	D3
0 krad	635	593	606
4.0 krad	805	791	745
10 krad	1012	1021	966
20 krad	1315	1358	1282
34 krad	1678	1772	1644
stop+anneal 20h	1948	2107	1851
+ anneal 42h	2291	2491	2104
+ anneal 62h	2319	2519	2147
+ anneal 1 week	2240	2411	1899
+ anneal 2 weeks	2283	2426	1858
+ anneal 3 weeks	2268	2462	1868
+ anneal 4 weeks	2355	2525	1852
stop+ anneal 6 weeks	2287	2462	1879
stop+ anneal 8 weeks	2255	2366	1835
+ anneal 12 weeks	2181	2309	2146
+ anneal 16 weeks (4 weeks @ 50°C)	1130	1160	1989

Table 6-17: Global DSNU measurements

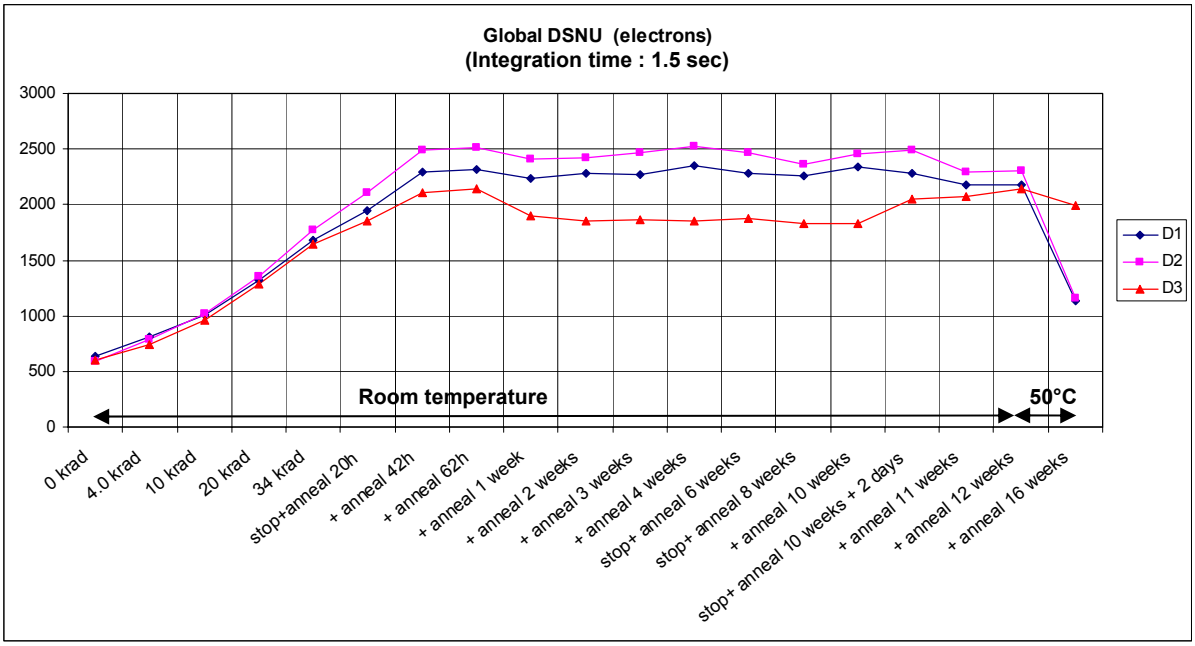

Figure 6-17 : Global DSNU evolution with irradiation

6.9.16.Mean dark current

Mean dark current (electron) – Parts irradiated and annealed biased ON (except D3 biased OFF after 62 hours anneal)
Note: **integration time is 200 milliseconds** (all figures to be multiplied by a factor 5 to obtain dark current in electron/s)

	D1	D2	D3
0 krad	13	14	30
4.0 krad	80	88	41
10 krad	216	238	171
20 krad	464	514	408
34 krad	837	932	763
stop+anneal 20h	931	1037	811
+ anneal 42h	664	769	606
+ anneal 62h	634	728	571
+ anneal 1 week	684	770	825
+ anneal 2 weeks	615	683	859
+ anneal 3 weeks	616	687	901
+ anneal 4 weeks	562	620	892
stop+ anneal 6 weeks	617	698	937
stop+ anneal 8 weeks	582	648	938
+ anneal 10 weeks	534	576	953
stop+ anneal 10 weeks + 2 days	595	659	732
+ anneal 11 weeks	623	653	620
+ anneal 12 weeks	624	661	606
+ anneal 16 weeks (4 weeks @ 50°C)	372	409	872

Table 6-18: Mean dark current measurements

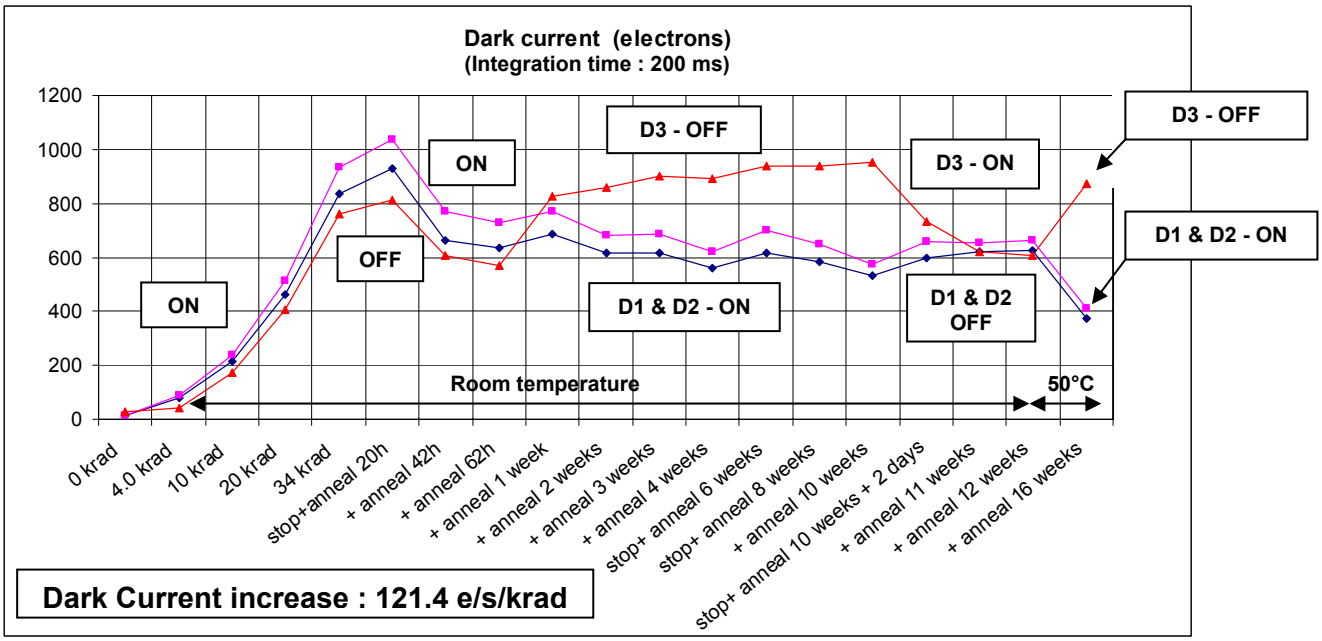

Figure 6-18 : Mean dark current evolution with irradiation

6.9.17.Dark current images and histograms in full frame DR mode

D1 - 0 krad – Irradiation ON

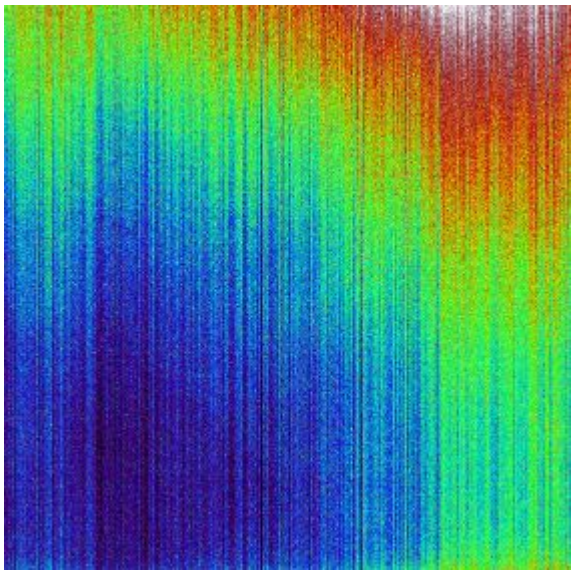

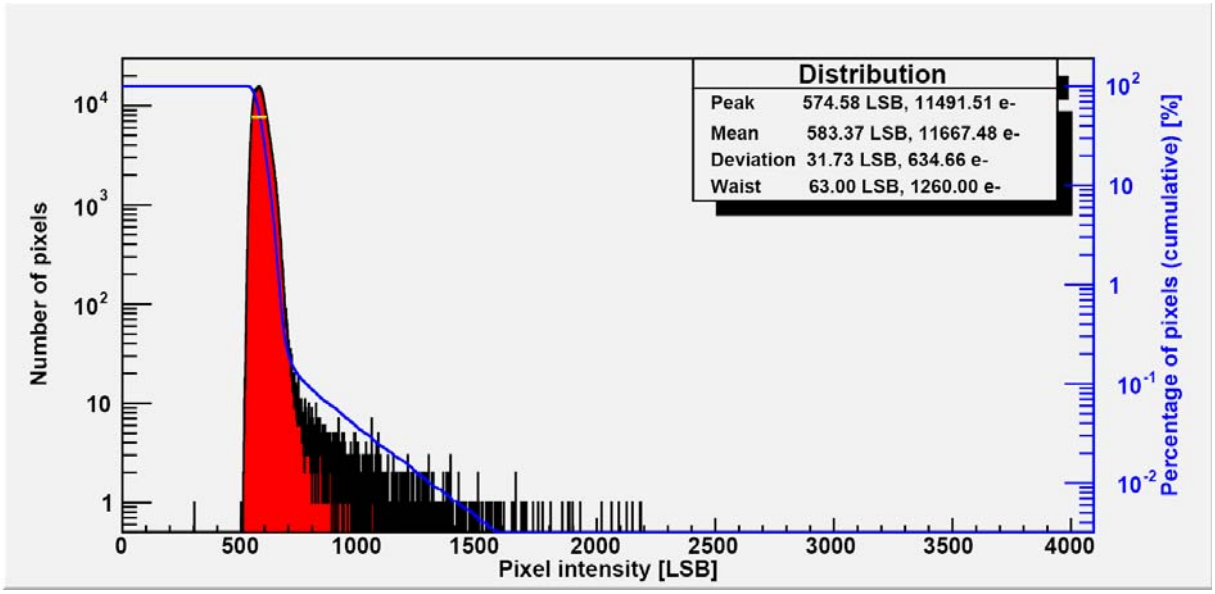

Figure 6-19 : D1 – 0 krad dark current map and histogram

D2 - 0 krad – Irradiation ON

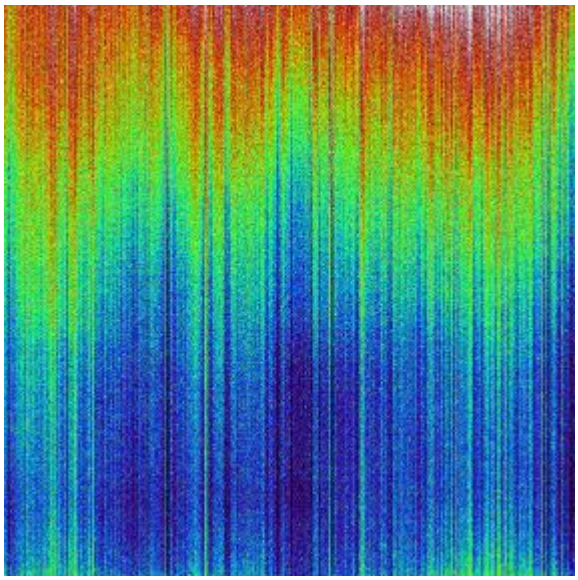

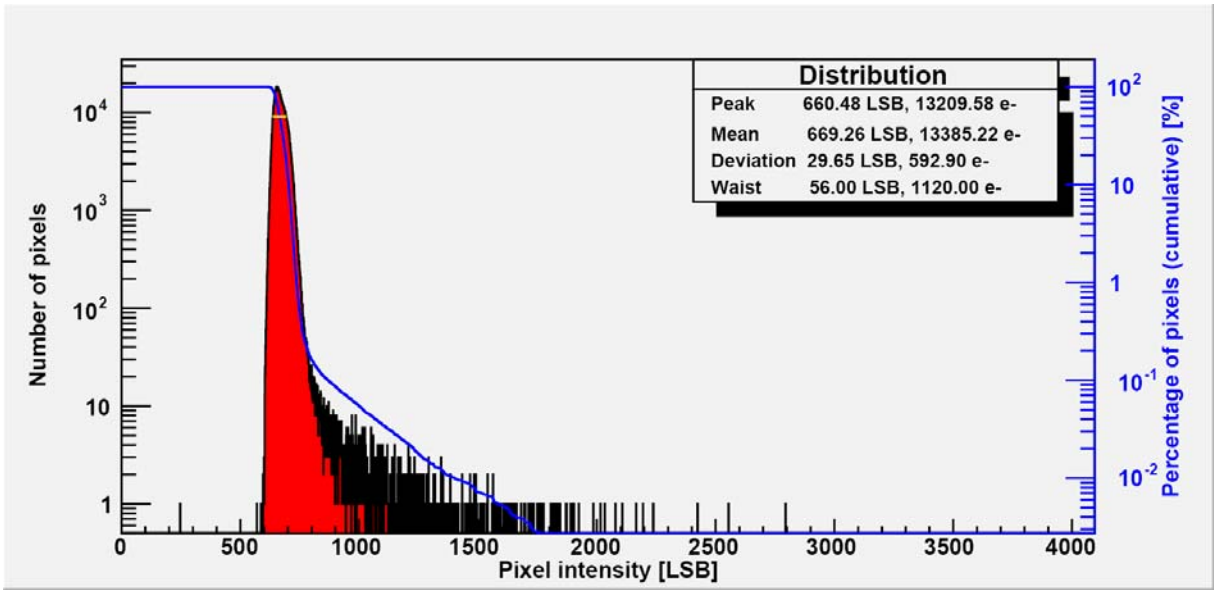

Figure 6-20 : D2 – 0 krad dark current map and histogram

D3 - 0 krad – Irradiation ON

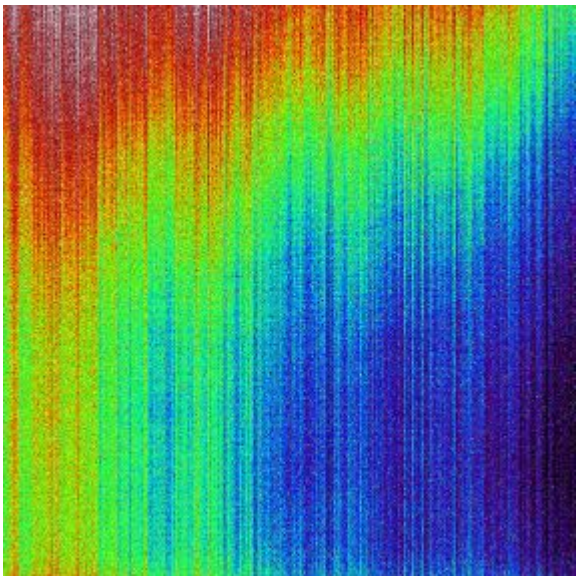

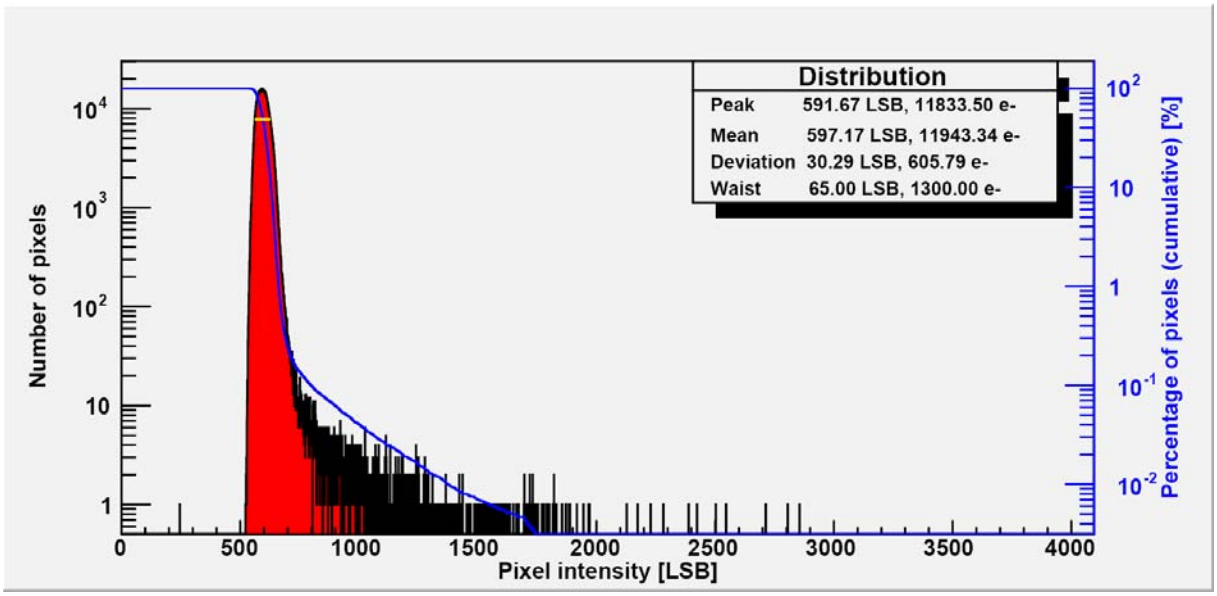

Figure 6-21 : D3 – 0 krad dark current map and histogram

D1 – 10 krad – Irradiation ON

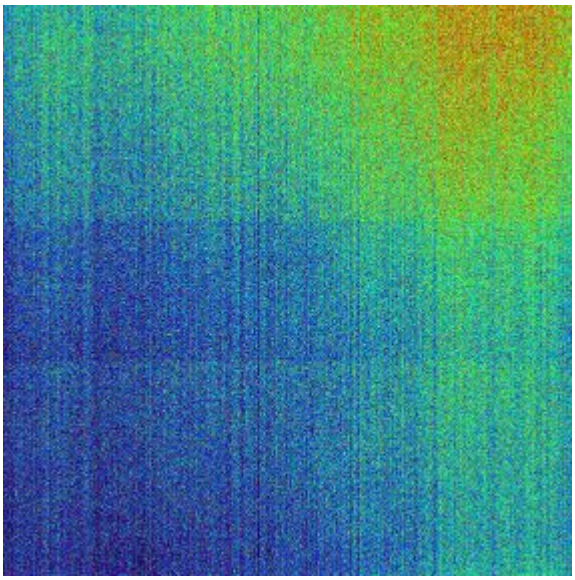

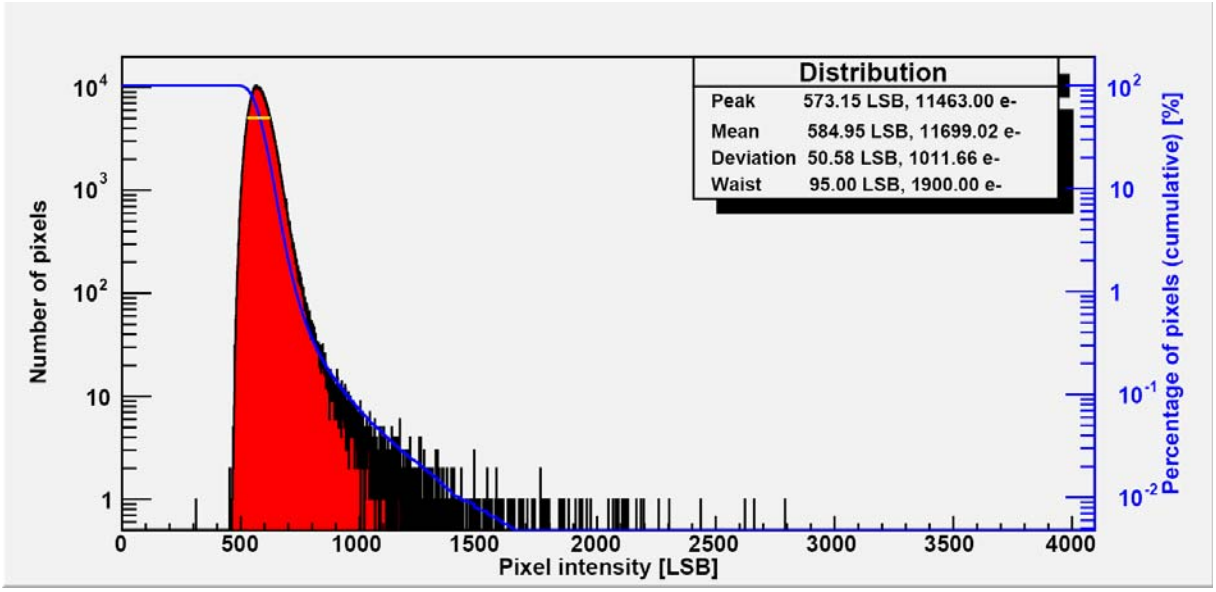

Figure 6-22 : D1 – 10 krad dark current map and histogram

D2 - 10 krad – Irradiation ON

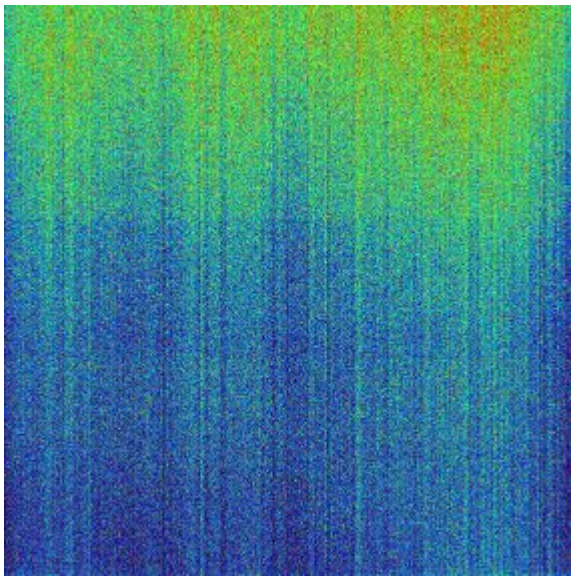

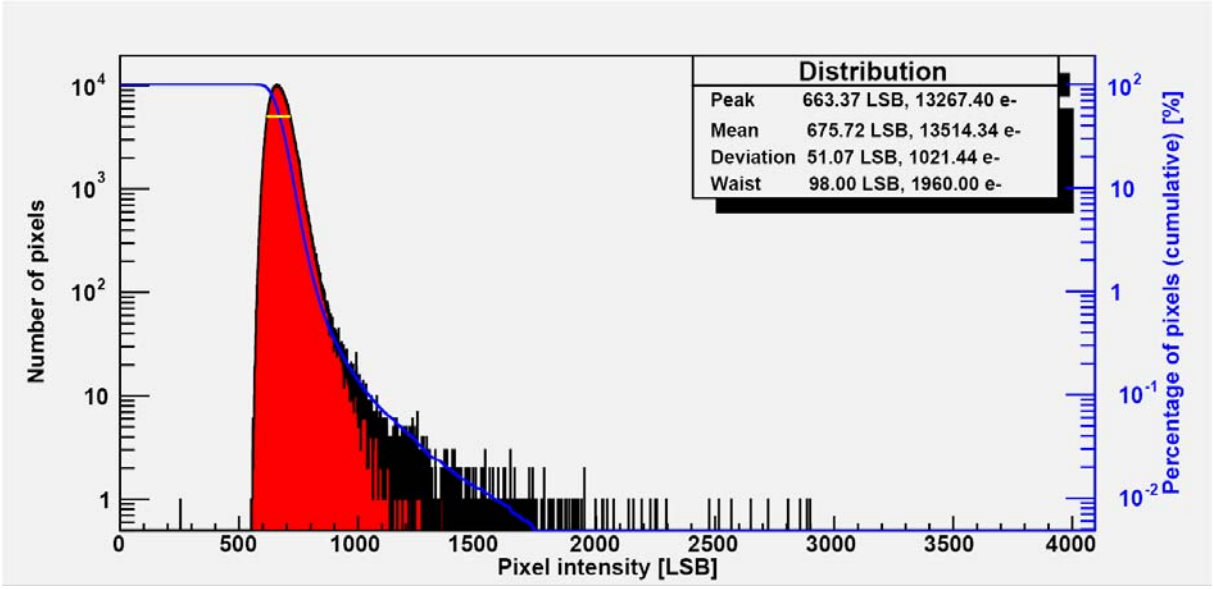

Figure 6-23 : D2 – 10 krad dark current map and histogram

D3 – 10 krad – Irradiation ON

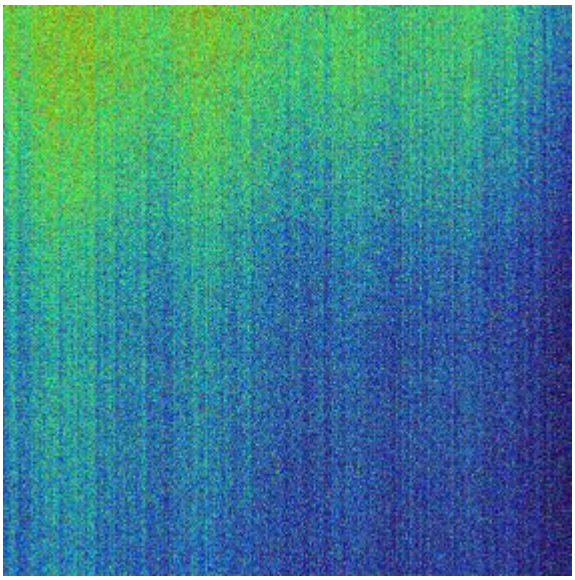

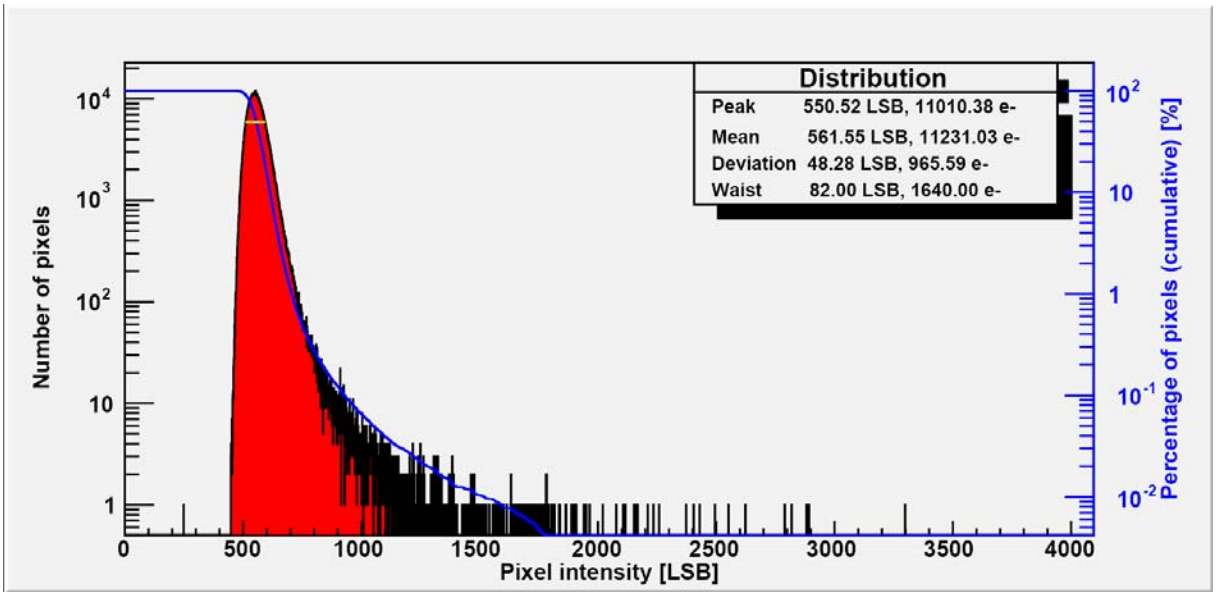

Figure 6-24 : D3 – 10 krad dark current map and histogram

D1 – 34 krad– Irradiation ON

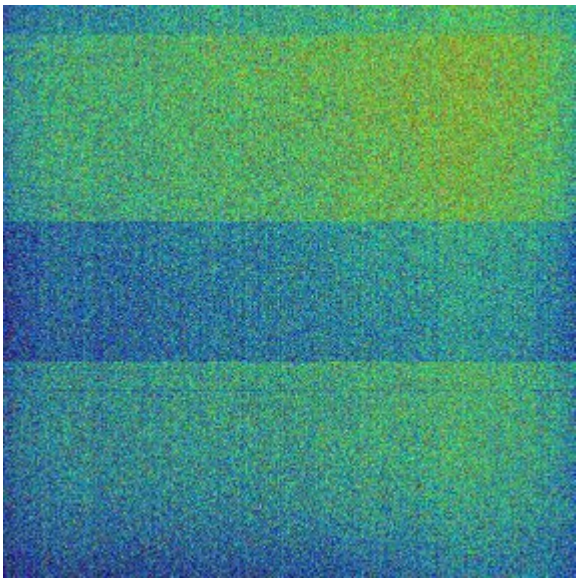

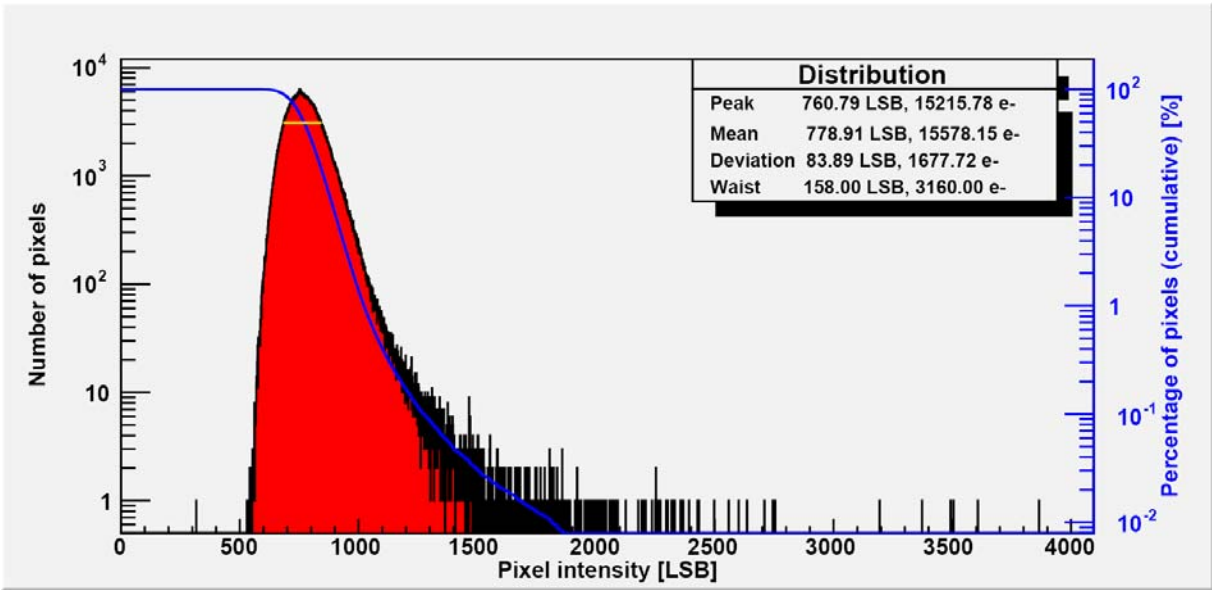

Figure 6-25 : D1 – 34 krad dark current map and histogram

D2 – 34 krad – Irradiation ON

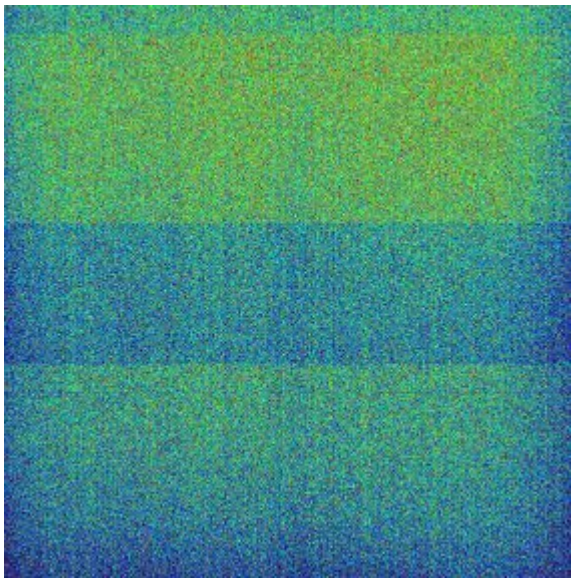

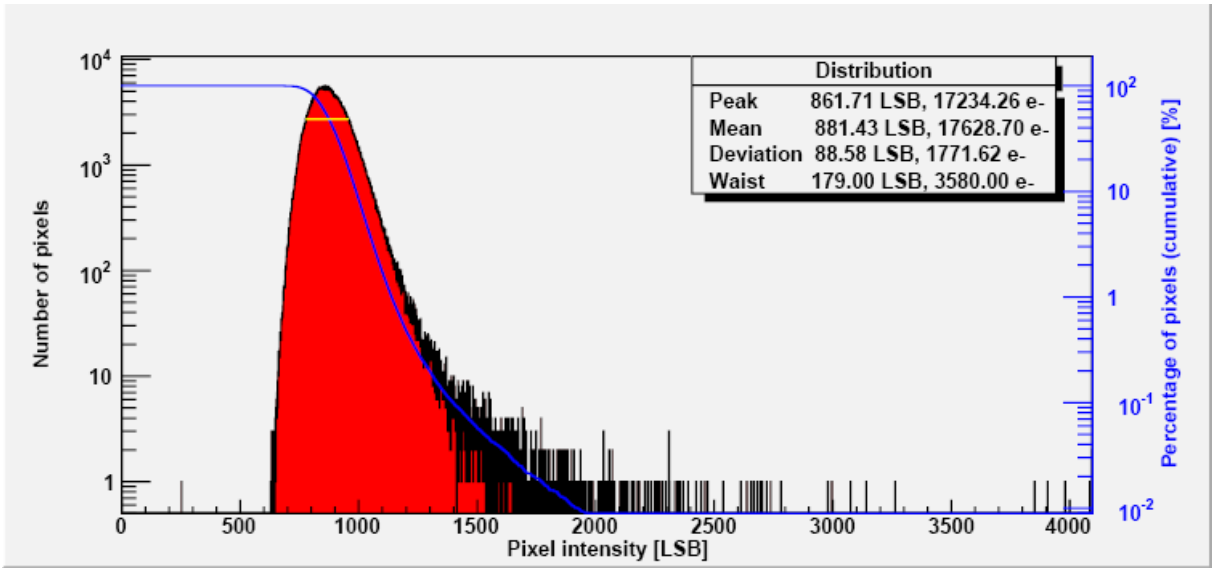

Figure 6-26 : D2 – 34 krad dark current map and histogram

D3 –34 krad – Irradiation ON

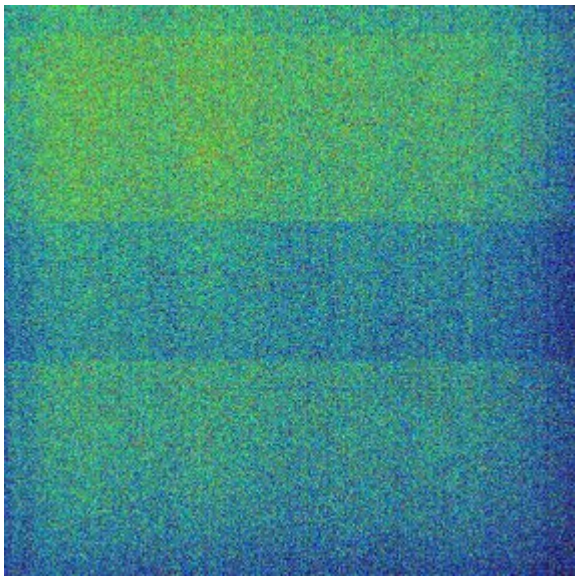

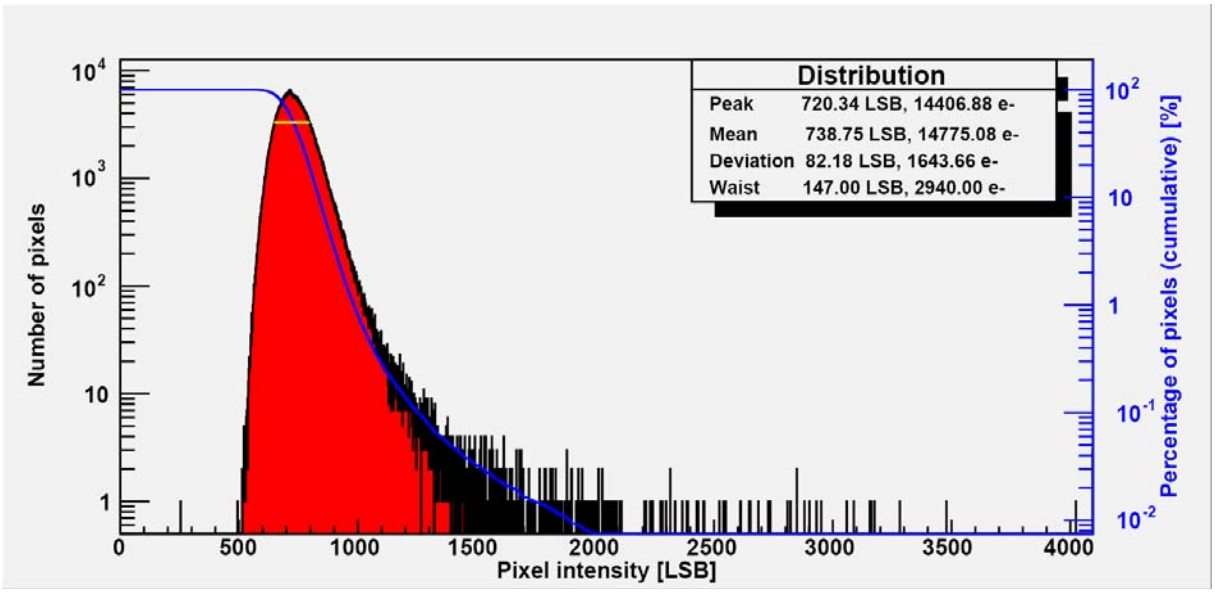

Figure 6-27 : D3 – 34 krad dark current map and histogram

D1 – 34 krad + 8 weeks – Annealing ON

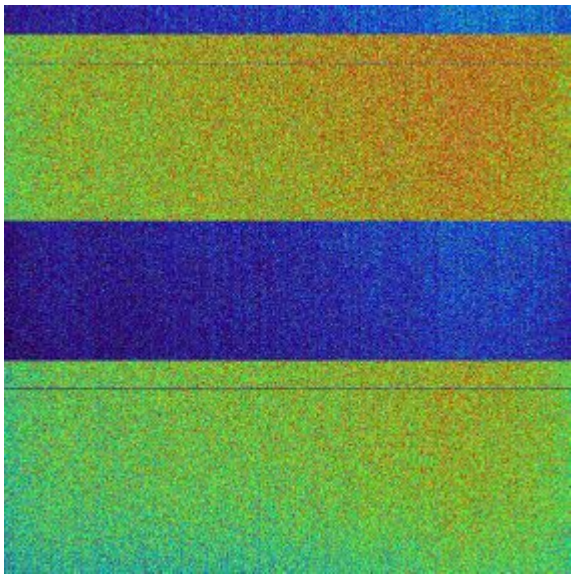

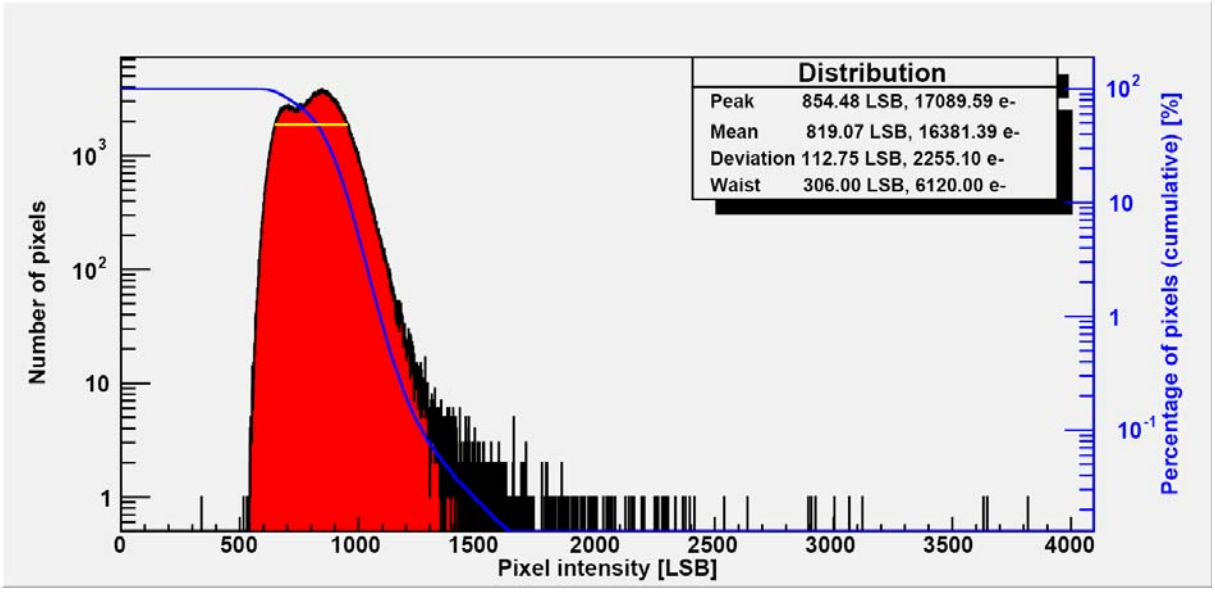

Figure 6-28 : D1 – 34 krad + 8 weeks annealing ON – dark current map and histogram

D2 – 34 krad + 8 weeks – Annealing ON

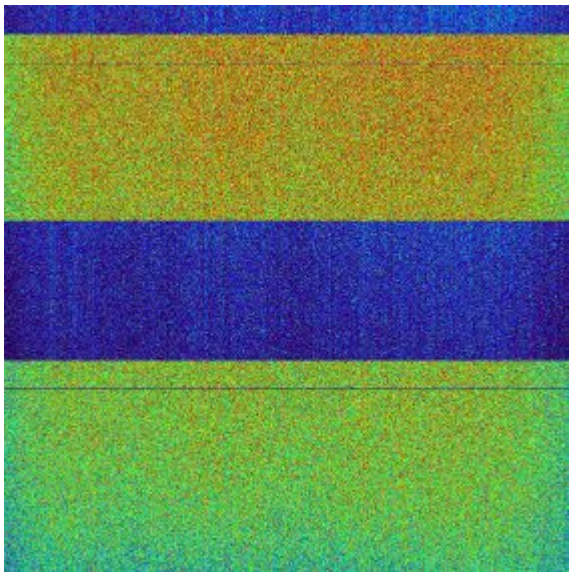

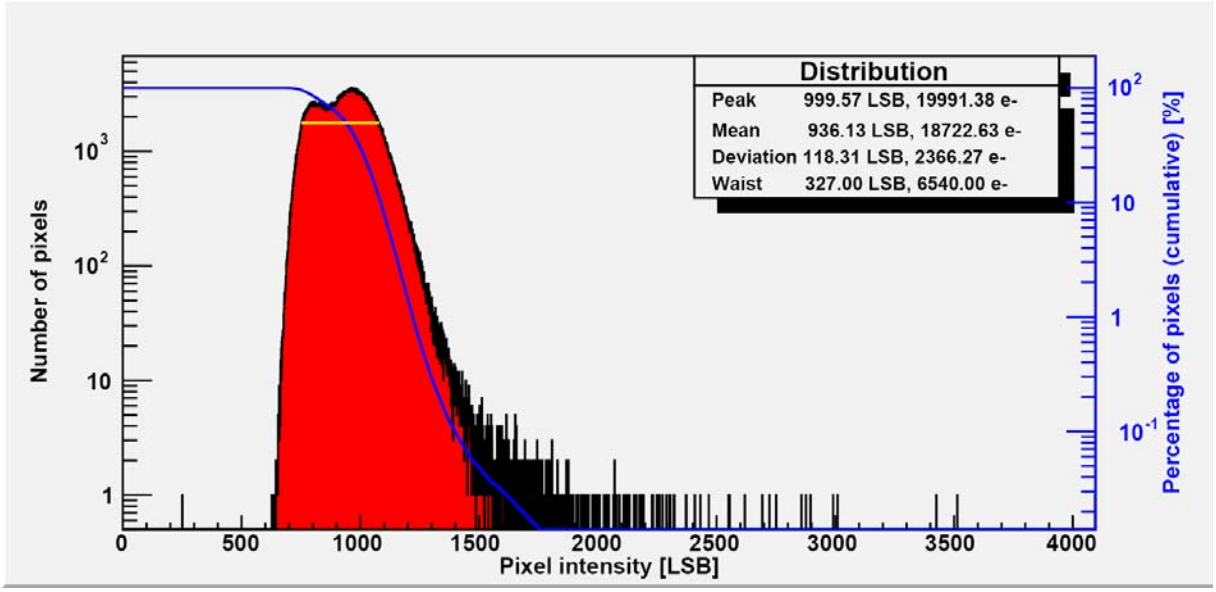

Figure 6-29 : D2 – 34 krad + 8 weeks annealing ON – dark current map and histogram

D3 – 34 krad + 8 weeks – Annealing OFF

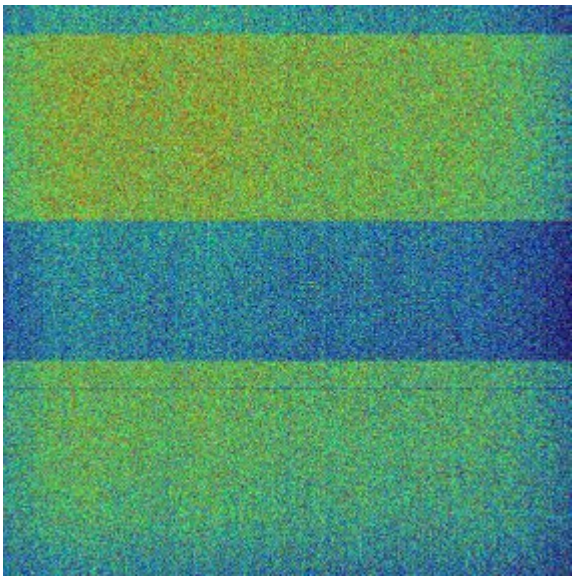

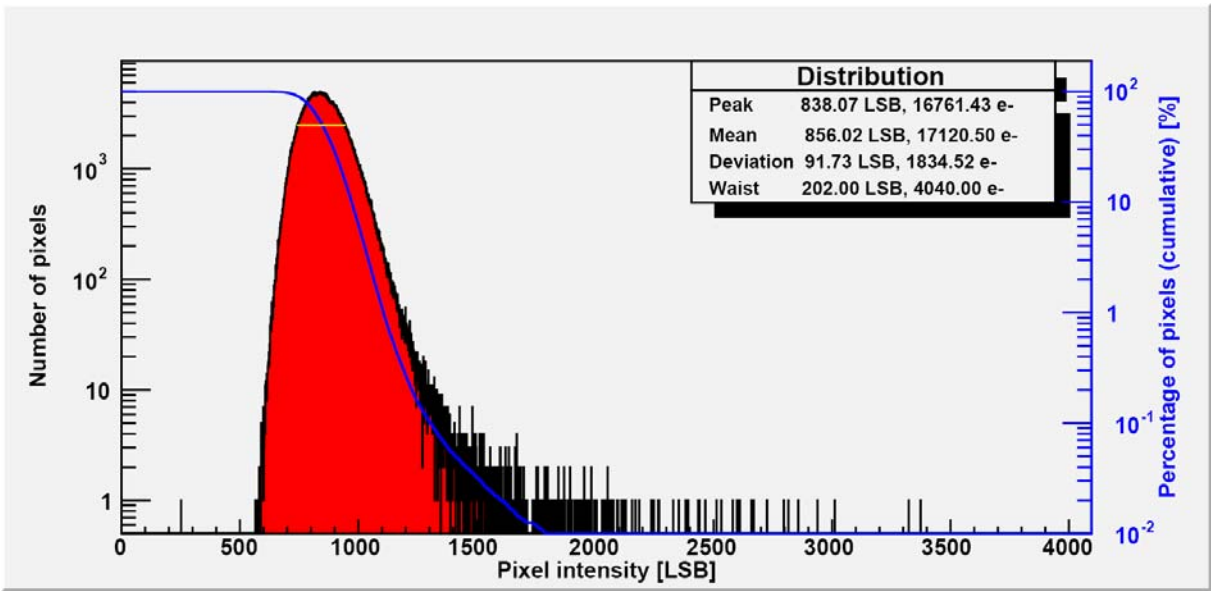

Figure 6-30 : D3 – 34 krad + 8 weeks annealing OFF – dark current map and histogram

D1 – 34 krad + 16 weeks– Annealing ON
Last 4 weeks at 50°C and operating in Full Frame dynamic readout

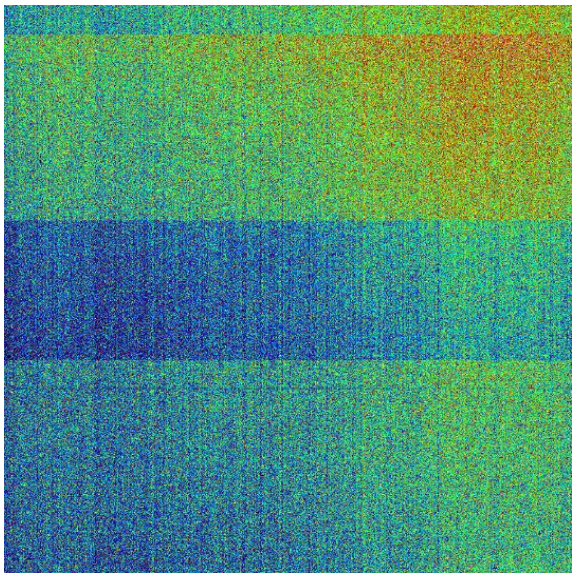

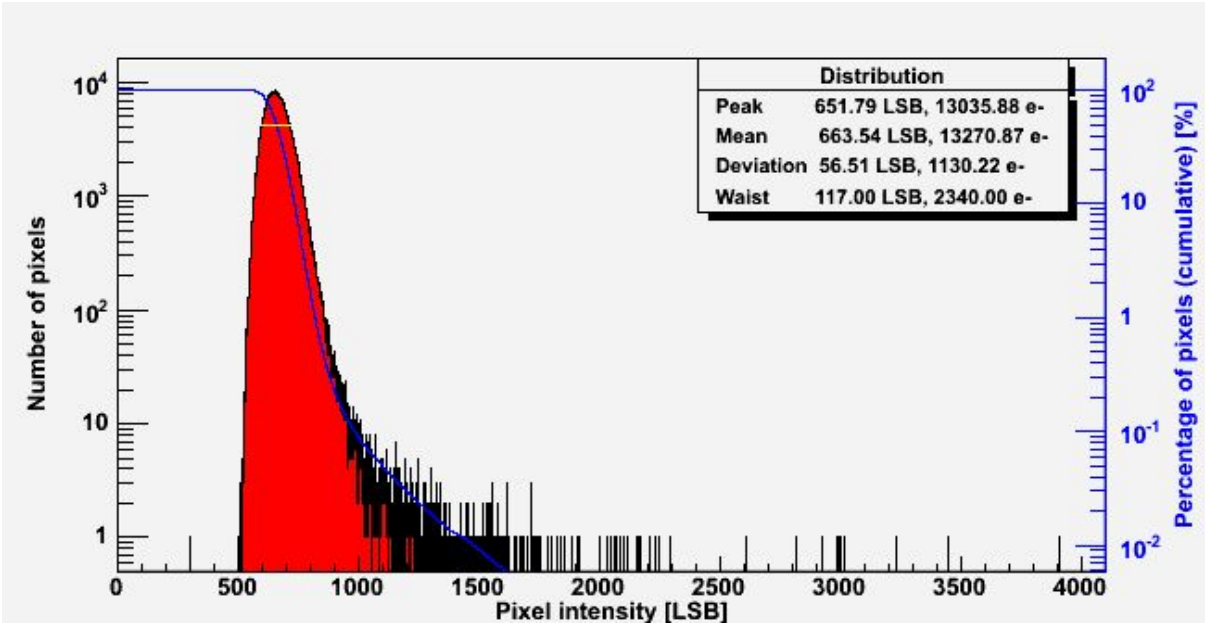

Figure 6-31 : D1 – 34 krad + 16 weeks (4 weeks at 50°C) annealing ON – dark current map and histogram

D2 – 34 krad + 16 weeks– Annealing ON
Last 4 weeks at 50°C biased and clocked on X register

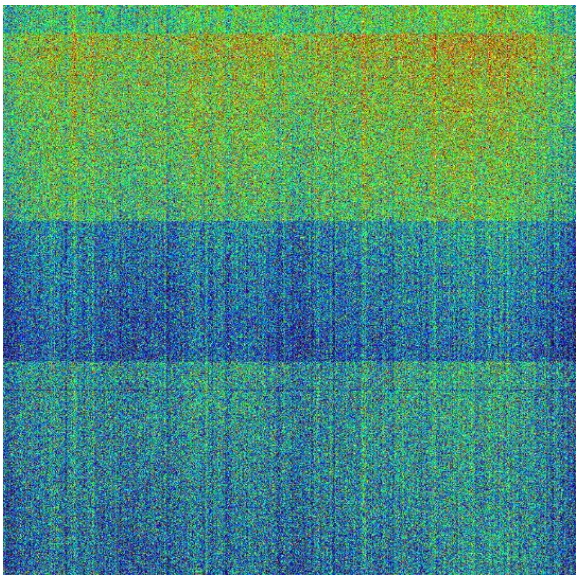

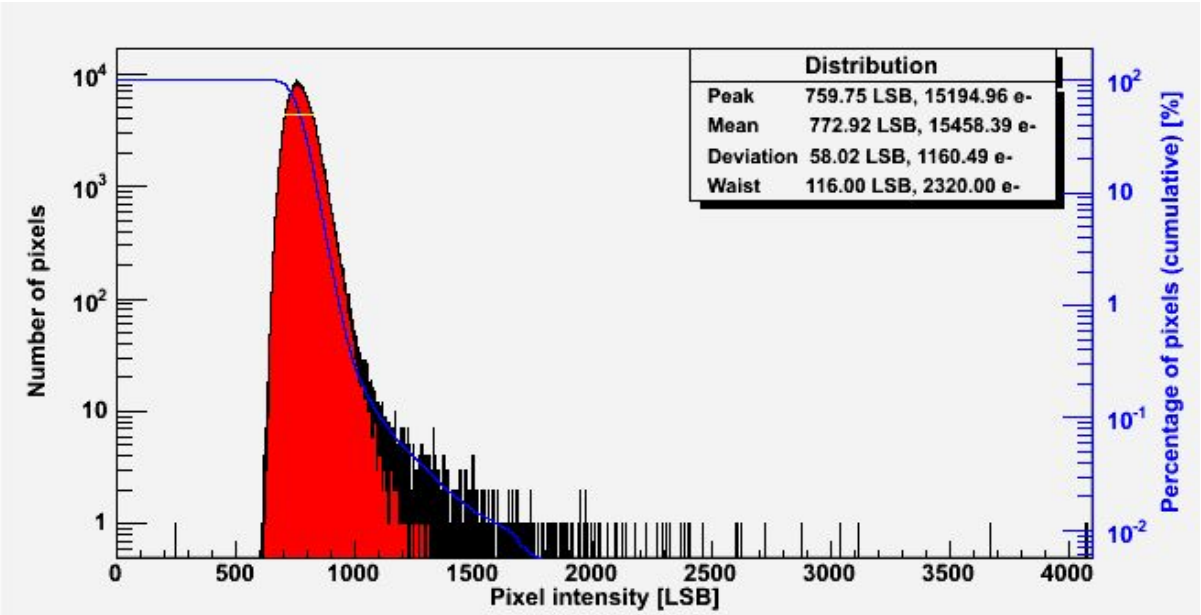

Figure 6-32 : D2 – 34 krad + 16 weeks (4 weeks at 50°C) annealing ON – dark current map and histogram

D3 – 34 krad + 16 weeks (4 weeks at 50°C) – Annealing OFF

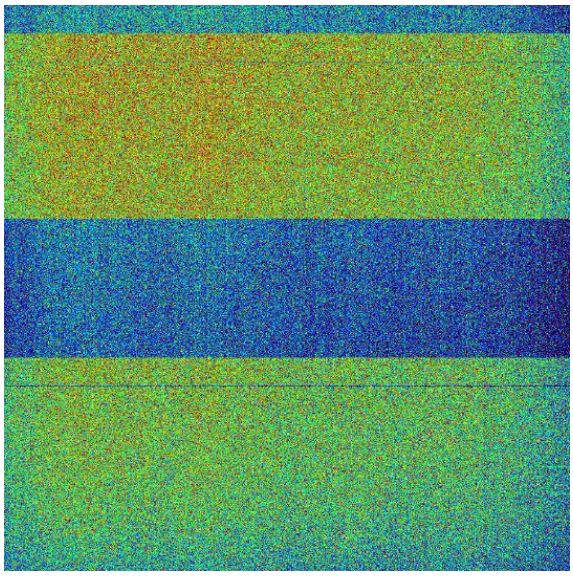

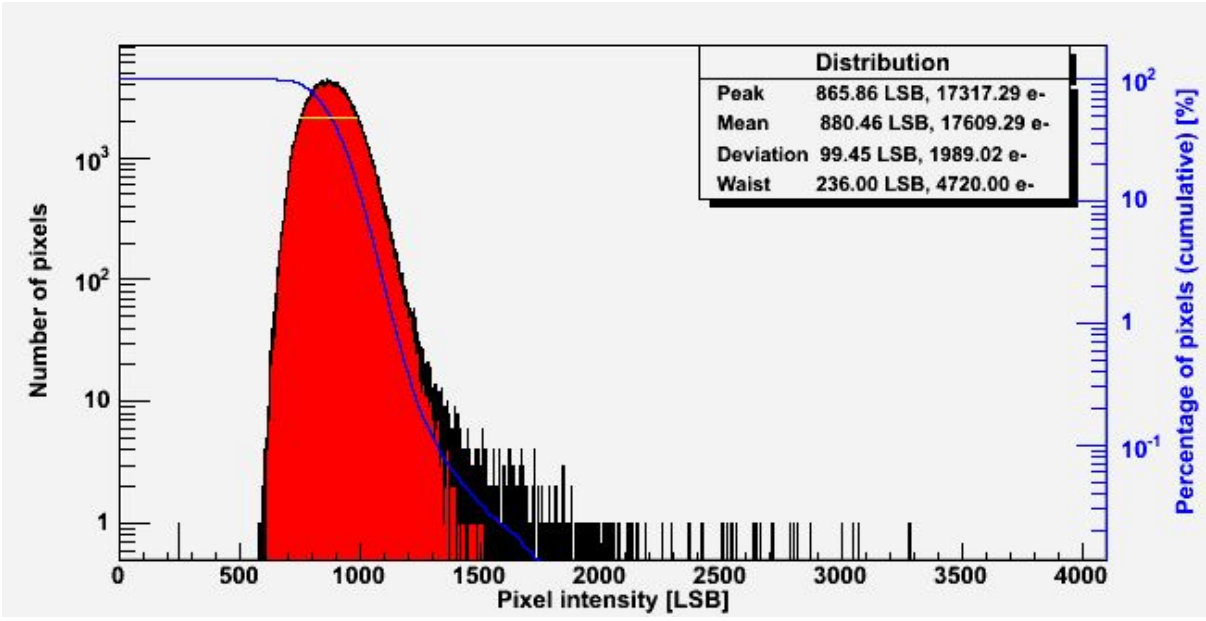

Figure 6-33 : D3 – 34 krad + 16 weeks (4 weeks at 50°C) annealing OFF – dark current map and histogram

7. SINGLE EVENT EFFECTS TEST CAMPAIGN

7.1. Tested samples

The 2 devices are HAS2 Engineering Models procured for the JUNO project with a specific assembly (wafer lot P20291.1). Sensor with serial number JUNO_15 (named detector D1) features a specific glass lid with a metallic mask (see section 7.4.1). Sensor with serial number JUNO_18 (named detector D2) features a bare die, without any cover lid. During a previous test campaign, this sensor had previously been exposed to a fluence of $4x10^7$ 60 MeV protons/cm². This low irradiation is considered to have no practical influence on the single event effects measurements.

7.2. Run list

For single event effects characterization, the runs presented in Table 7-1 were performed:

As can be seen in the table, three different sensor configurations were used:

- “Calibration”, aimed at the measurement of pulse frequency and fluence (see section 5.2.2). The sensor is irradiated in air, without glass lid.
- “SET”, aimed at the measurements of electron-induced direct ionization effects on the sensor. More details on the characterization methodology are presented in section 7.3.1.The sensor is irradiated in air, without glass lid.
- “Cerenkov”, aimed at the measurement of photonic secondary effects (Cerenkov and Luminescence). More details on the characterization methodology are presented in section 7.4.1. The sensor is irradiated in air, placed behind 9.5 mm of silica.

In-situ processing of the data showed that runs 2 to 21 were plagued by a small amount of parasitic light from the irradiation chamber. Parasitic light is not a concern for the calibration runs 2 to 7, but disturbs the SET and photonic effects measurements on runs 8 to 21. In consequence, runs 22 to 43 were performed again in total darkness.

Run	DUT	Mode	Integ. Time	Image #	Temp. (°C)	Energy (MeV)	Dose rate (UM/min)	Dose (UM)	Tilt (°)	Configuration/ Goal	Comments
2	2	DR	4	40	19	12	100	10	0	Calibration	Beam missed
3	2	DR	4	40	19	12	100	10	0	Calibration	Parasitic light
4	2	DR	4	40	19	22	100	10	0	Calibration	Parasitic light
5	2	DR	4	40	19	12	1000	100	0	Calibration	Parasitic light
6	2	DR	4	40	19	22	1000	100	0	Calibration	Beam missed
7	2	DR	4	40	19	22	1000	100	0	Calibration	Parasitic light
8	2	DR	130	40	19	12	100	10	0	SET	Parasitic light
9	2	NDR	2571840	80	19	22	100	10	0	SET	Parasitic light
10	2	NDR	2571840	80	19	12	100	10	0	SET	Parasitic light
11	2	DR	130	40	19	22	100	10	0	SET	Parasitic light
12	2	DR	30	40	19	12	1000	100	0	SET	Parasitic light
13	2	DR	30	40	19	22	1000	100	0	SET	Parasitic light
14	2	DR	130	40	19	12	100	10	28.5	SET	Parasitic light
15	2	NDR	2571840	80	19	22	100	10	28.5	SET	Parasitic light
16	2	NDR	2571840	80	19	12	100	10	28.5	SET	Parasitic light
17	2	DR	130	40	19	22	100	10	28.5	SET	Parasitic light
18	2	DR	30	40	19	12	1000	100	28.5	SET	Parasitic light
19	2	DR	30	40	19	22	1000	100	28.5	SET	Parasitic light
20	2	DR	130	40	19	12	100	10	0	Cerenkov	Wrong DUT
21	1	DR	130	40	19	12	100	10	0	Cerenkov	Parasitic light
22	1	DR	130	40	19	12	100	10	0	Cerenkov	
23	1	NDR	2571840	80	19	22	100	10	0	Cerenkov	
24	1	NDR	2571840	80	19	12	100	10	0	Cerenkov	
25	1	DR	130	40	19	22	100	10	0	Cerenkov	
26	1	DR	30	40	19	12	1000	100	0	Cerenkov	
27	1	DR	30	40	19	22	1000	100	0	Cerenkov	
28	2	DR	130	40	19	12	100	10	0	SET	
29	2	NDR	2571840	80	19	22	100	10	0	SET	
30	2	NDR	2571840	80	19	12	100	10	0	SET	
31	2	DR	130	40	19	22	100	10	0	SET	
32	2	DR	30	40	19	12	1000	100	0	SET	
33	2	DR	30	40	19	22	1000	100	0	SET	
34	2	DR	130	40	19	12	100	10	28.2	SET	
35	2	NDR	2571840	80	19	22	100	10	28.2	SET	
36	2	NDR	2571840	80	19	12	100	10	28.2	SET	
37	2	DR	130	40	19	22	100	10	28.2	SET	
38	2	DR	30	40	19	12	1000	100	28.2	SET	
39	2	DR	30	40	19	22	1000	100	28.2	SET	
40	1	DR	130	40	19	12	100	10	23.8	Cerenkov	
41	1	DR	130	40	19	22	100	10	23.8	Cerenkov	
42	1	DR	30	40	19	12	1000	100	23.8	Cerenkov	
43	1	DR	30	40	19	22	1000	100	23.8	Cerenkov	

Table 7-1: Run list for Single Event Effects characterization

The cumulative levels brought by the irradiations were computed in Table 7-2:

Run	Energy (MeV)	Dose (UM)	Configuration / Goal	Ionizing dose (Gy[water])	Ionizing dose (rad[Si])	Fluence (#/cm²)	NIEL (MeV .cm²/g)	Displacement damage dose (MeV/g)
2	12	10	Calibration	0.1	9.37	2.67E8	1.10E-4	2.94E4
3	12	10	Calibration	0.1	9.37	2.67E8	1.10E-4	2.94E4
4	22	10	Calibration	0.1	9.37	2.63E9	1.29E-4	3.39E5
5	12	100	Calibration	1.0	93.7	2.67E9	1.10E-4	2.94E5
6	22	100	Calibration	1.0	93.7	2.63E9	1.29E-4	3.39E5
7	22	100	Calibration	1.0	93.7	2.63E9	1.29E-4	3.39E5
8	12	10	SET	0.1	9.37	2.67E8	1.10E-4	2.94E4
9	22	10	SET	0.1	9.37	2.63E8	1.29E-4	3.39E4
10	12	10	SET	0.1	9.37	2.67E8	1.10E-4	2.94E4
11	22	10	SET	0.1	9.37	2.63E8	1.29E-4	3.39E4
12	12	100	SET	1.0	93.7	2.67E9	1.10E-4	2.94E5
13	22	100	SET	1.0	93.7	2.63E9	1.29E-4	3.39E5
14	12	10	SET	0.1	9.37	2.67E8	1.10E-4	2.94E4
15	22	10	SET	0.1	9.37	2.63E8	1.29E-4	3.39E4
16	12	10	SET	0.1	9.37	2.67E8	1.10E-4	2.94E4
17	22	10	SET	0.1	9.37	2.63E8	1.29E-4	3.39E4
18	12	100	SET	1.0	93.7	2.67E9	1.10E-4	2.94E5
19	22	100	SET	1.0	93.7	2.63E9	1.29E-4	3.39E5
20	8	10	Cerenkov	0.1	9.37	2.67E8	9.68E-5	2.58E4
21	8	10	Cerenkov	0.1	9.37	2.67E8	9.68E-5	2.58E4
22	8	10	Cerenkov	0.1	9.37	2.67E8	9.68E-5	2.58E4
23	18	10	Cerenkov	0.1	9.37	2.63E8	1.24E-4	3.26E5
24	8	10	Cerenkov	0.1	9.37	2.67E8	9.68E-5	2.58E4
25	18	10	Cerenkov	0.1	9.37	2.63E8	1.24E-4	3.26E5
26	8	100	Cerenkov	1.0	93.7	2.67E9	9.68E-5	2.58E5
27	18	100	Cerenkov	1.0	93.7	2.63E9	1.24E-4	3.26E6
28	12	10	SET	0.1	9.37	2.67E8	1.10E-4	2.94E4
29	22	10	SET	0.1	9.37	2.63E8	1.29E-4	3.39E4
30	12	10	SET	0.1	9.37	2.67E8	1.10E-4	2.94E4
31	22	10	SET	0.1	9.37	2.63E8	1.29E-4	3.39E4
32	12	100	SET	1.0	93.7	2.67E9	1.10E-4	2.94E5
33	22	100	SET	1.0	93.7	2.63E9	1.29E-4	3.39E5
34	12	10	SET	0.1	9.37	2.67E8	1.10E-4	2.94E4
35	22	10	SET	0.1	9.37	2.63E8	1.29E-4	3.39E4
36	12	10	SET	0.1	9.37	2.67E8	1.10E-4	2.94E4
37	22	10	SET	0.1	9.37	2.63E8	1.29E-4	3.39E4
38	12	100	SET	1.0	93.7	2.67E9	1.10E-4	2.94E5
39	22	100	SET	1.0	93.7	2.63E9	1.29E-4	3.39E5
40	8	10	Cerenkov	0.1	9.37	2.67E8	9.68E-5	2.58E4
41	18	10	Cerenkov	0.1	9.37	2.63E8	1.24E-4	3.26E5
42	8	100	Cerenkov	1.0	93.7	2.67E9	9.68E-5	2.58E5
43	18	100	Cerenkov	1.0	93.7	2.63E9	1.24E-4	3.26E6
Total		1770	-	17.7	1.66E3	-	-	5.80E6

Table 7-2: Cumulative levels induced by the irradiations

7.3. Single Event Transients

7.3.1. Methodology

As charged particles impinge on the sensor, they will create tracks of electron-hole pairs that will appear as parasitic transients on the images. The main goal of the single event transient tests is to measure the average signal created by the electrons, and to infer the charge collection layer thickness of the detector from these measurements.

The epitaxial layer thickness of the HAS2 is estimated at 6 µm, which should roughly correspond to the charge collection layer thickness. In the 10-20 MeV energy range, the expected mean signal on a pixel hit by an electron is about:

LET (e-/µm) x *thickness* (µm) x *diffusion factor* = 110 x 6 x 0.58 = 383 electrons = 19.2 LSB

LET value is taken from ESTAR collision stopping power [RD 4], with an average energy of 3.6 eV needed to create an electron-hole pair.

Depending on the beam and the environment conditions, the temporal noise of the test bench is characterized by a standard deviation value ranging from 3.25 LSB to 5.5 LSB. In consequence, in most of the cases the electron signal will be too weak to be correctly detected and measured.

A better way to characterize the mean electron signal is to accumulate several hits on each pixel, in order to raise the signal above the noise floor. The expected fluence per pulse is presented in Table 5-3 for a sensor positioned 5 cm away from the applicator end. Expressing this fluence in terms of hits on an 18 x 18 µm² pixel gives the following results:

	Dose rate	Energy	Tilt	Avg. time b/w pulses	Hits per pulse
RUN 28	100 UM/min	12 MeV	0°	56.4 ms	8.14 e-/pixel
RUN 31	100 UM/min	22 MeV	0°	62.0 ms	8.82 e-/pixel
RUN 32	1000 UM/min	12 MeV	0°	6.2 ms	8.64 e-/pixel
RUN 33	1000 UM/min	22 MeV	0°	6.4 ms	9.10 e-/pixel
RUN 34	100 UM/min	12 MeV	28.2°	56.4 ms	7.17 e-/pixel
RUN 37	100 UM/min	22 MeV	28.2°	62.0 ms	7.77 e-/pixel
RUN 38	1000 UM/min	12 MeV	28.2°	6.2 ms	7.61 e-/pixel
RUN 39	1000 UM/min	22 MeV	28.2°	6.4 ms	8.02 e-/pixel

Table 7-3: CLINAC 1 pixel hits per pulse for in different configurations

The exposition to a single pulse in the reference position is sufficient to raise the signal level well above the noise floor.

For 1000 UM/min (10 Gy[water]/min) dose rate, the pulse frequency increases by a factor 10. The integration time of the sensor can be tuned so that focal plane array pixels are exposed to a single or double pulse during their integration time. This phenomenon is illustrated for an integration time of 30 lines (8 ms) in Figure 7-1.

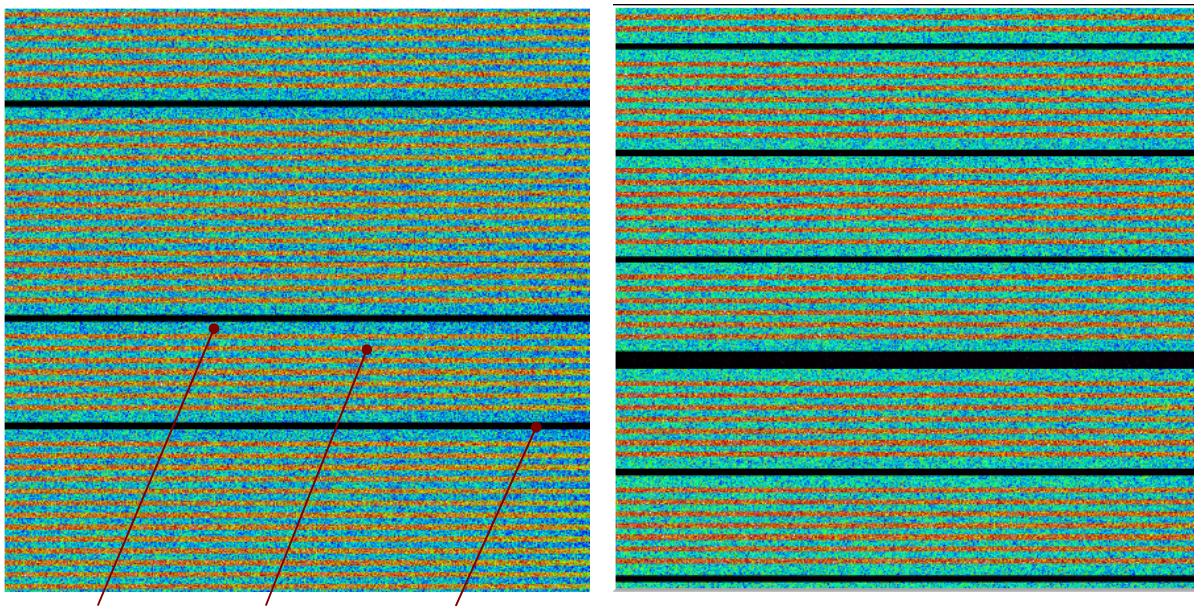

Figure 7-1: Full frame DR image 1000 UM/min, 12 MeV (left), 22 MeV (right)

One can see overlapping stripes on the images, corresponding to zones that were exposed never, once or twice to the accelerator pulses. In case of double pulses, the number of hits per pixel becomes:

- 12 MeV, double pulses: 17.28 hits per pixel
- 22 MeV, double pulses: 18.20 hits per pixel.

Double pulses will give additional information on the mean electron signal.

SET characterization runs were performed on bare sensors, with the glass lid removed. The incident particle energy loss in air is considered negligible. Irradiation and characterization are performed at room temperature (19°C).

7.3.2.Experimental data

7.3.2.1.Data processing overview

Single event transient data analysis was performed on sequences recorded in DR mode. On each run, five images recorded under the beam were selected. These images were systematically chosen 5 images after the start of the irradiation, to ensure that the CLINAC 1 had reached a stable state (see section 5.2.2).

On these images, DR electrical offset and FPN was subtracted using the averaged values of pixel to pixel offsets from the final images of the run (recorded while the beam was turned off). The averaging is typically performed on 10 frames, which leads to a residual noise on the FPN image of ~1.3 LSB.

For each analyzed run, more than 20 pulses were averaged in order to compute their mean intensity distribution. The results are presented over the next sections.

7.3.2.2.Run 28: 12 MeV electrons, 100 UM/min, normal incidence, 19°C

Processing parameters:

- Processed images: from #10 to #15
- Number of averaged pulses: 24

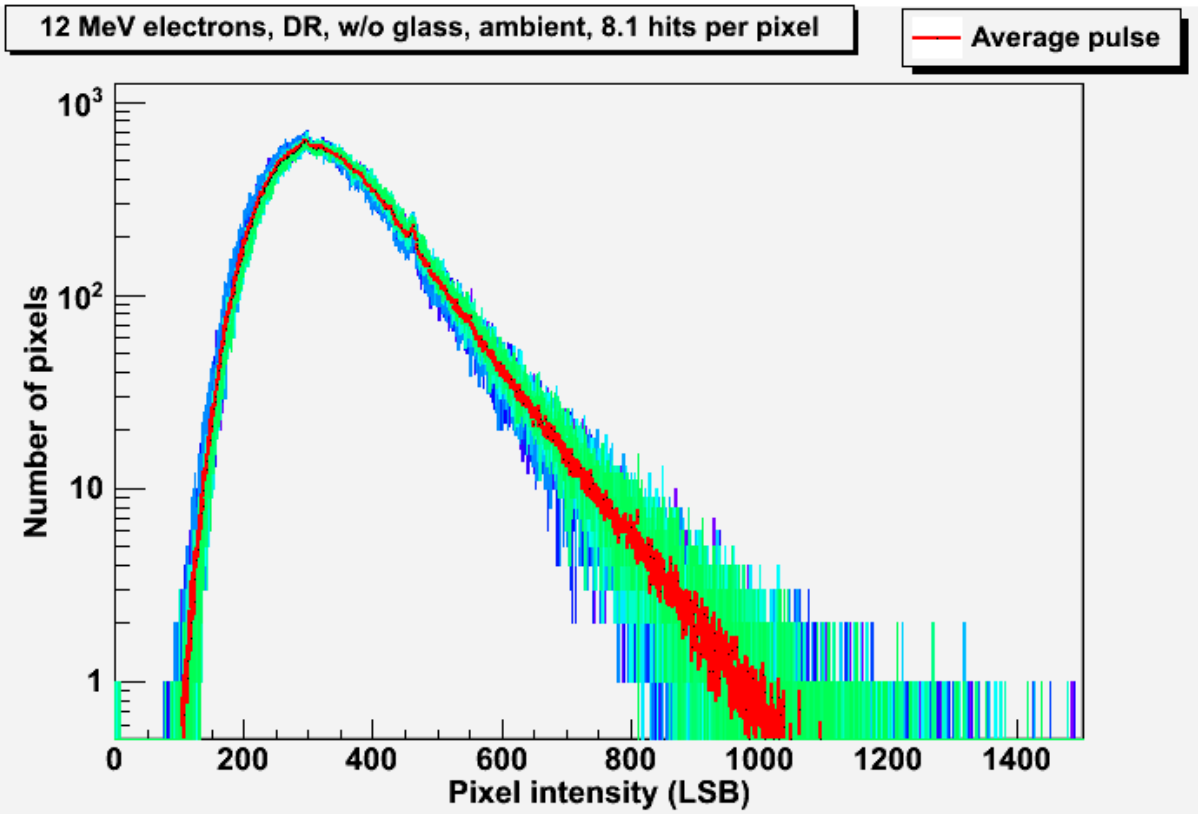

Figure 7-2: Mean electron pulse distribution at 12 MeV, 100 UM/min, normal incidence

7.3.2.3.Run 31: 22 MeV electrons, 100 UM/min, normal incidence, 19°C

Processing parameters:

- Number of images processed: from #10 to #15
- Number of averaged pulses: 23

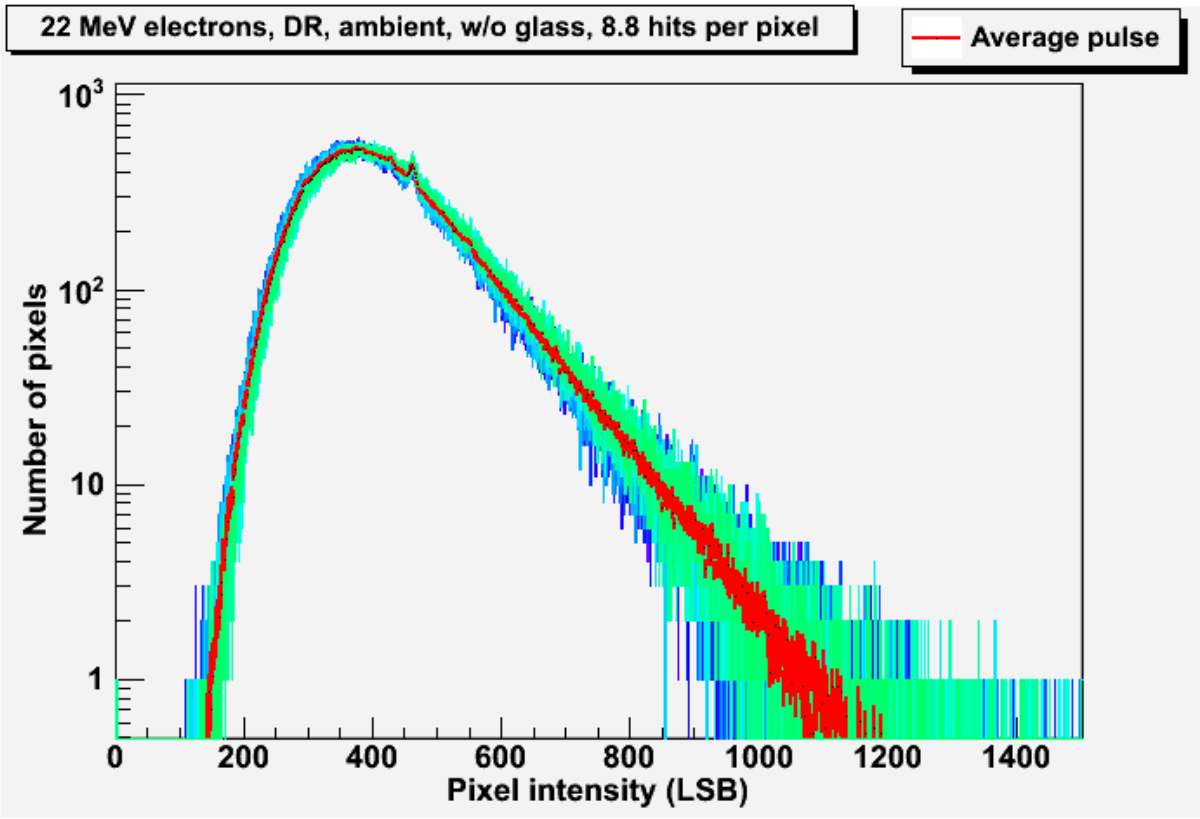

Figure 7-3: Mean electron pulse distribution at 22 MeV, 100 UM/min, normal incidence

7.3.2.4.Run 32: 12 MeV electrons, 1000 UM/min, normal incidence, 19°C

Processing parameters:

- Number of images processed: from #5 to #10
- Number of averaged pulses: 482

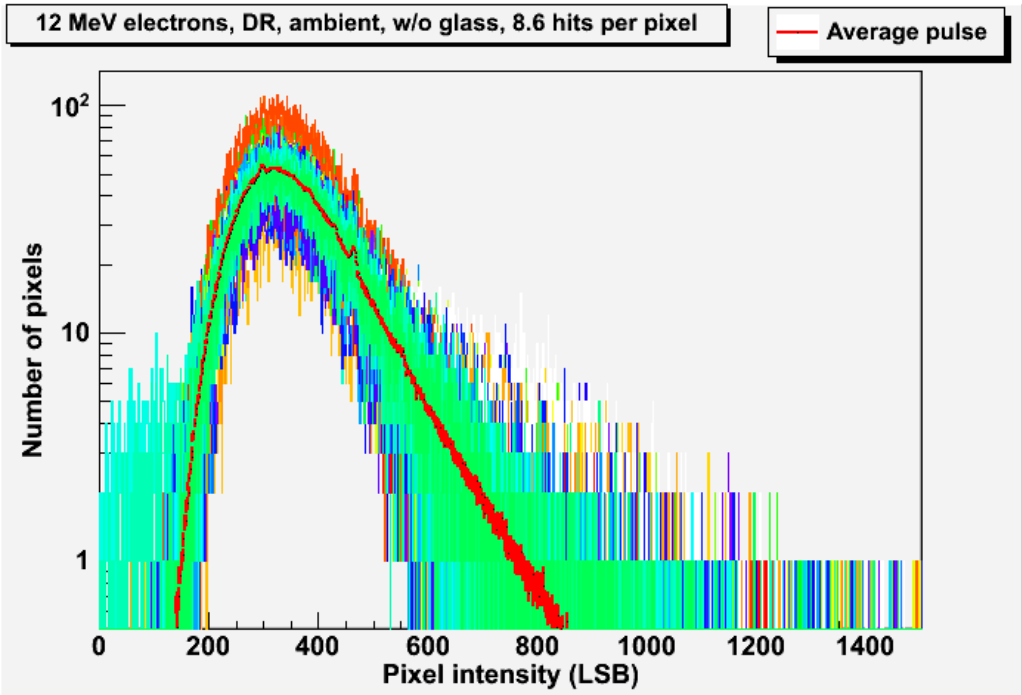

Figure 7-4: Mean electron single pulse at 12 MeV, 1000 UM/min, norm. incidence

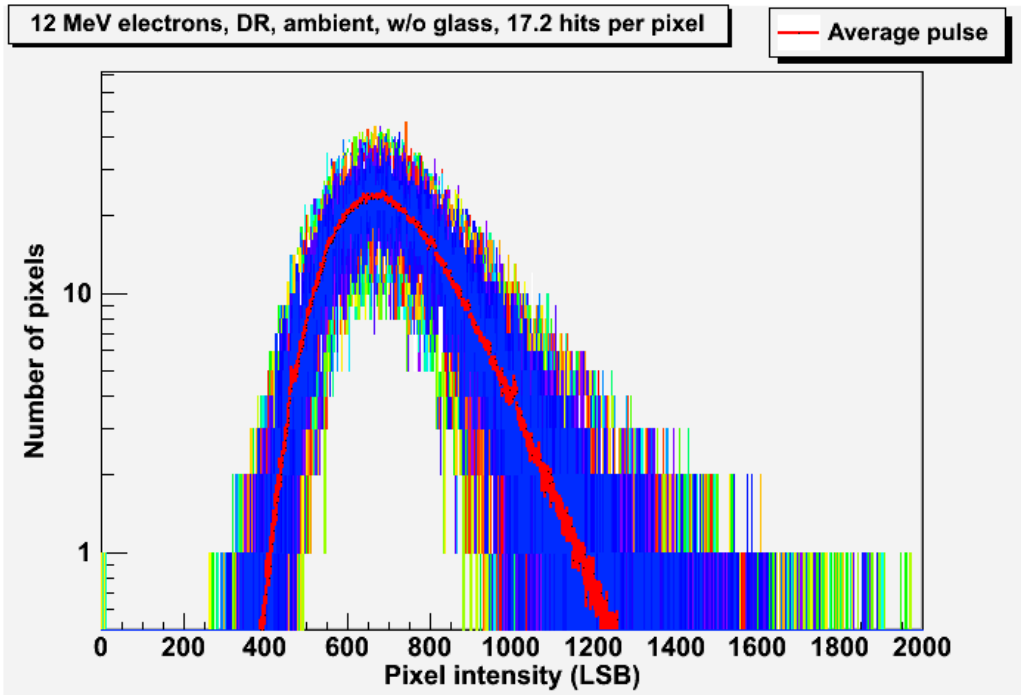

Figure 7-5: Mean electron double pulse at 12 MeV, 1000 UM/min, norm. incidence

7.3.2.5.Run 33: 22 MeV electrons, 1000 UM/min, normal incidence, 19°C

Processing parameters:

- Number of images processed: from #5 to #10
- Number of averaged pulses: 445

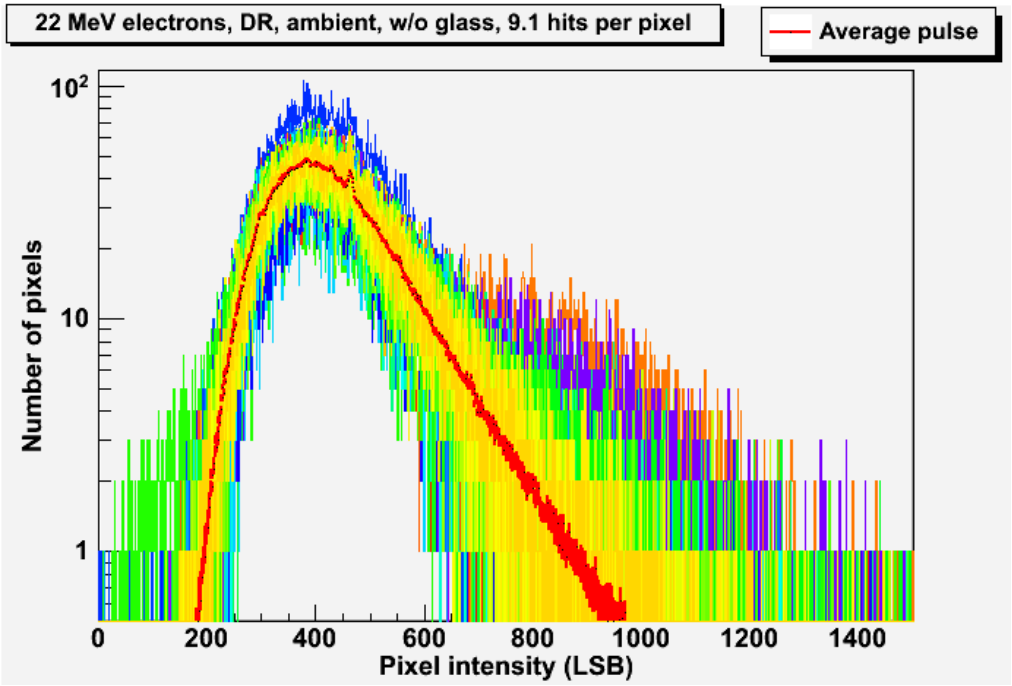

Figure 7-6: Mean electron single pulse at 22 MeV, 1000 UM/min, norm. incidence

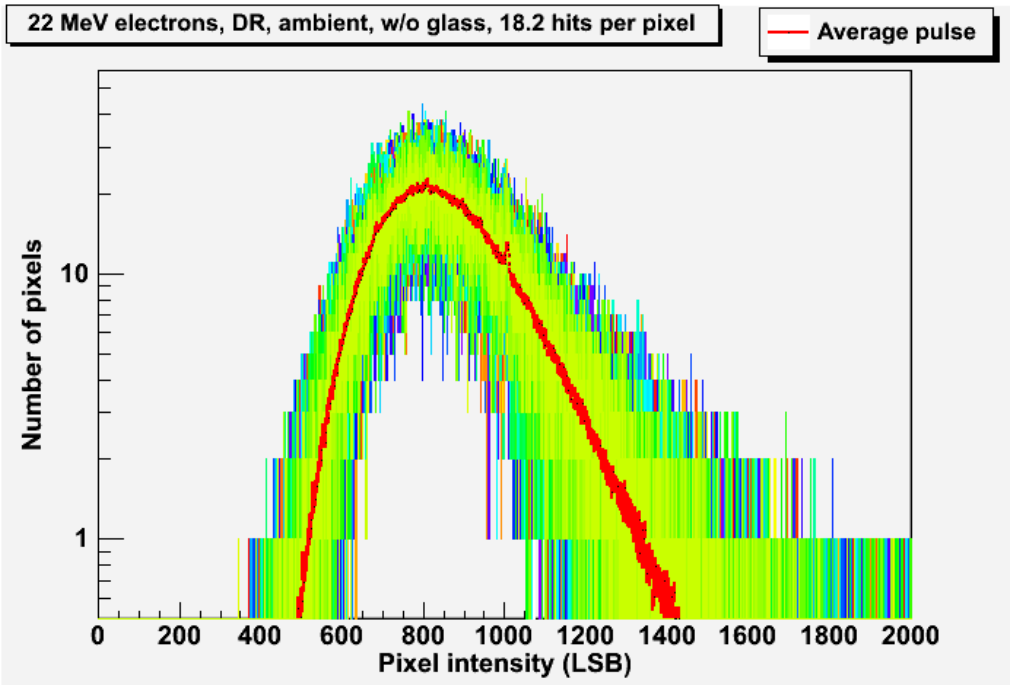

Figure 7-7: Mean electron double pulse at 22 MeV, 1000 UM/min, norm. incidence

7.3.2.6.Run 34: 12 MeV electrons, 100 UM/min, 28.2° tilt, 19°C

Processing parameters:

- Number of images processed: from #10 to #15
- Number of averaged pulses: 24

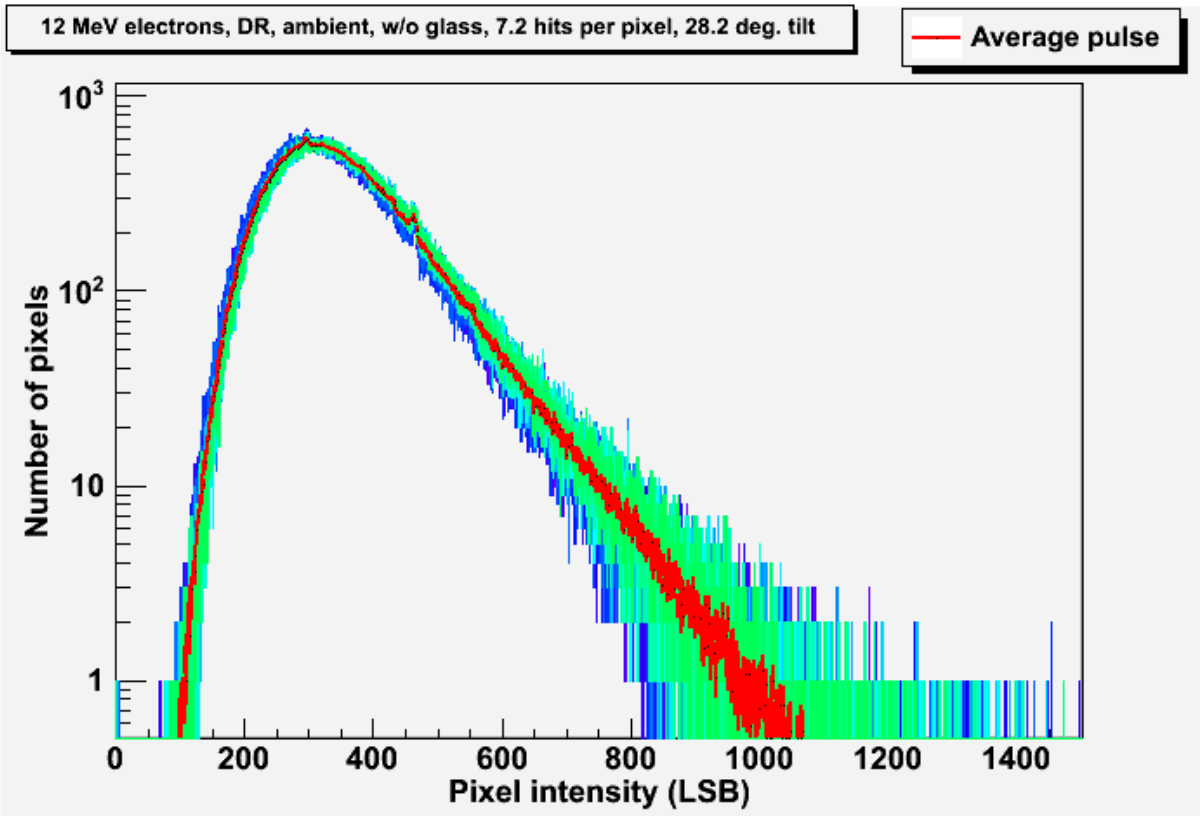

Figure 7-8: Mean electron pulse distribution at 12 MeV, 100 UM/min, 28.2° tilt

7.3.2.7.Run 37: 22 MeV electrons, 100 UM/min, 28.2° tilt, 19°C

Processing parameters:

- Number of images processed: from #10 to #15
- Number of averaged pulses: 21

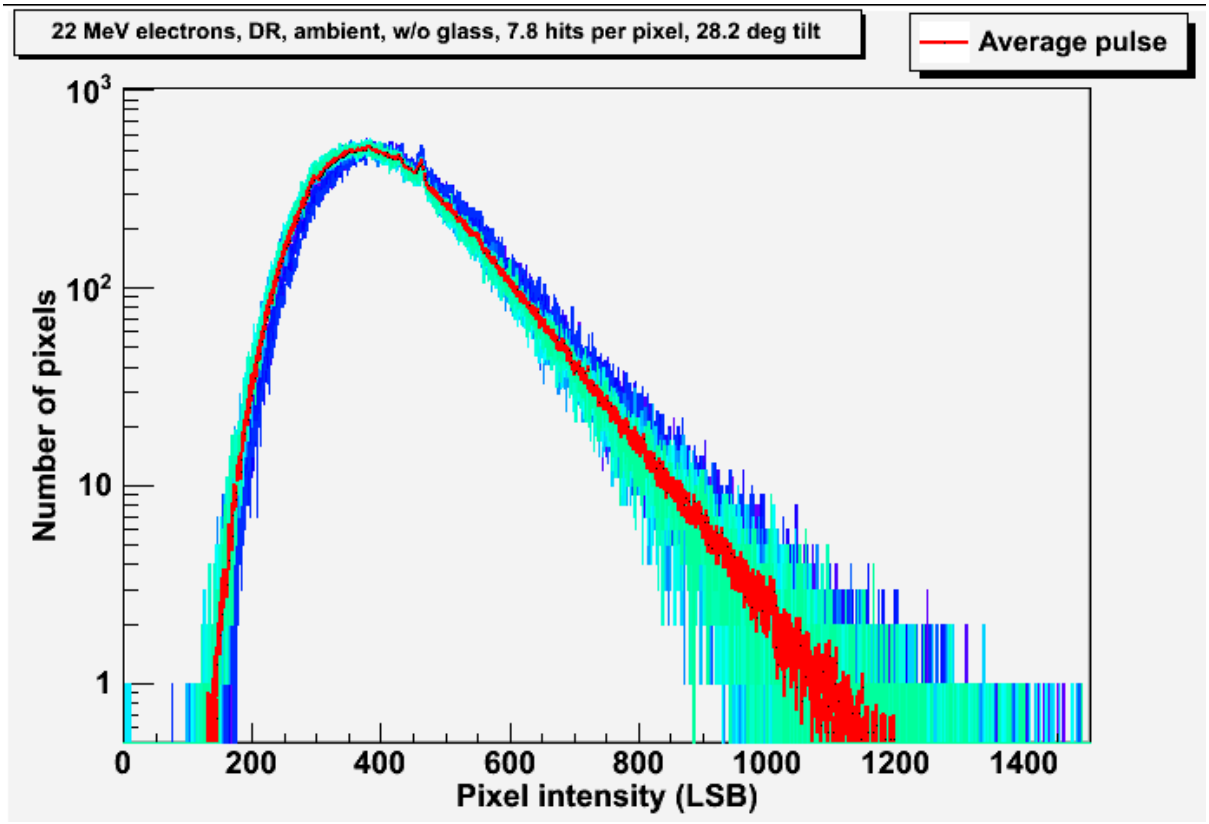

Figure 7-9: Mean electron pulse distribution at 22 MeV, 100 UM/min, 28.2° tilt

7.3.2.8.Run 38: 12 MeV electrons, 1000 UM/min, 28.2° tilt, 19°C

Processing parameters:

- Number of images processed: from #5 to #9
- Number of averaged pulses: 370

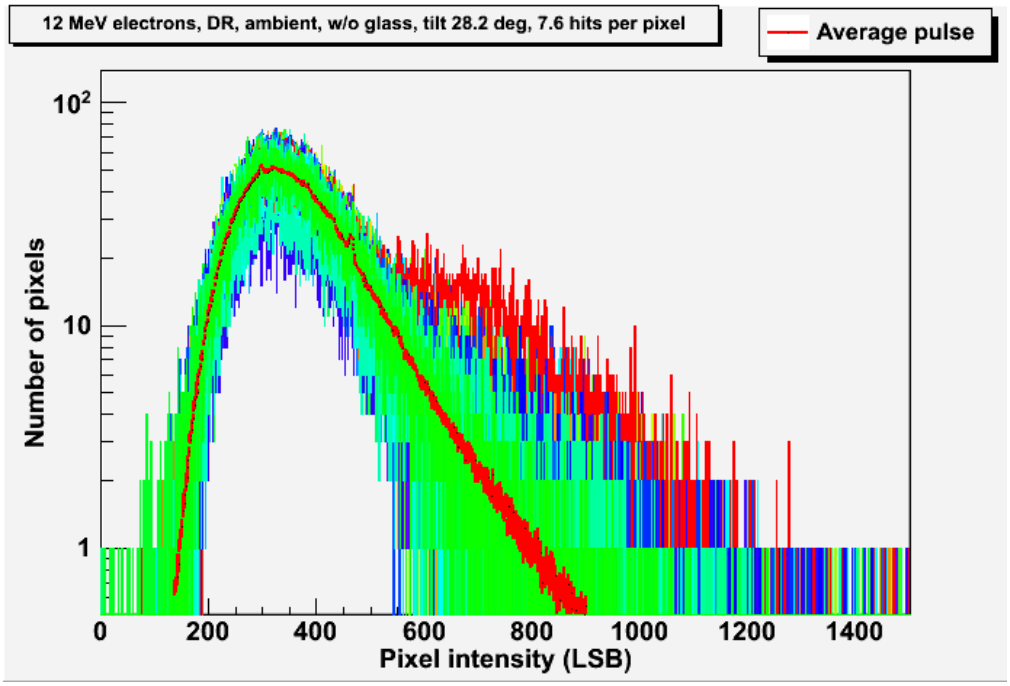

Figure 7-10: Mean electron single pulse at 12 MeV, 1000 UM/min, 28.2° tilt

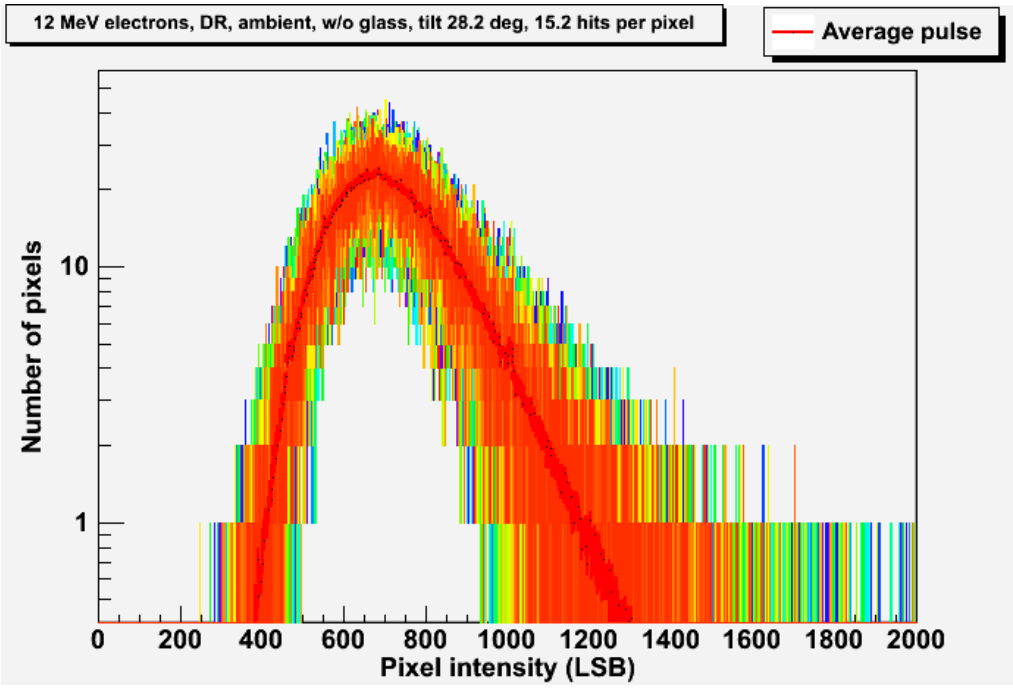

Figure 7-11: Mean electron double pulse at 12 MeV, 1000 UM/min, 28.2° tilt

7.3.2.9.Run 39: 22 MeV electrons, 1000 UM/min, 28.2° tilt, 19°C

Processing parameters:

- Number of images processed: from #5 to #10
- Number of averaged pulses: 432

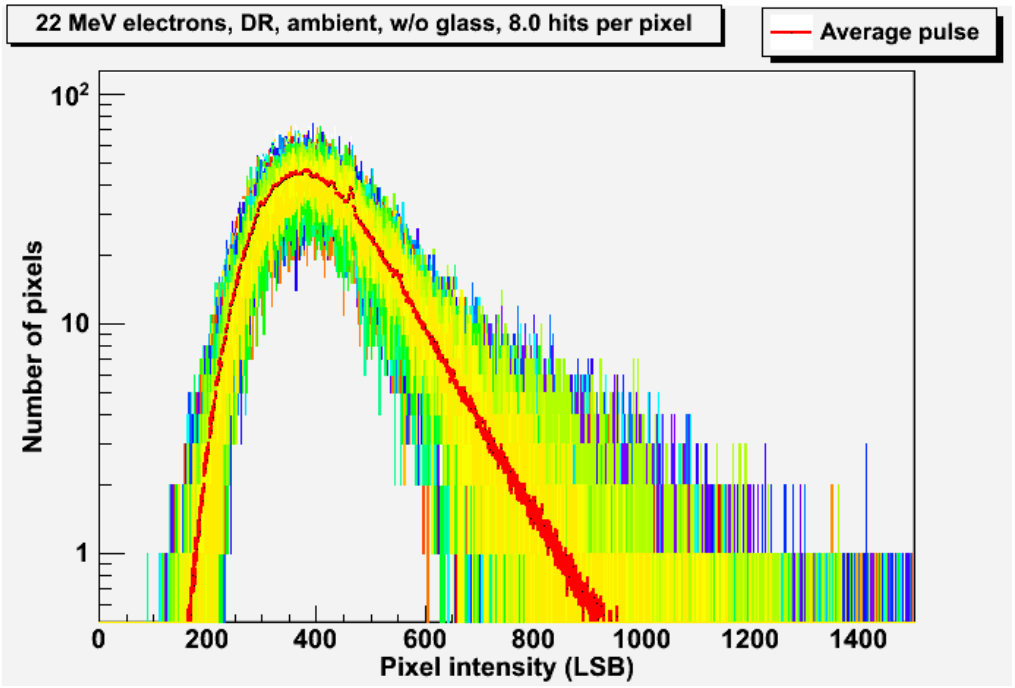

Figure 7-12: Mean electron single pulse at 22 MeV, 1000 UM/min, 28.2° tilt

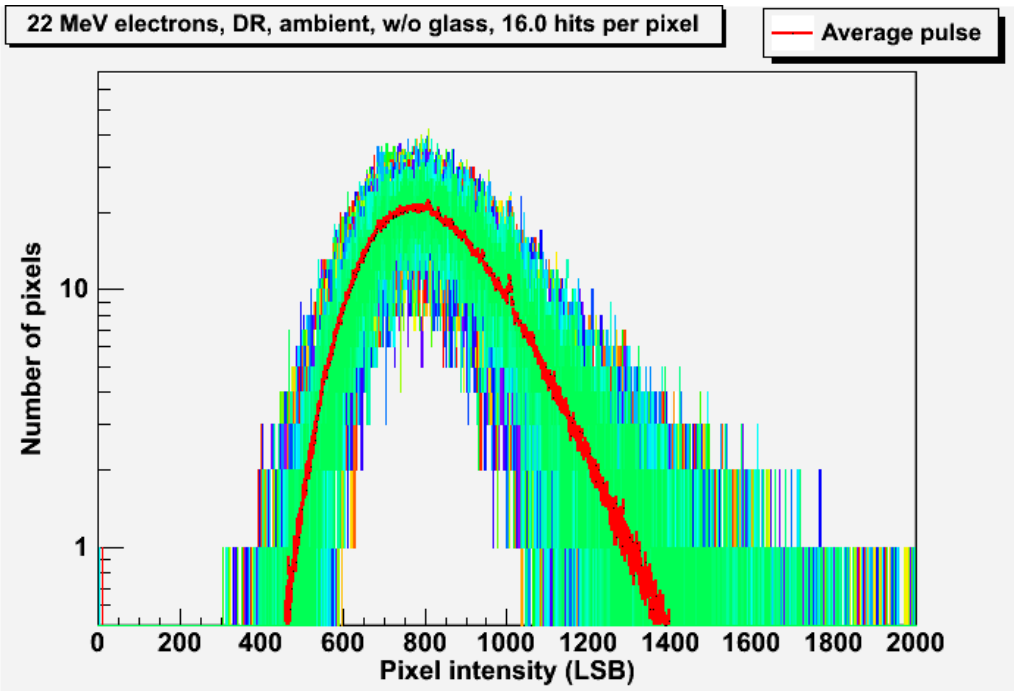

Figure 7-13: Mean electron double pulse at 22 MeV, 1000 UM/min, 28.2° tilt

7.3.2.10.Summary

Finally, Figure 7-14, Figure 7-15, and Figure 7-16 compare the average pulse distributions in the different configurations.

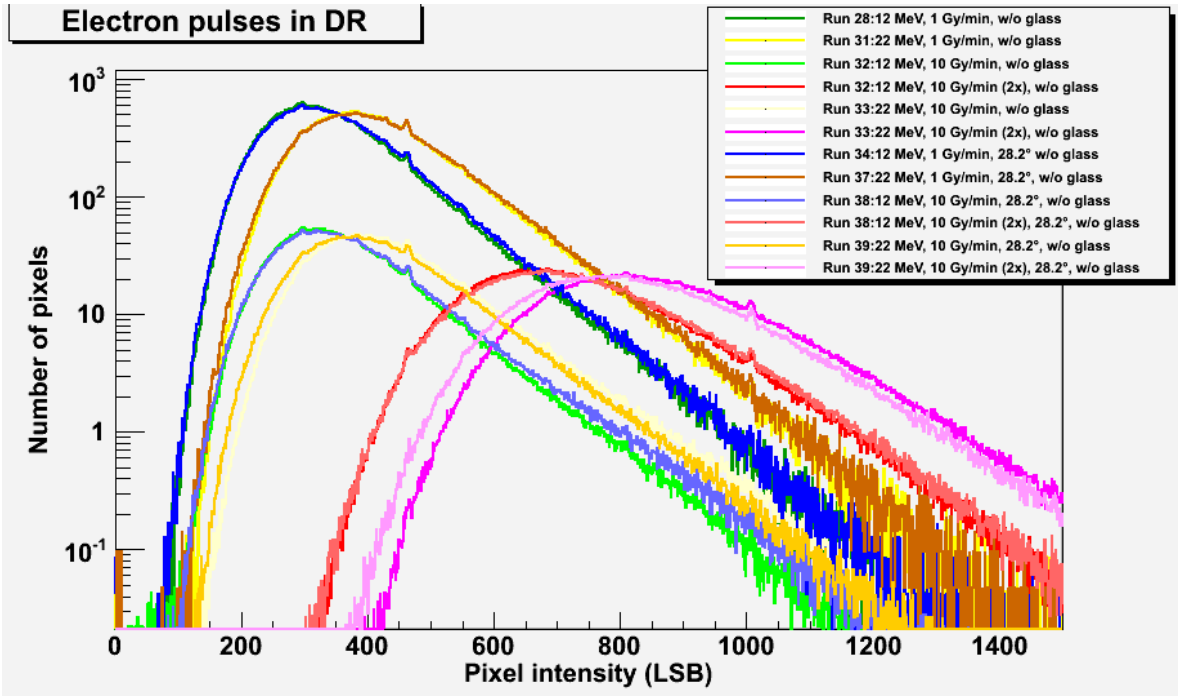

Figure 7-14: Mean electron pulse distributions in DR mode (combined view)

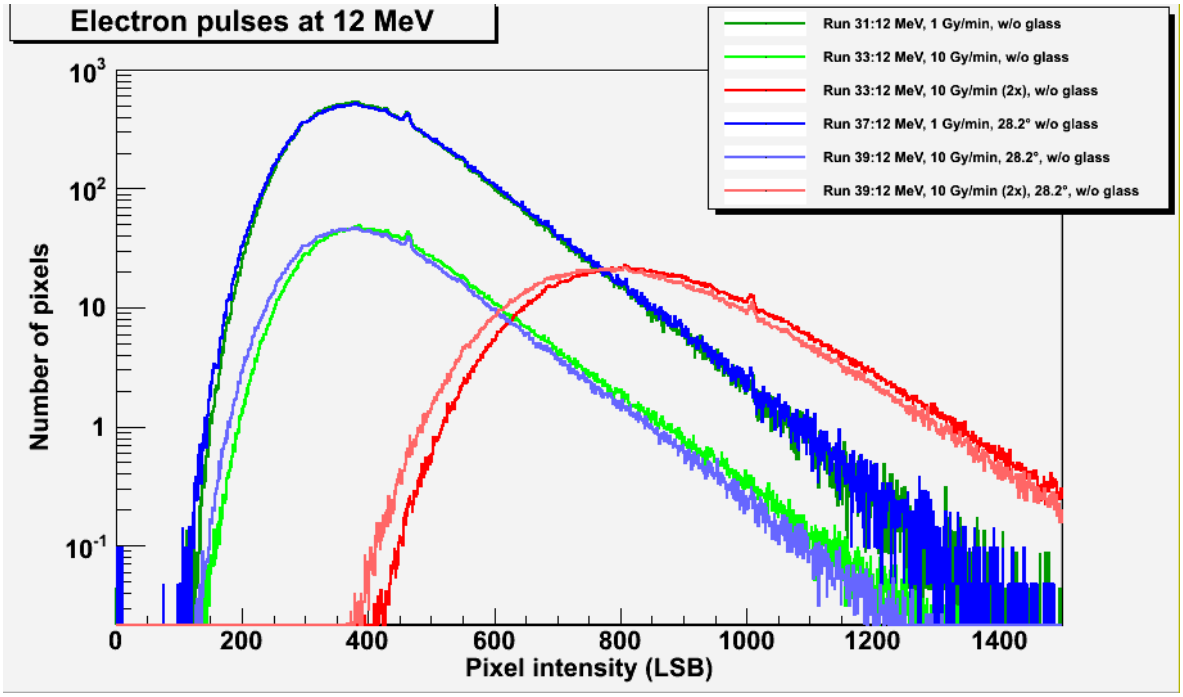

Figure 7-15: Mean electron pulse distributions in DR mode (12 MeV)

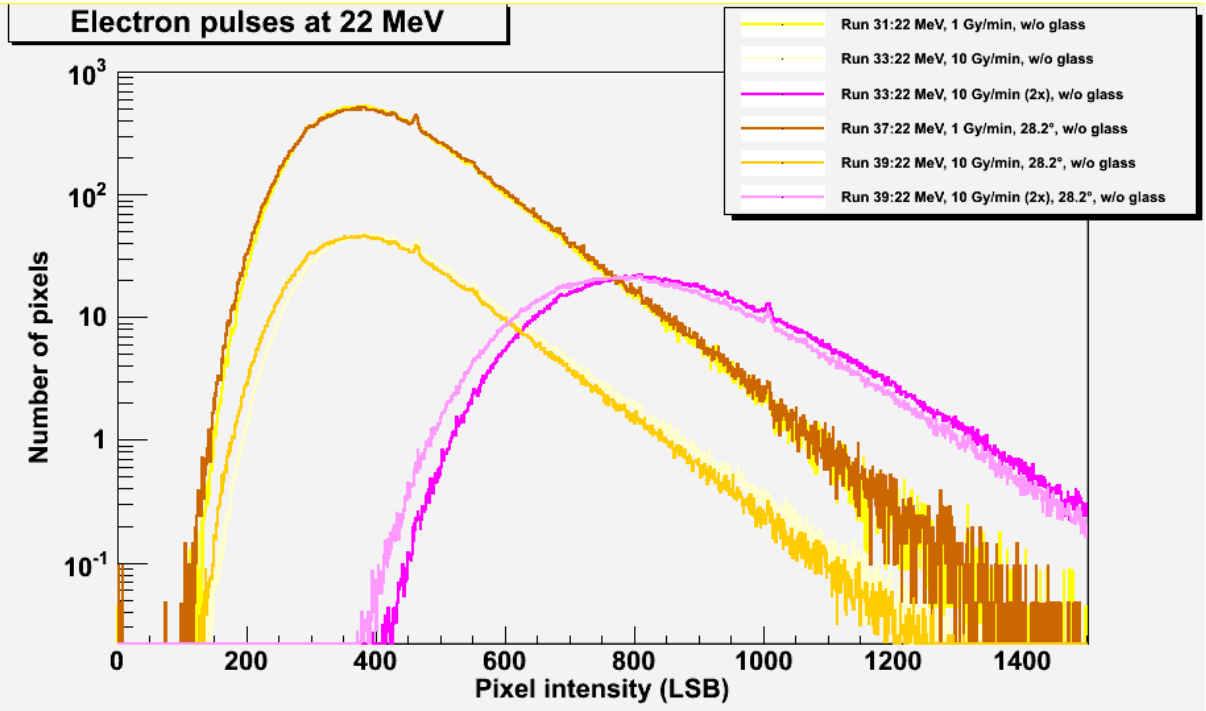

Figure 7-16: Mean electron pulse distributions in DR mode (22 MeV)

7.3.3.Analysis

7.3.3.1.Mean LET and Poisson distribution with diffusion

7.3.3.1.1.Data analysis overview

The most direct way to analyze the data is to consider that each electron hit generates the same amount of signal **H**. As in section 7.3.1, the average amount of signal is given by:

$$H = \frac{LET \times \rho \times t}{E_{e-h}}$$

In which:

- LET is the Linear Energy Transfer taken from the collision stopping power from ESTAR [RD 4],
- ρ is the density of silicon (2.33 g/cm^3),
- t is the path length in the charge collection layer,
- $E_{e\text{-}h}$ is the mean energy needed to create an electron-hole pair in silicon (3.6 eV)

In a pulse, each pixel is hit multiple times. The number of electrons impinging on a pixel during the integration time is characterized by a homogenous Poisson process:

- events are independent from each others,
- the average number of hits per pixel is known and constant, as the electron flux in a pulse is also known and constant.

The random variable representing the number of hits on a given pixel during a pulse will be designated as **X**.

The probability of a pixel being hit **n** times follows a Poisson distribution such as:

$$P(X = n) = \frac{\lambda^n e^{-\lambda}}{n!}$$

with λ being the average number of hits per pixel, computed in section 7.3.1.

As an example, the Poisson distribution for λ=10 hits per pixels is as follows:

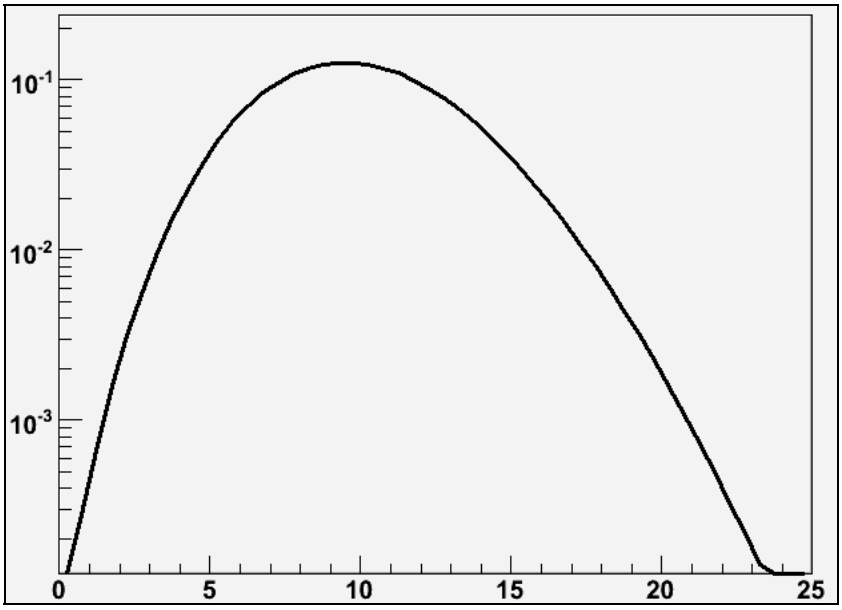

Figure 7-17: Poisson distribution for λ = 10

The distribution of the expected numbers of hits on **k** pixels of the sensor can be obtained by generating k times a random number based on the previous Poisson distribution.

As an example, the expected distribution of the number of hits X for λ=10 on the whole focal plane array (1024x1024 pixels) is as follows:

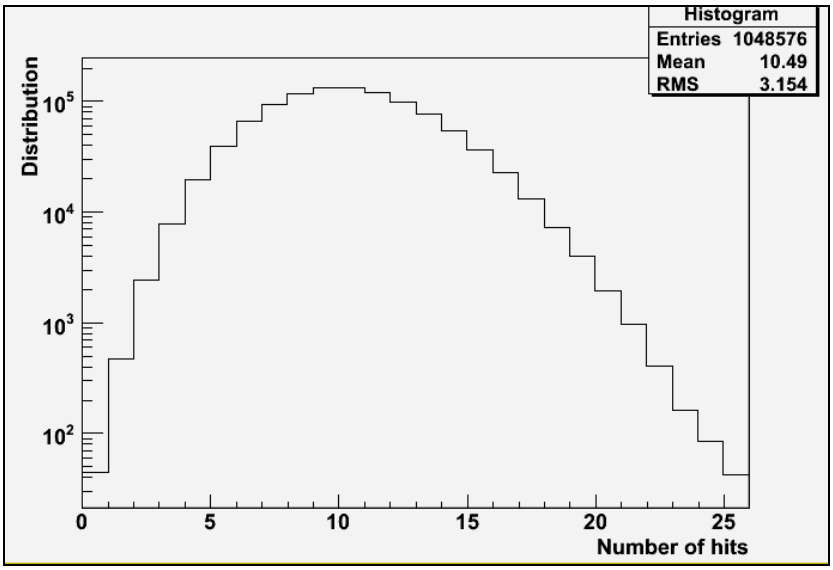

Figure 7-18: 1024x1024 distribution generated with Poisson law

The usual properties of the Poisson distribution are verified:

- Mean (μ) = λ
- Standard deviation (σ or RMS on the plots) = $\sqrt{\lambda}$

The signal level **S** is simply the product of the signal per electron H and of the number of electron hits X on a given pixel:

$$S = X \times H$$

As an example, we will take H = 30 LSB (see section 7.3.1). For a 1024x1024 focal plane array, the expected signal level distribution with λ=10 is therefore:

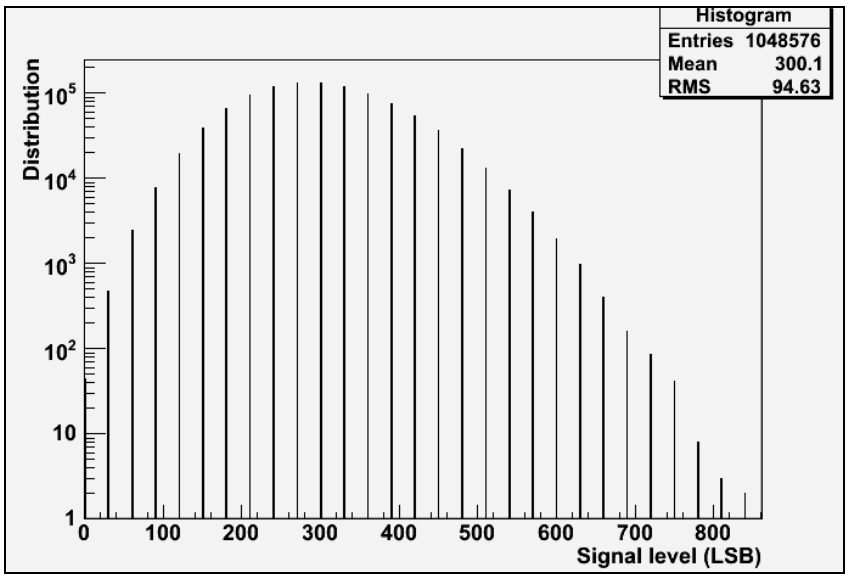

Figure 7-19: Signal level distribution generated by Poisson law

In this distribution, the Poisson distribution properties on standard deviation are still verified:
$\sigma = \sqrt{\lambda} \times H$

The charges generated by the incident electron diffuse in the substrate before being collected by the photodiodes. As the pixels are not isolated between each other, this causes a significant cross-talk in the surrounding pixels. We will use the simplified interpixel diffusion pattern for light to model the process:

2.5 %	8.0 %	2.5 %
8.0 %	58 %	8.0 %
2.5 %	8.0 %	2.5 %

Figure 7-20: HAS simplified interpixel diffusion pattern for light

The pattern has been obtained at Sodern using a laser spot: it is slightly different from the performance announced in [RD 1] which was made using a knife-edge.

When applying the interpixel diffusion process to the signal distribution previously computed for λ=10, the following distribution is obtained:

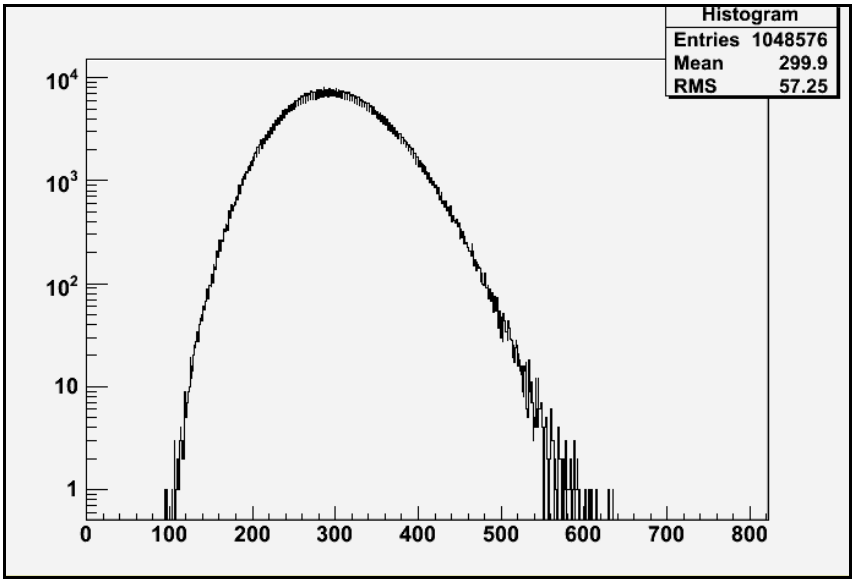

Figure 7-21: Signal level distribution generated by Poisson law and interpixel diffusion

These steps allow us to generate the theoretical Poisson signal distributions for every run. The number of exposed pixels (linked to integration time, section 5.2.2) and the average number of electron hits per pixel (computed in section 7.3.1) are known. The only unknown parameter is the mean signal per electron, which will be assessed by fitting the theoretical distributions to the experimental distributions presented in section 7.3.2. This will finally allow us to compute the average charge collection depth.

7.3.3.1.2.Run 28: 12 MeV electrons, 100 UM/min, normal incidence, 19°C

Analysis parameters:

- mean number of hits: 8.14 per pixel
- signal at distribution peak: 317.4 LSB
- corresponding signal per electron: 39 LSB
- corresponding charge collection thickness: 6.84 µm

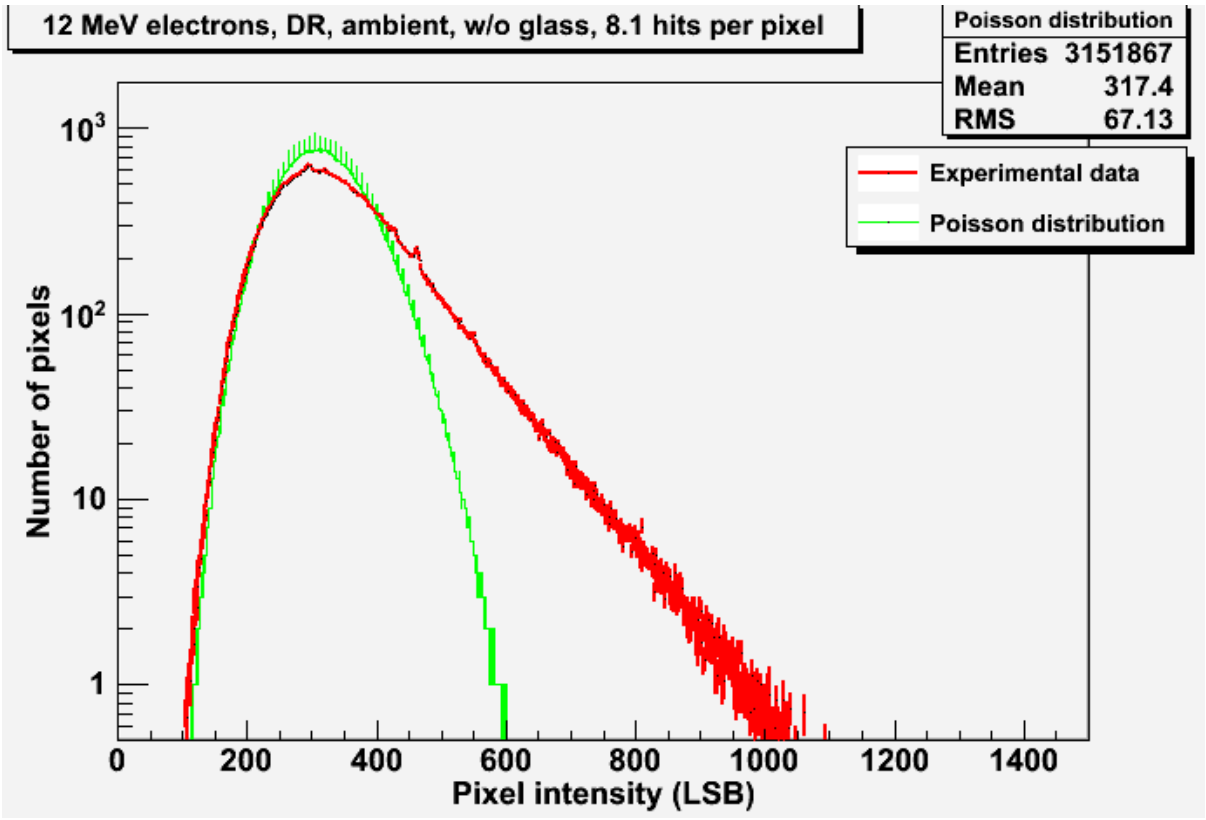

Figure 7-22: Mean electron pulse distribution at 12 MeV, 100 UM/min, normal incidence compared to theoretical Poisson distribution

7.3.3.1.3.Run 31: 22 MeV electrons, 100 UM/min, normal incidence, 19°C

Analysis parameters:

- mean number of hits: 8.8 per pixel
- signal at distribution peak: 379.3 LSB
- corresponding signal per electron: 43 LSB
- corresponding charge collection thickness: 7.17 µm

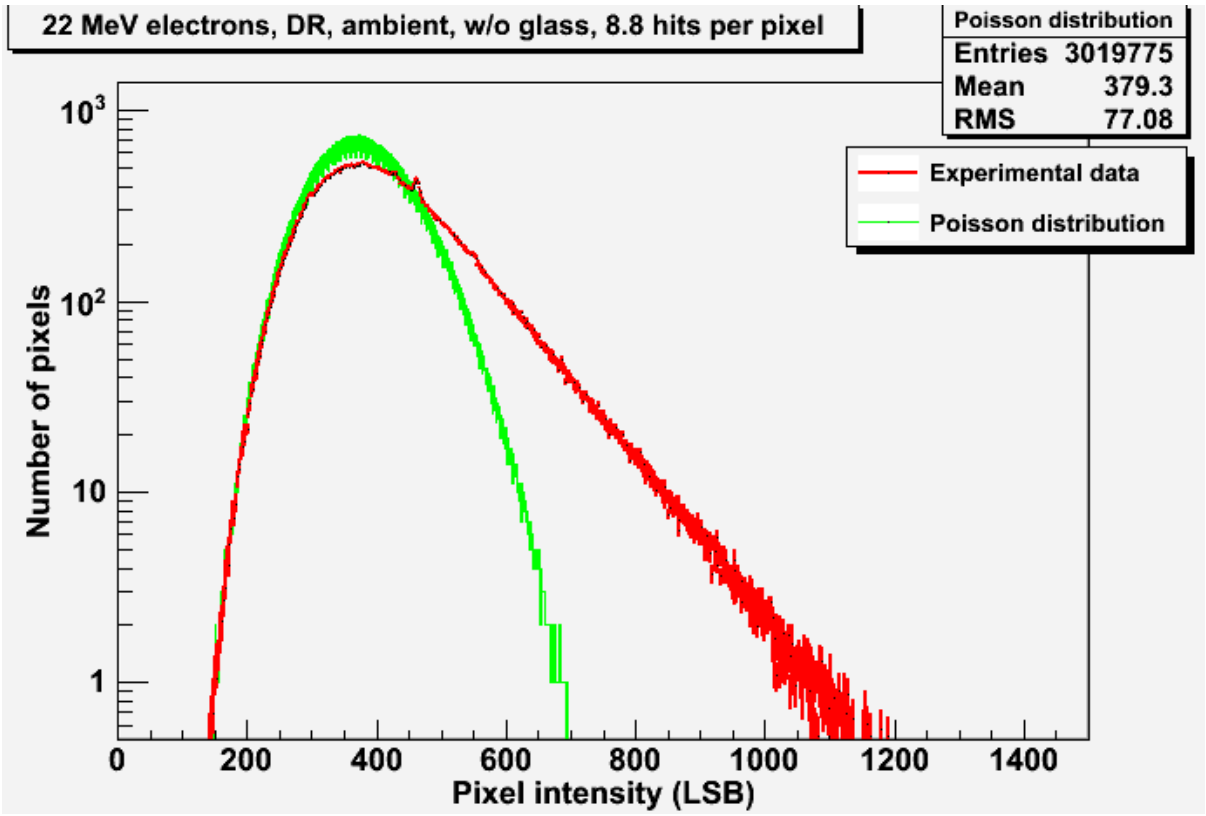

Figure 7-23: Mean electron pulse distribution at 22 MeV, 100 UM/min, normal incidence compared to theoretical Poisson distribution

7.3.3.1.4.Run 32: 12 MeV electrons, 1000 UM/min, normal incidence, 19°C

Analysis parameters:

- mean number of hits: 8.6 per pixel (x1), 17.2 per pixel (x2)
- signal at distribution peak: 343.4 LSB (1x), 686.8 LSB (2x)
- corresponding signal per electron: 40 LSB
- corresponding charge collection thickness: 7.02 µm

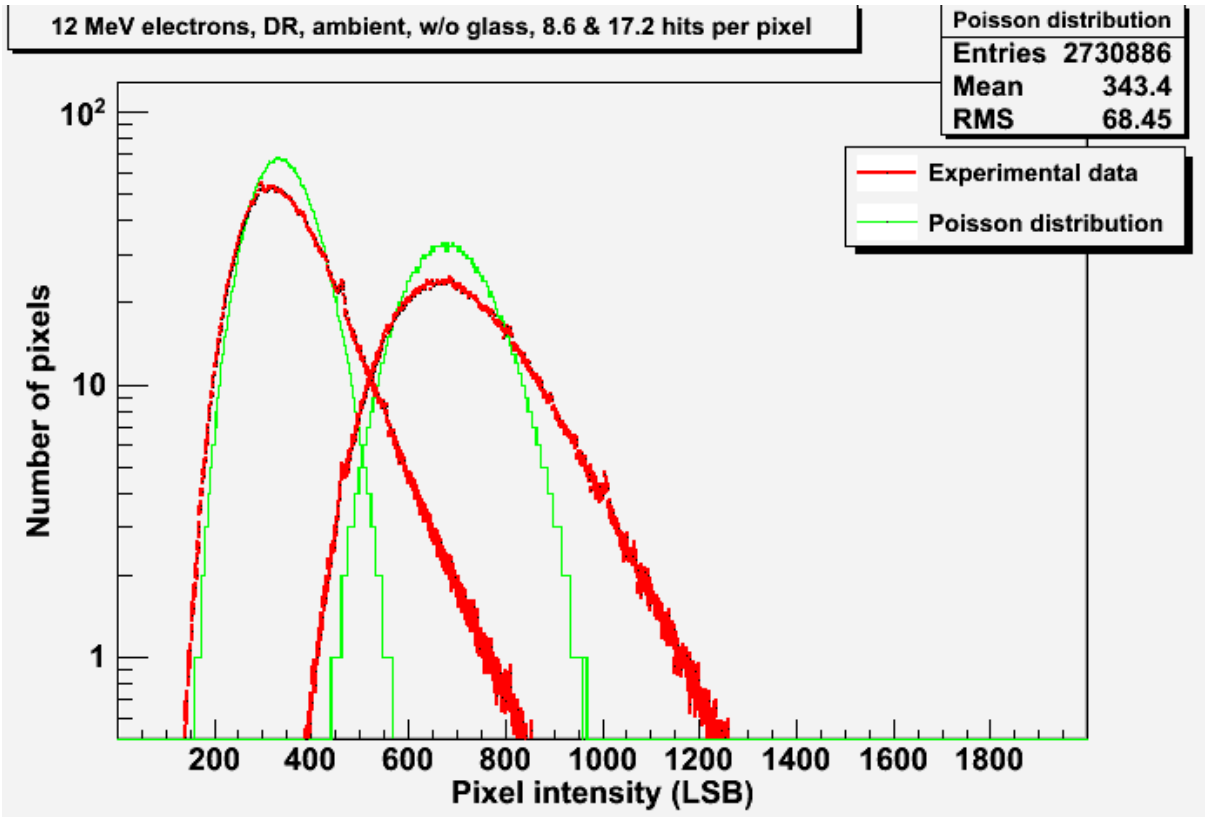

Figure 7-24: electron single pulse and double pulse distributions at 12 MeV, 1000 UM/min, normal incidence compared to theoretical Poisson distribution

7.3.3.1.5.Run 33: 22 MeV electrons, 1000 UM/min, normal incidence, 19°C

Analysis parameters:

- mean number of hits: 9.1 (1x),18.2 (2x)
- signal at distribution peak: 399.5 LSB (1x), 799 LSB (2x)
- corresponding signal per electron: 43 LSB
- corresponding charge collection thickness: 7.33 µm

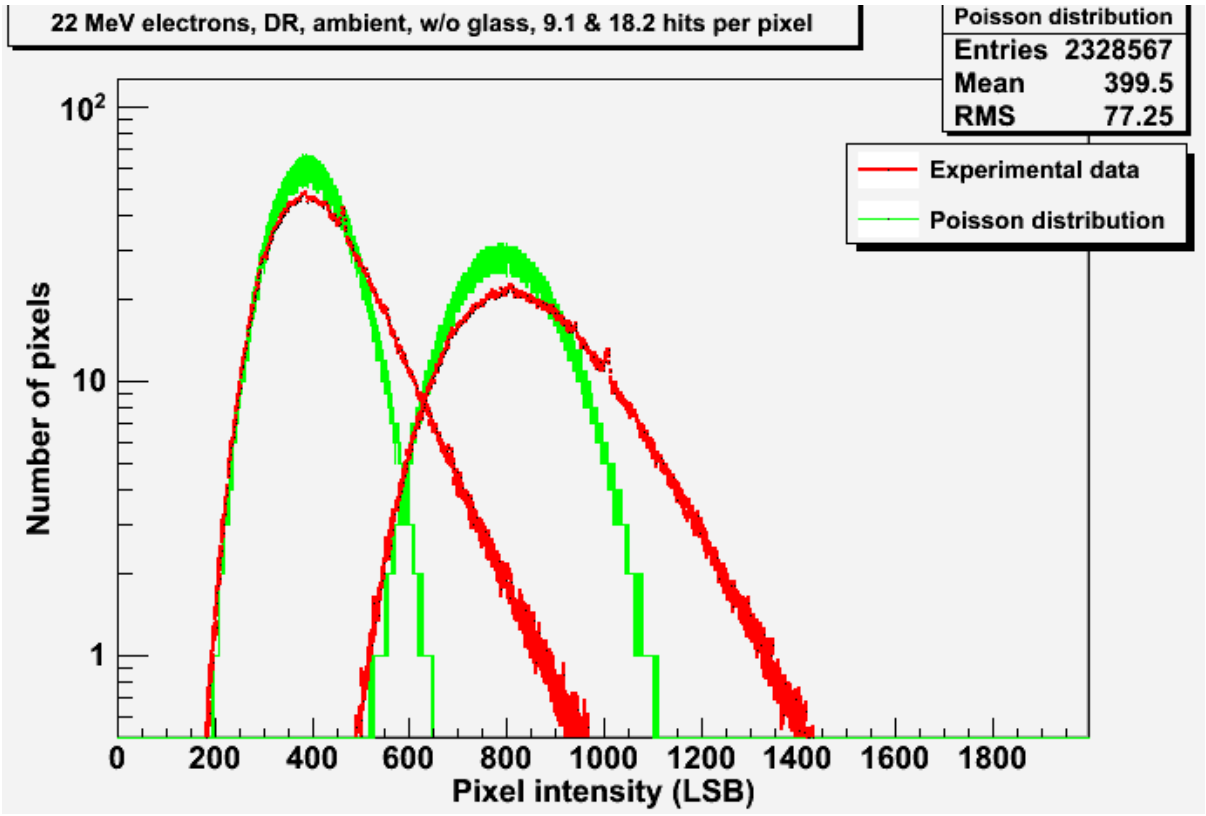

Figure 7-25: Mean electron single pulse and double pulse distributions at 22 MeV, 1000 UM/min, normal incidence compared to theoretical Poisson distributions

7.3.3.1.6.Run 34: 12 MeV electrons, 100 UM/min, 28.2° tilt, 19°C

Analysis parameters:

- mean number of hits: 7.2 per pixel
- signal at distribution peak: 324 LSB
- corresponding signal per electron: 45 LSB
- corresponding charge collection thickness: 6.96 µm

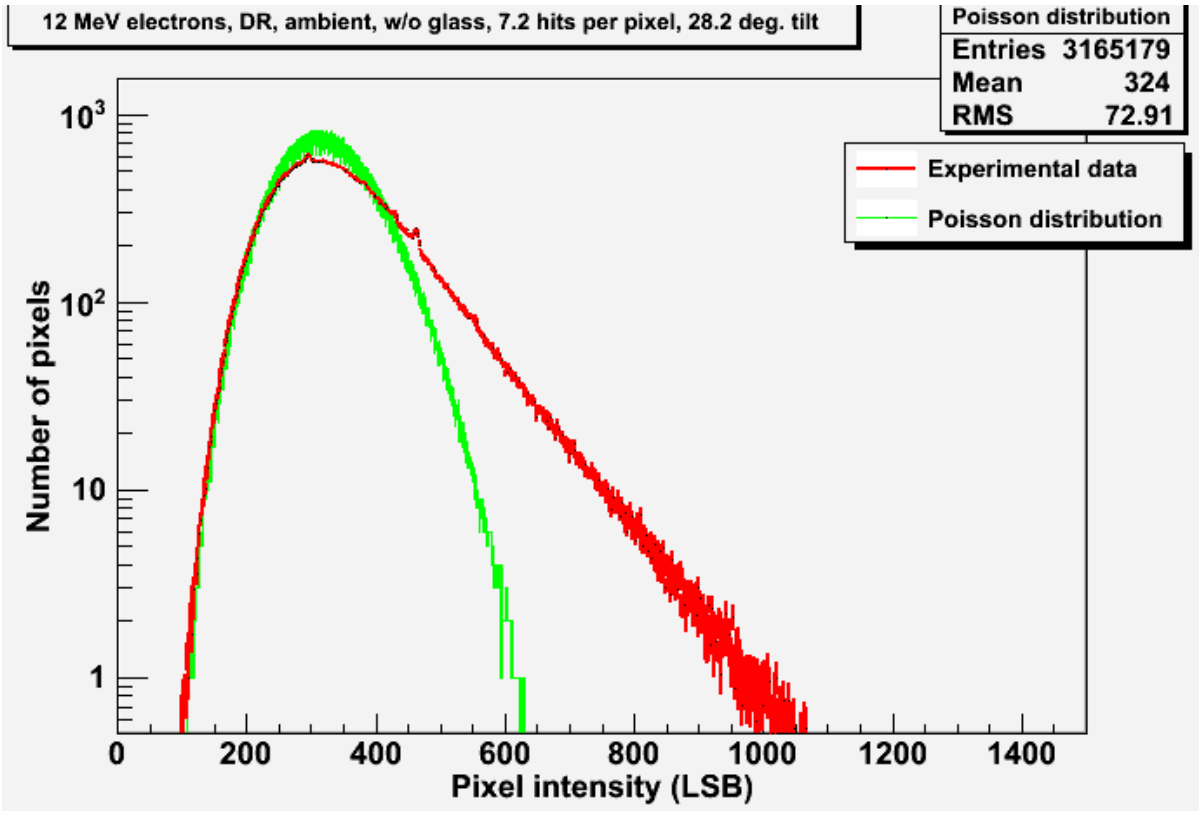

Figure 7-26: Mean electron pulse distribution at 12 MeV, 100 UM/min, 28.2° tilt compared to theoretical Poisson distribution

7.3.3.1.7.Run 37: 22 MeV electrons, 100 UM/min, 28.2° tilt, 19°C

Analysis parameters:

- mean number of hits: 7.77 per pixel
- signal at distribution peak: 380.8 LSB
- corresponding signal per electron: 49 LSB
- corresponding charge collection thickness: 7.20 µm

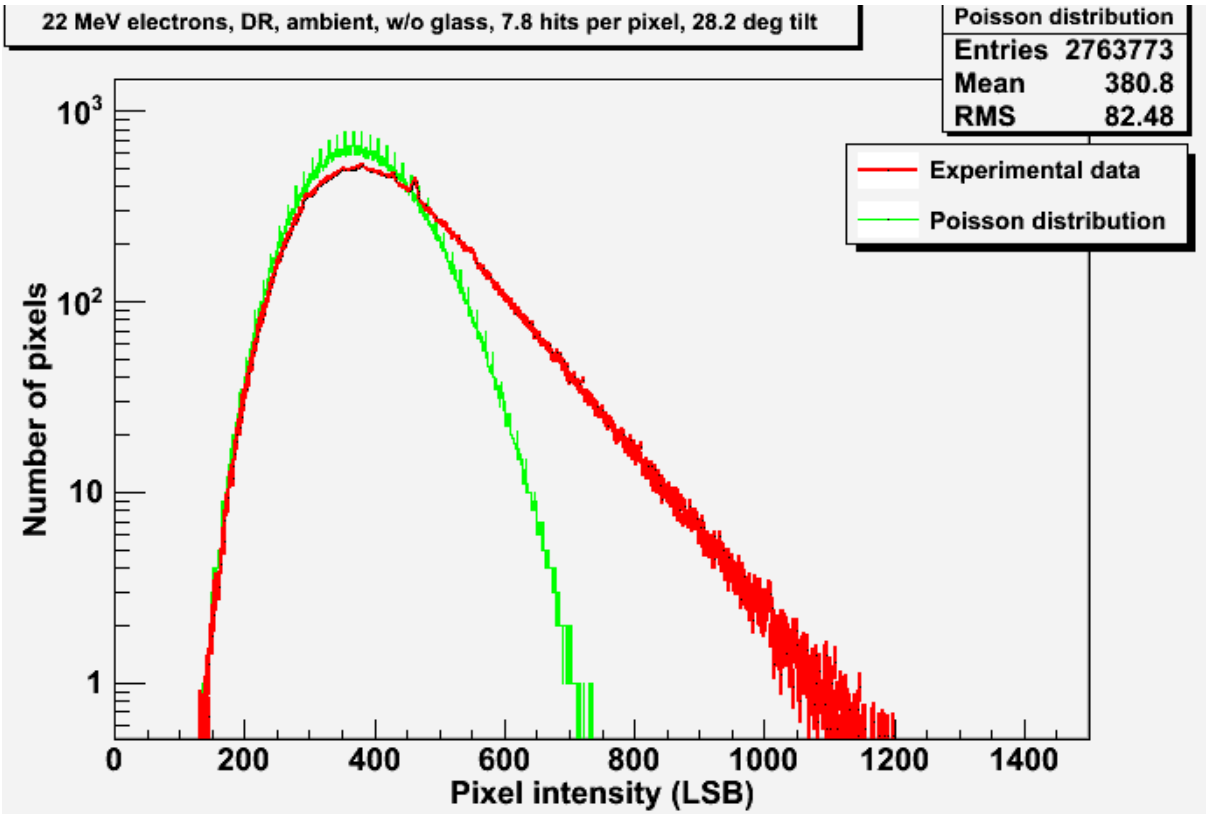

Figure 7-27: Mean electron pulse distribution at 22 MeV, 100 UM/min, 28.2° tilt compared to theoretical Poisson distribution

7.3.3.1.8.Run 38: 12 MeV electrons, 1000 UM/min, 28.2° tilt, 19°C

Analysis parameters:

- mean number of hits: 7.61 (1x), 15.22 (2x)
- signal at distribution peak: 333.7 LSB (1x), 667.4 LSB (2x)
- corresponding signal per electron: 44 LSB
- corresponding charge collection thickness: 6.80 µm

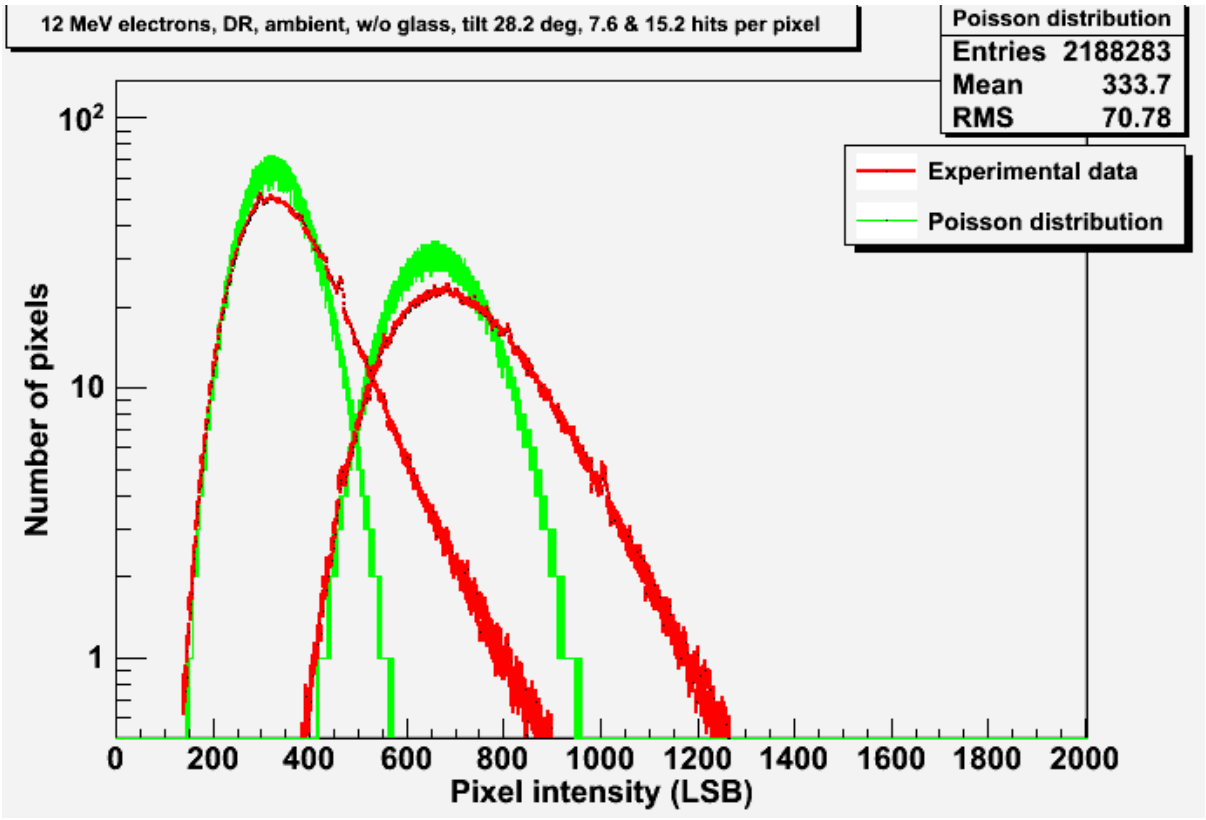

Figure 7-28: Mean electron single pulse and double pulse distributions at 12 MeV, 1000 UM/min, 28.2° tilt compared to theoretical Poisson distributions

7.3.3.1.9.Run 39: 22 MeV electrons, 1000 UM/min, 28.2° tilt, 19°C

Analysis parameters:

- mean number of hits: 8.0 (1x), 16.0 (2x)
- signal at distribution peak: 383 LSB (1x), 766 LSB (2x)
- corresponding signal per electron: 45 LSB
- corresponding charge collection thickness:

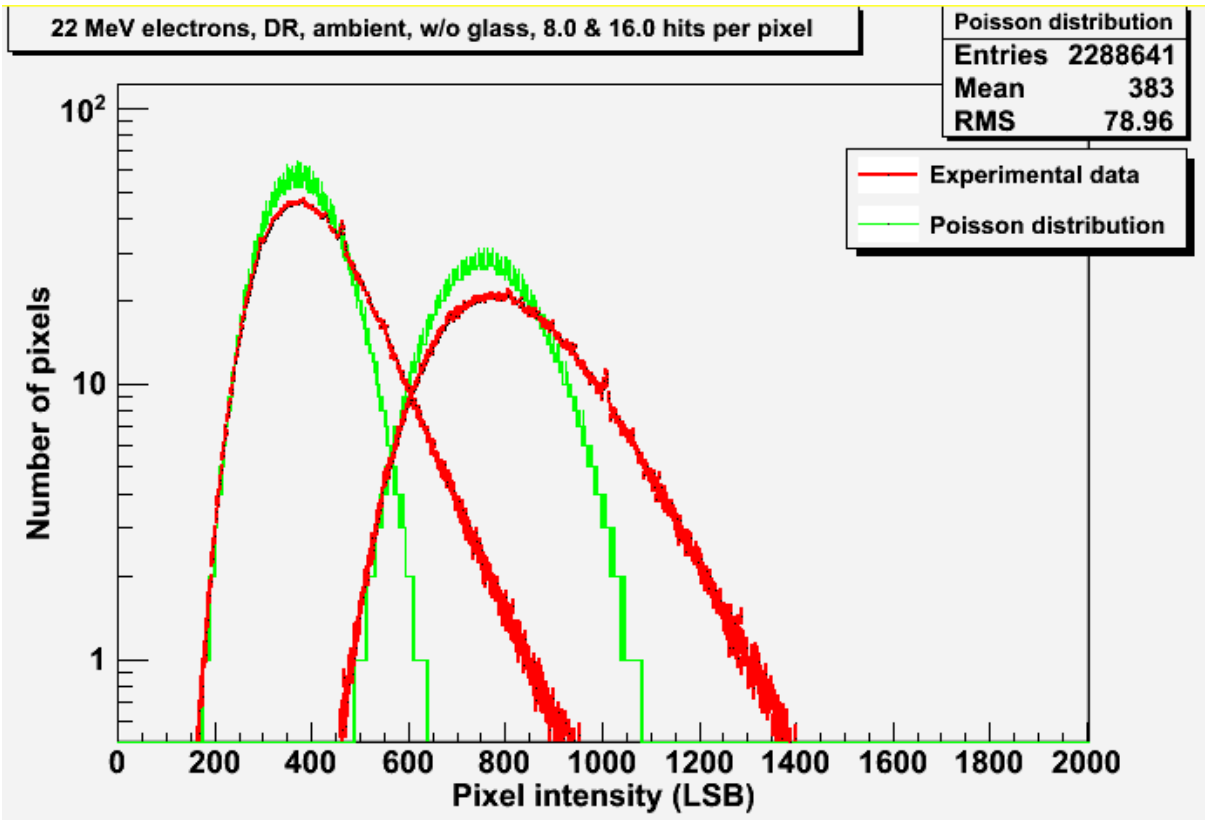

Figure 7-29: Mean electron single pulse and double pulse distributions at 22 MeV, 100 UM/min, 28.2° tilt compared to theoretical Poisson distributions

7.3.3.2.Conclusions

The results of the Poisson analysis are summarized in Table 7-5. The peak signal and corresponding charge collection layer thickness are computed for every DR run. For tilted runs, the charge collection layer thickness has been simply corrected by the cosine-angle factor, so that:

$$t = \frac{S}{X} \times \cos(\theta)$$

In which S is the peak signal, X is the number of hits per pulse, and θ is the beam angle of incidence.

	Dose rate	Energy	Tilt	Hits per pulse	Peak signal	Thickness
RUN 28	100 UM/min	12 MeV	0°	8.14 e-/pixel	317.4 LSB	6.84 µm
RUN 31	100 UM/min	22 MeV	0°	8.82 e-/pixel	379.3 LSB	7.17 µm
RUN 32	1000 UM/min	12 MeV	0°	8.64 e-/pixel	343.4 LSB	7.02 µm
RUN 33	1000 UM/min	22 MeV	0°	9.10 e-/pixel	399.5 LSB	7.33 µm
RUN 34	100 UM/min	12 MeV	28.2°	7.17 e-/pixel	324.0 LSB	6.96 µm
RUN 37	100 UM/min	22 MeV	28.2°	7.77 e-/pixel	380.8 LSB	7.20 µm
RUN 38	1000 UM/min	12 MeV	28.2°	7.61 e-/pixel	333.7 LSB	6.80 µm
RUN 39	1000 UM/min	22 MeV	28.2°	8.02 e-/pixel	383.0 LSB	7.05 µm
Mean 12 MeV						6.91 µm
Mean 22 MeV						7.19 µm
Mean						7.05 µm

Table 7-4: Summary of the Poisson analysis results

The Poisson analysis shows that the charge collection layer of the HAS2 is 7.05 µm thick. 12 MeV and 22 MeV results are consistent, with less than ±3% of variation between the two energies.

This is the thickness which should be used when modelling the charge deposition process as a linear energy loss along a straight path. However, the theoretical distribution shapes show a bad match with the experimental ones, which is particularly salient when the distributions are plotted on a linear scale.

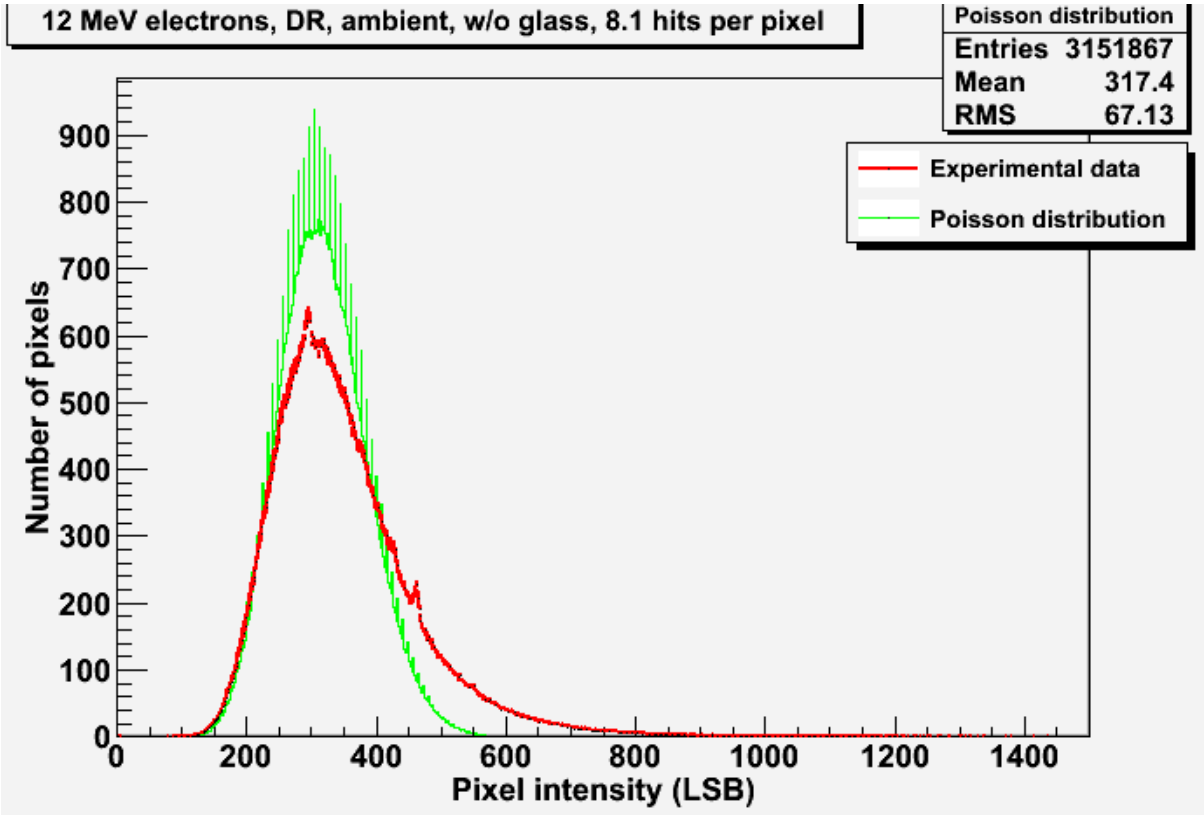

Figure 7-30: Mean electron pulse distribution at 12 MeV, 100 UM/min, normal incidence compared to theoretical Poisson distribution on a linear scale (RUN 28)

7.3.3.3.Straggling with diffusion

7.3.3.3.1.Data analysis overview

A more accurate analysis can be performed by taking into account particle-to-particle energy deposition variation (straggling process). The physics and modelling of the straggling process has been described in detail in [RD 2]. For this analysis, we use the same model as presented in the reference document. The inputs needed to generate a theoretical straggling distribution are:

- the incident electrons energy (known from CLINAC 1 settings),
- the average number of electron hits per pixel (computed in section 7.3.1),
- the number of exposed pixels (linked to integration time, section 5.2.2),
- the path length in the charge collection layer thickness of the sensor.

Once the distribution is generated, the inter-pixel diffusion pattern from section 7.3.3.1 is applied.

The only unknown parameter is the charge collection layer thickness, which will be assessed by fitting the theoretical distributions to the experimental ones presented in section 7.3.2. For tilted runs, the path length p has been simply corrected by the cosine-angle factor, so that:

$$p = {}^{t}\!/_{\cos(\theta)}$$

7.3.3.3.2.Run 28: 12 MeV electrons, 100 UM/min, normal incidence, 19°C

Analysis parameters:

- mean number of hits: 8.1 hits per pixel
- mean signal: 359.5 LSB
- mean charge collection layer thickness: 9.75 µm

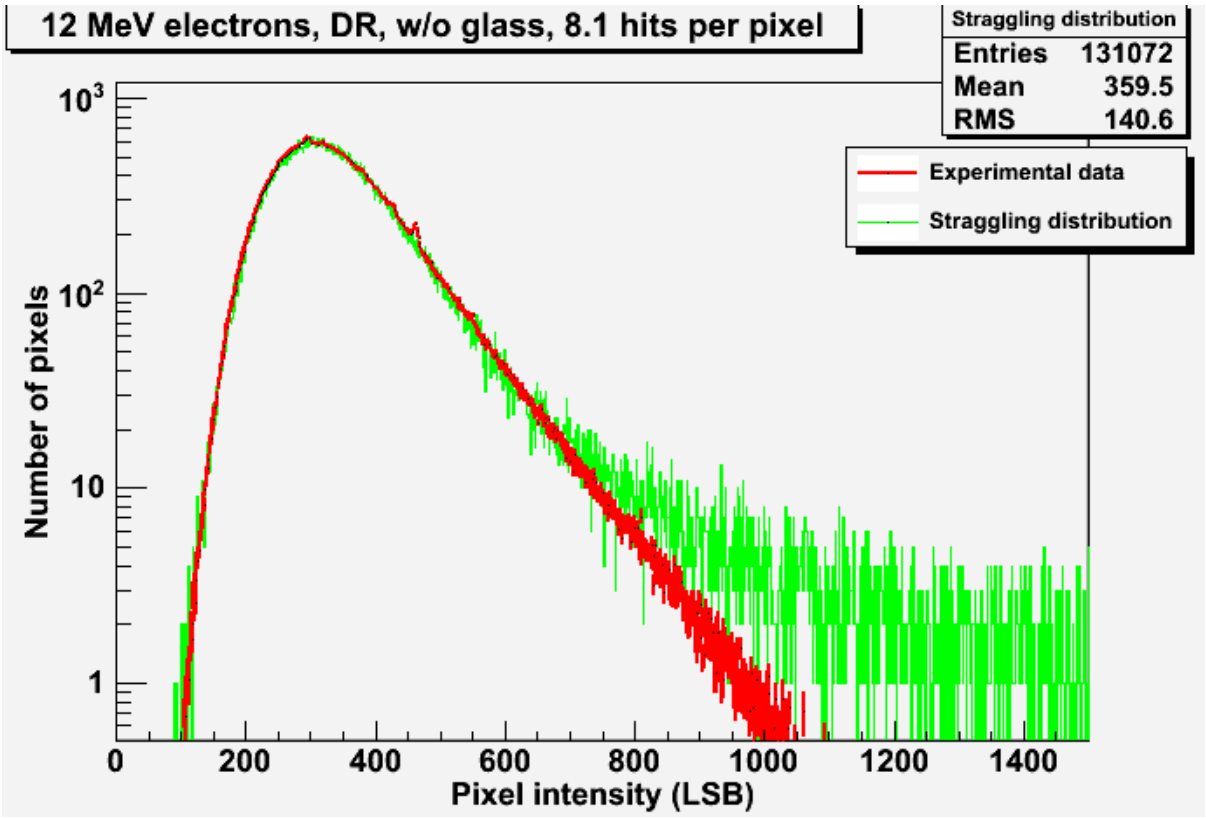

Figure 7-31: Mean electron pulse distribution at 12 MeV, 100 UM/min, normal incidence compared to theoretical straggling distribution

7.3.3.3.3.Run 31: 22 MeV electrons, 100 UM/min, normal incidence, 19°C

Analysis parameters:

- mean number of hits: 8.8 per pixel
- mean signal: 424.1 LSB
- mean charge collection layer thickness: 10.5 µm

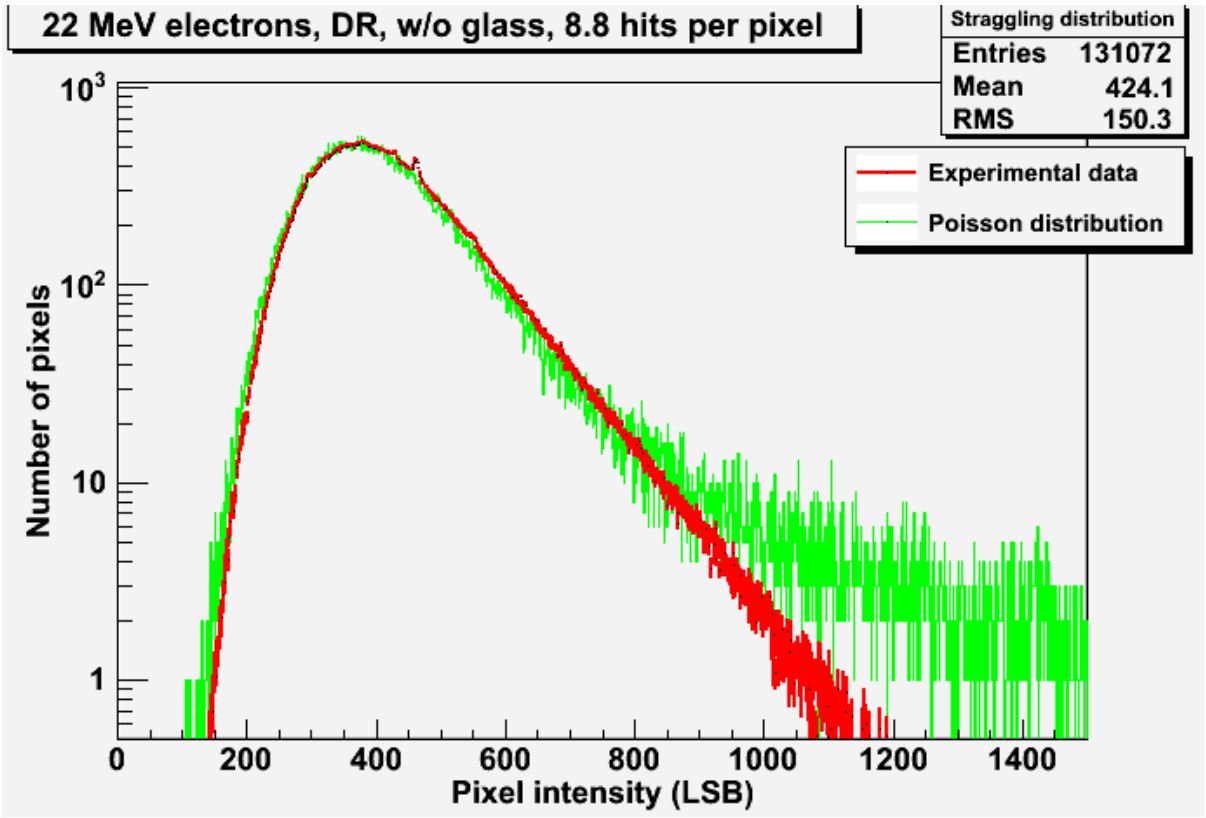

Figure 7-32: Mean electron pulse distribution at 22 MeV, 100 UM/min, normal incidence compared to theoretical straggling distribution

7.3.3.3.4.Run 34: 12 MeV electrons, 100 UM/min, 28.2° tilt, 19°C

Analysis parameters:

- mean number of hits: 7.2 per pixel
- mean signal: 320.4 LSB
- mean charge collection layer thickness: 10.25 µm

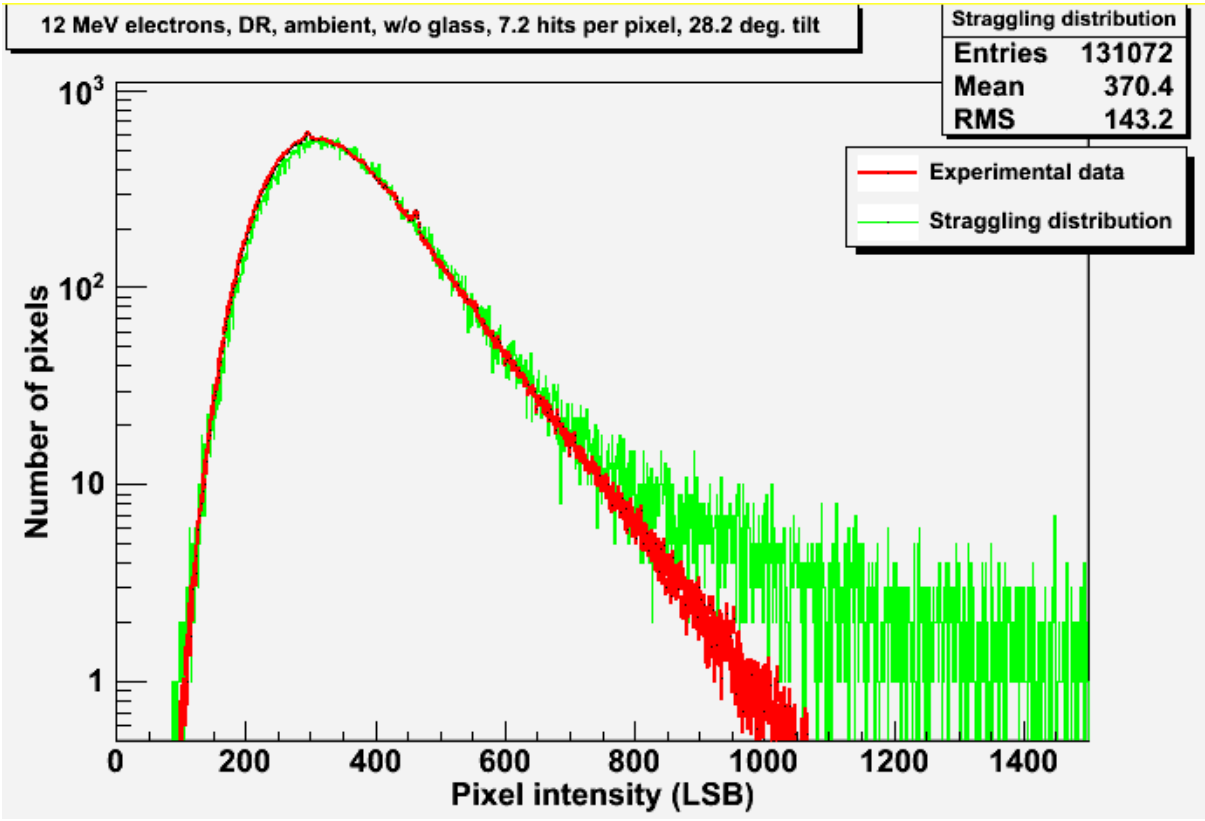

Figure 7-33: Mean electron pulse distribution at 12 MeV, 100 UM/min, 28.2° tilt compared to theoretical straggling distribution

7.3.3.3.5.Run 37: 22 MeV electrons, 100 UM/min, 28.2° tilt, 19°C

Analysis parameters:

- mean number of hits: 7.77 per pixel
- signal at distribution peak:
- corresponding charge collection thickness:

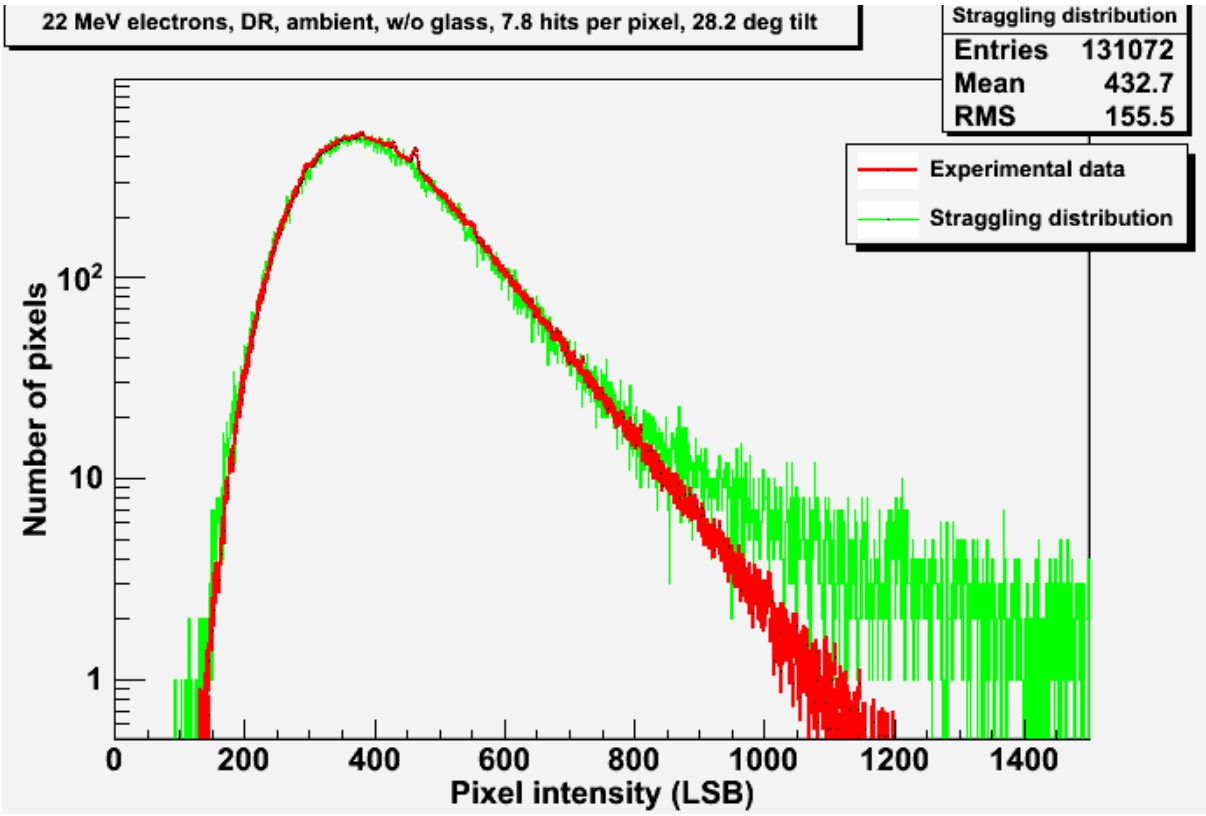

Figure 7-34: Mean electron pulse distribution at 22 MeV, 100 UM/min, 28.2° tilt compared to theoretical straggling distribution

7.3.3.3.6.Conclusions

The results of the straggling analysis are summarized in Table 7-5.

	Dose rate	Energy	Tilt	Hits per pulse	Collection thickness
RUN 28	100 UM/min	12 MeV	0°	8.14 e-/pixel	9.75 µm
RUN 31	100 UM/min	22 MeV	0°	8.82 e-/pixel	10.50 µm
RUN 34	100 UM/min	12 MeV	28.2°	7.17 e-/pixel	9.75 µm
RUN 37	100 UM/min	22 MeV	28.2°	7.77 e-/pixel	10.75 µm
Mean 12 MeV					9.75 µm
Mean 22 MeV					10.625 µm
Mean					10.19 µm

Table 7-5: Summary of the straggling analysis results

The straggling analysis shows that the charge collection layer of the HAS2 is 10.19 µm thick. 12 MeV and 22 MeV results are consistent, with less than ±4.5% of variation between the two energies.

A significant difference is found with the results of the Poisson analysis in 7.3.3.1, for which the charge collection layer thickness was found to be 7.05 µm thick. This inconsistency is explained in the following way: on one hand, the Poisson analysis was performed by fitting the peaks of the experimental and theoretical distributions. The thickness computed in the previous section is effectively corresponding to the most probable energy loss of incident particles. On the other hand, the straggling analysis was made by fitting the whole distribution. The thickness computed in this section effectively corresponds to the mean energy loss of incident particles, and should be considered as more accurate. More information on the differences between the mean energy loss and most probable energy loss can be found in [RD 2].

Finally, the match between the shape of theoretical and experimental distributions is very good. The distributions perfectly fit on two decades, until small discrepancies appear for high pixel intensity values. The theoretical distribution tails systematically overshoot the experimental ones, leading to a slightly worst-case modelling. When plotted on a linear scale, the theoretical distributions are virtually indistinguishable from the experimental ones.

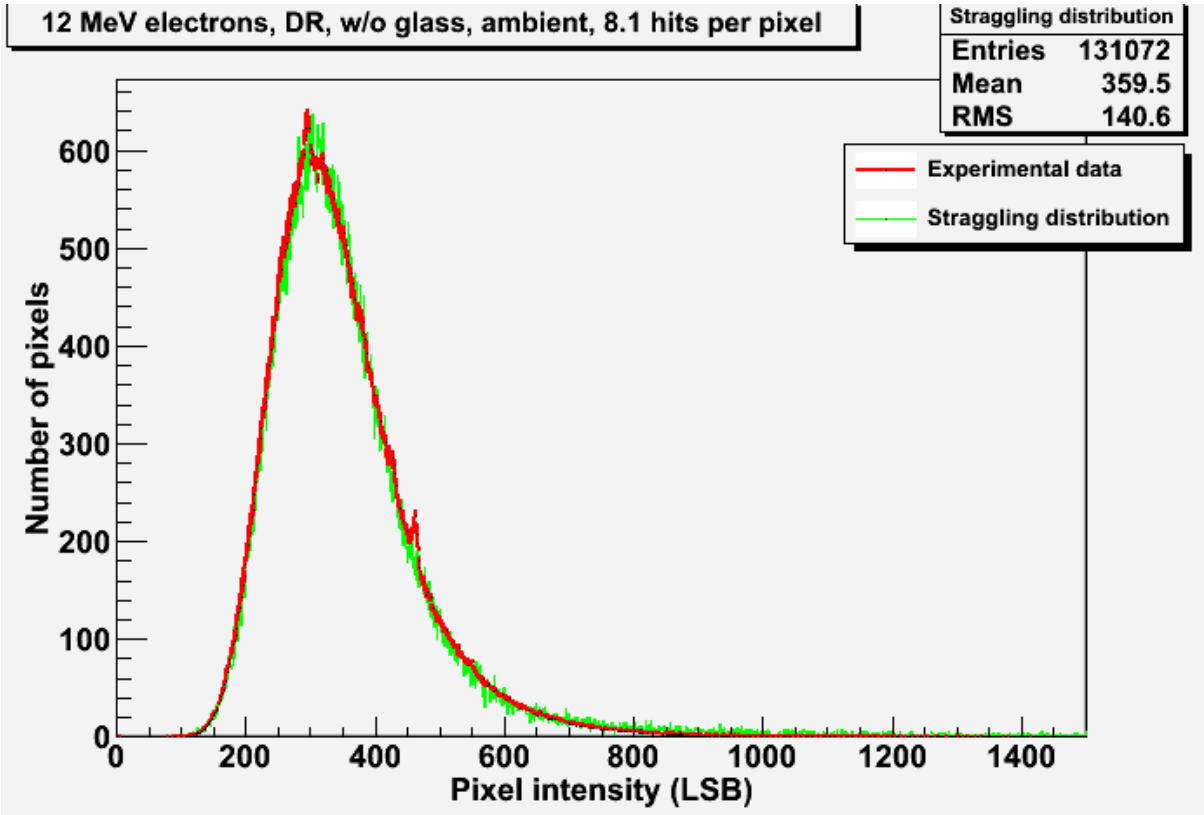

Figure 7-35: Mean electron pulse distribution at 12 MeV, 100 UM/min, normal incidence compared to theoretical straggling distribution on a lin. scale (RUN 28)

7.3.3.4.Monte-Carlo with diffusion

7.3.3.4.1.Data analysis overview

An additional analysis can be performed with direct Monte-Carlo simulation, which can be used to compute the deposited energy in each pixel of the sensor. The simulations have been performed with GEANT4 standard electromagnetic physics in collaboration with TRAD. They are considered as the most accurate analysis method of this test report.

As shown on Figure 7-36, the HAS2 has been modelled along with a simple model representative of the test bench. This model included the plastic socket, the epoxy PCB and the aluminium housing. The HAS2 itself has been modelled in great detail. The metal and passivation layers of each pixel have been taken into account according to Figure 7-37 and Figure 7-38.

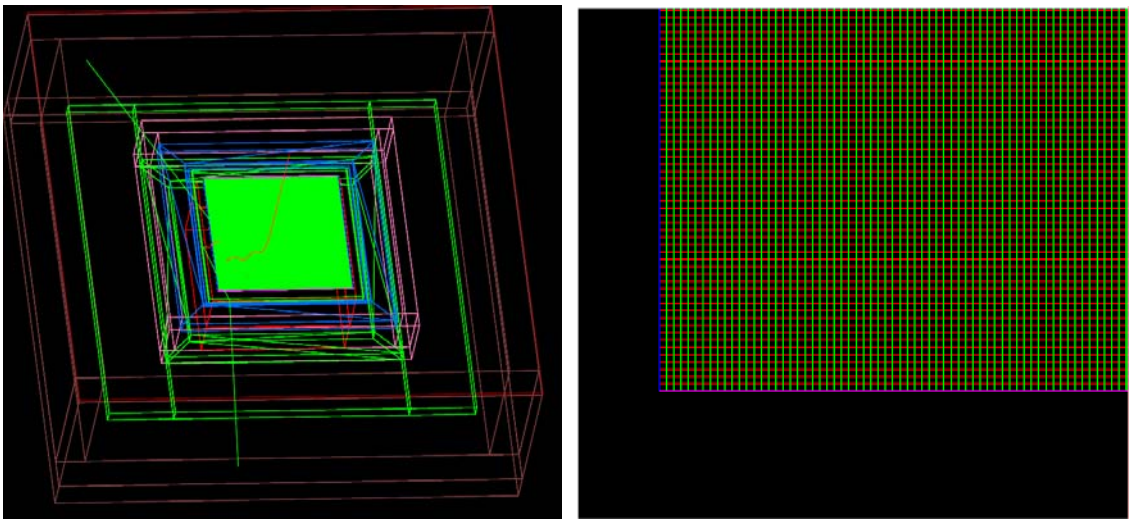

Figure 7-36: GEANT4 modeling of the HAS2 and of the test bench (left), detail of the metal and passivation layers of the HAS2 model (right)

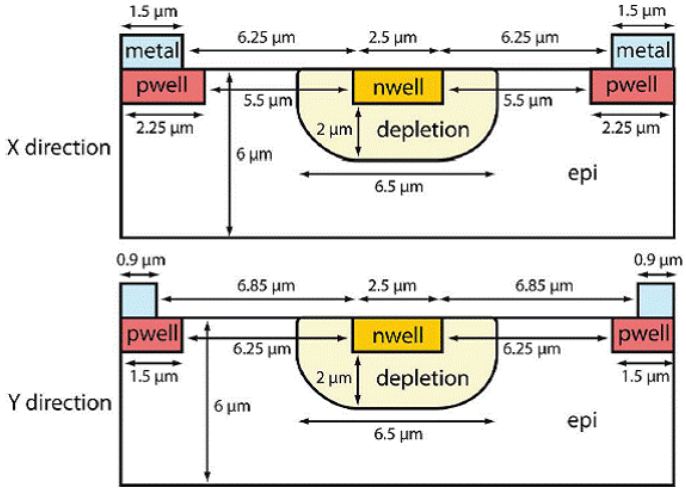

Figure 7-37: HAS2 pixel lateral dimensions

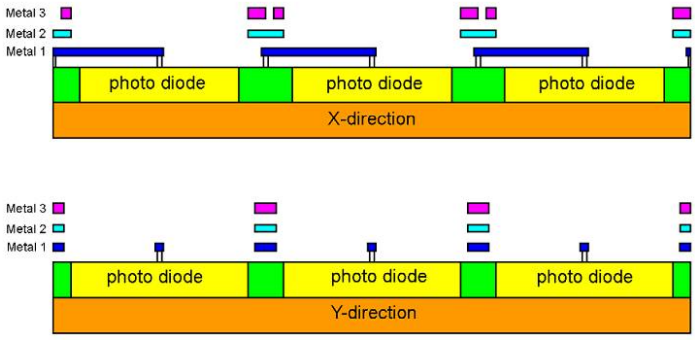

Description	value
distance silicium – metal 1	0.94 um
height metal 1	0.64 um
distance metal 1 – metal 2	0.95 um
height metal 2	0.61 um
distance metal 2 – metal 3	0.95 um
Height metal 3	0.89 um

Figure 7-38: HAS2 metal and passivation layers characteristics. The passivation layer is considered to extend up to 1 µm above the metal 3 layer.

The sensor expositions have been simulated by a mono-energetic and uniform beam, with a 1:1 correspondence between the number of fired particles and the number of electrons expected during a pulse. The output of the simulation is a 2D energy distribution map reporting the energy lost by primary electrons and secondary particles in each pixel. The contributions of primary and secondary particles can be precisely told apart.

The energy deposition maps have been converted to generated charge maps by considering the average electron-hole pair creation energy of 3.6 eV.

Finally, once the charge deposition maps have been computed, the inter-pixel diffusion pattern from section 7.3.3.1 is applied.

The simulations are time-consuming (about 8 hours for each run). In consequence, they have only been performed on a limited number of test cases.

7.3.3.4.2.Run 28: 12 MeV electrons, 100 UM/min, normal incidence

Analysis parameters:

- mean number of hits: 8.1 hits per pixel
- mean signal: 356.8 LSB
- simulated charge collection layer thickness: 9 µm

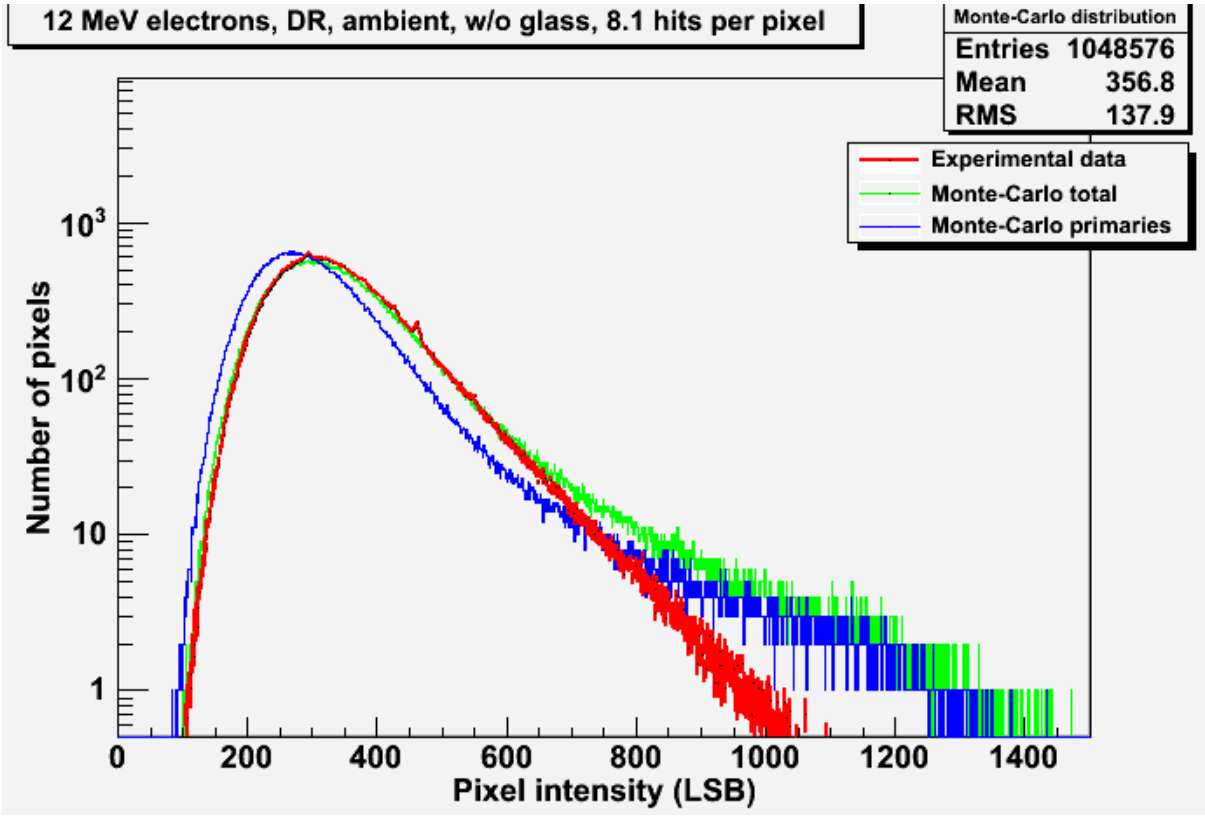

Figure 7-39: Mean electron pulse distribution at 12 MeV, 100 UM/min, normal incidence compared to Monte-Carlo computed distribution

7.3.3.4.3.Run 31: 22 MeV electrons, 100 UM/min, normal incidence

Analysis parameters:

- mean number of hits: 8.8 per pixel
- mean signal: 444.7 LSB
- simulated charge collection layer thickness: 10 µm

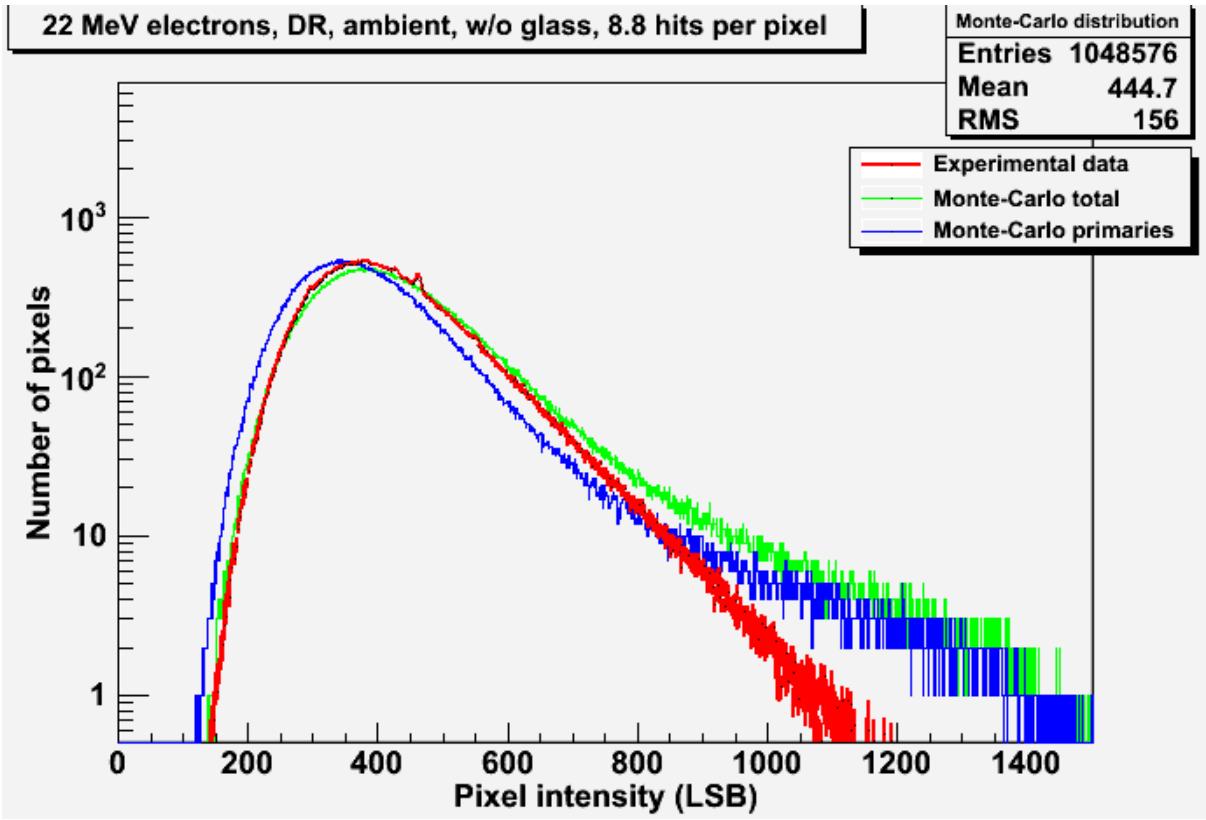

Figure 7-40: Mean electron pulse distribution at 22 MeV, 100 UM/min, normal incidence compared to Monte-Carlo computed distribution

7.3.3.4.4.Conclusions

The Monte-Carlo simulations on a detailed model sensor give very similar results to the straggling analysis performed in section 7.3.3.3. The charge collection layer thickness is shown to be close to 9.5 µm, which is slightly lower than the 10.2 µm figure found previously. Most of the signal is generated from the interaction of primary electrons.

Once again, the match between the shape of theoretical and experimental distributions is good, as shown on Figure 7-41. Just like in section 7.3.3.3, the simulated distribution tails systematically overshoot the experimental ones. In this respect, the Monte-Carlo analysis does not appear to give significant advantage over the straggling analysis. When plotted on a linear scale, the simulated distributions are very close to the experimental ones.

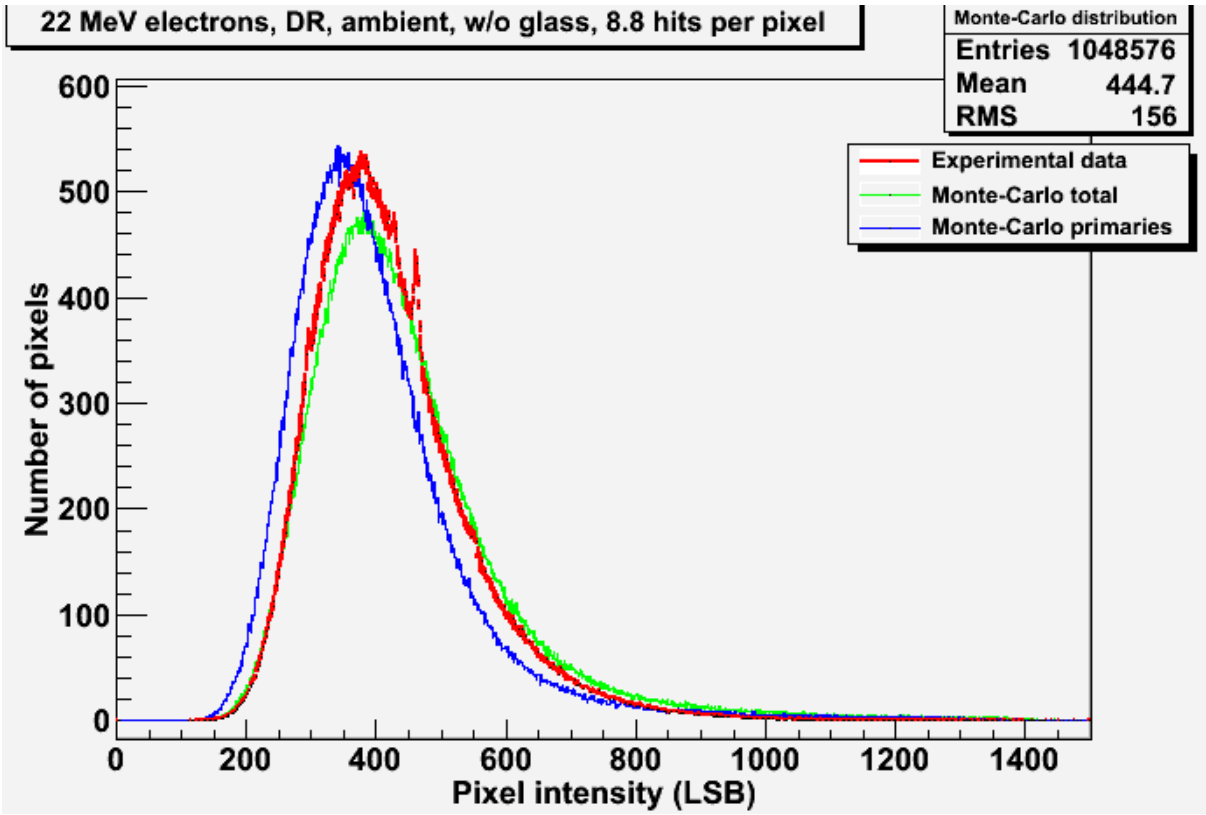

Figure 7-41: Mean electron pulse distribution at 22 MeV, 100 UM/min, normal incidence compared to computed Monte-Carlo distribution on a lin. scale (RUN 28)

7.4.Secondary photonic effects

7.4.1.Methodology

Fast charged particles such as electrons can generate light as they cross optical materials. The secondary photons can disturb the measurements of the star tracker. Two main processes are causing this phenomenon:

- Čerenkov effect, a photonic shockwave created by a charged particle exceeding the speed of light in the considered medium,
- Luminescence effect, the reemission of absorbed ionizing radiation energy as light.

These effects have been reviewed in detail in [RD 3].

To characterize these secondary photonic effects, two modifications have been made to the baseline test set-up described in section 5.3:

- The sensors are tested with a 1.5 mm thick specific window in silica. On the underside of the window, a metallic mask has been deposited, which effectively covers half of the focal plane array. This area is therefore shielded from optical photons generated in the window. The metallic mask is grounded to avoid any charging effect under beam. Two wedges of kapton are sandwiched between the sensor die and the window.
- An additional 8 mm thick sample of silica is added on top of the detector, in order to enhance the secondary photonic signal.

This specific set-up is presented in Figure 7-42 and Figure 7-43.

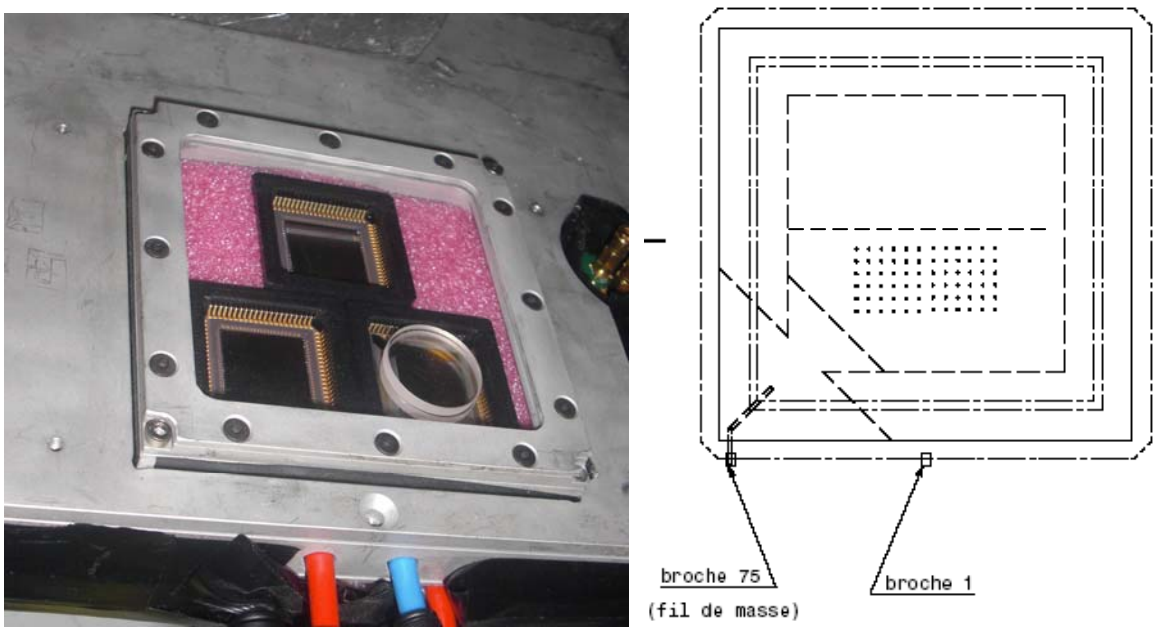

Figure 7-42: Experimental set-up with 9.5 mm of silica on the detector (left), overview of the optical mask (right)

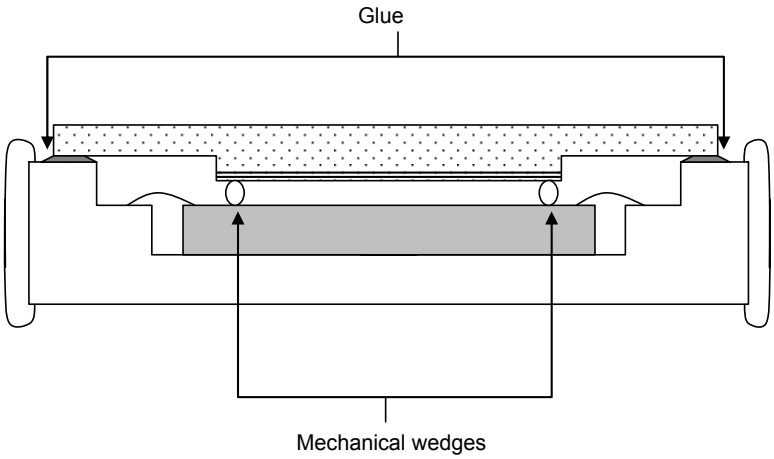

Figure 7-43: Cross-section of the specific window

The analysis is performed in the following way: two analysis zones are defined on the sensor, a masked zone and a clear zone, as presented in Figure 7-44. The clear zone will be exposed to direct ionization from electrons, and to secondary photons generated in the window. The masked zone will be only exposed to electron direct ionization. The difference between the signals of these two zones will give a measurement of the secondary photonic effects.

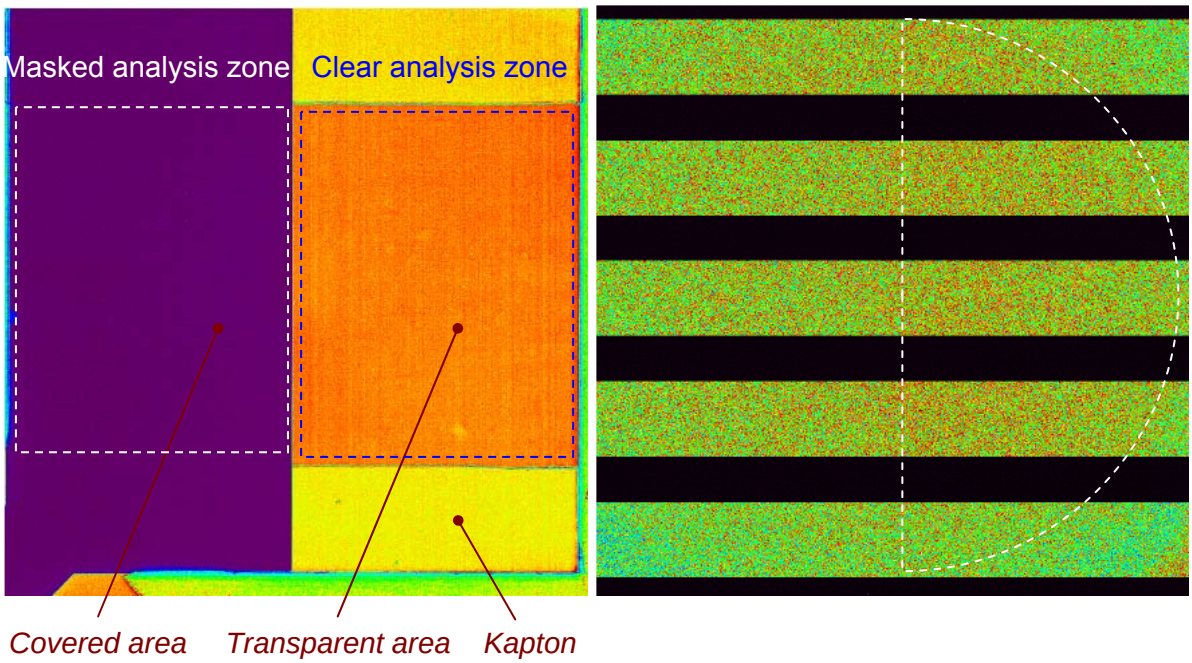

Figure 7-44: image under light showing the covered and transparent areas of the mask (left), image under beam showing a slight signal enhancement (right)

The electrons will go through the same amount of silica in both zones before reaching the sensor. The ionization-induced signal is therefore going to be the same. After 9.5 mm of silica, GEANT4 Monte-Carlo simulation shows that the electron energy falls down to:

- 8 MeV at die level for the 12 MeV electron beam.
- 18 MeV at die level for the 22 MeV electron beam.

Several corrections are made to ensure that the calculation of photonic signal is correct. For each run, DR electrical offset and FPN was subtracted using the averaged values of pixel to pixel offsets from the final images of the run (recorded while the beam was turned off). The averaging is typically performed on 10 frames, which leads to a residual noise on the FPN image of ~1.3 LSB.

In each analysis zone, the pulse signal S_{pulse} and the reference signal S_{ref} in between the pulses is computed. The pulse signal and reference signals are averaged on 20 frames of the run.

The formula used to compute the photonic signal per pulse after FPN correction is:

$$S_{diff} = \left(S_{pulse}^{clear} - S_{ref}^{clear}\right) - \left(S_{pulse}^{masked} - S_{ref}^{masked}\right)$$

Finally, the beam spatial non-uniformity must be taken into account. As stated in [AD 1], the beam intensity shows a slight decrease towards its external radius, which corresponds to the clear area of the metallic mask. In order to assess this non-uniformity, the analysis presented above has been performed on runs recorded on bare sensors, in the same CLINAC 1 configuration. The effective photonic signal with beam non-uniformity bias suppressed is given by:

$$S_{photon} = S_{diff}^{window} - S_{diff}^{bare}$$

These runs on bare sensors have been performed at the start of the cumulative effects campaign.

7.4.2.Order of magnitude of the expected signal

To assess the number of optical photons generated by the beam in the silica, we use the methods presented in [RD 3]. The computation is performed independently for the Čerenkov and luminescence effects.

For the Čerenkov process, the mean energy of incident electrons in silica is considered: 10 MeV for the 12 MeV beam, and 20 MeV for the 22 MeV beam. The following parameters are used to compute the generated photonic signal:

- thickness of silica sample: 9.5 mm
- refractive index of silica: 1.5
- lateral dimensions of the silica sample: 26.8 x 26.8 mm²
- distance between die and silica sample: 80 µm
- spectral bandwidth: from 400 to 900 nm

The simplified Čerenkov formula of [RD 3] is:

$$\beta(E) = \sqrt{1 - \frac{1}{\left(\frac{E}{mc^2} + 1\right)^2}}$$

$$N = 2\pi \cdot \alpha \cdot \left(\frac{1}{\lambda \min} - \frac{1}{\lambda \max} \right) \cdot \left(1 - \frac{1}{n^2 \beta^2} \right) \cdot x \cdot \Phi$$

In which β is the reduced velocity, E is the electron energy, c is the speed of light, α is the fine structure constant, n is the index of the medium, m is the electron mass, x is the path length in the medium and λ is the wavelength.

The results are presented in Table 7-6. The "generated photons" entry gives the fluence of photons generated in the silica per pulse. The "detected photons", gives the number of photons that reach effectively reach the detector and are collected as signal, taking into account the geometry of the set-up, and the quantum efficiency and fill factor of the sensor.

	Dose rate	Energy	Tilt	Fluence per pulse	Generated photons per pulse	Detected photons per pulse
RUN 22	100 UM/min	12 MeV	0°	2.51E6 e-/cm²	8.39E8 ph/cm²	242 ph/pixel
RUN 25	100 UM/min	22 MeV	0°	2.72E6 e-/cm²	9.14E8 ph/cm²	264 ph/pixel

Table 7-6: Estimation of the number of generated Čerenkov photons

For luminescence, the following parameters are used to compute the mean photonic signal:

- thickness of silica sample: 9.5 mm
- density of silica : 2.5 g/cm^3
- lateral dimensions of the silica sample: 26.8 x 26.8 mm²
- distance between die and silica sample: 80 µm
- spectral bandwidth: from 400 to 900 nm

As in [RD 3], the simplified luminescence formula is:

$$M = V \cdot \rho$$

$$N = D \cdot M \cdot K \cdot \left(\lambda_{\max} - \lambda_{\min} \right)$$

In which D is the deposited dose, M is the mass of the sample, V is the volume of the sample, ρ is the density of the medium, λ is the wavelength and K is the luminescence conversion factor of 50 photons/(MeV.nm).

The results are presented in Table 7-7. The "generated photons" entry gives the fluence of photons generated in the silica per pulse. The "detected photons", gives the number of photons that reach effectively reach the detector and are collected as signal, taking into account the geometry of the set-up, and the quantum efficiency and fill factor of the sensor.

	Dose rate	Energy	Tilt	Energy per pulse	Generated photons per pulse	Detected photons per pulse
RUN 22	100 UM/min	12 MeV	0°	100 TeV	3.13E9 ph/cm²	836 ph/pixel
RUN 25	100 UM/min	22 MeV	0°	106 TeV	3.33E9 ph/cm²	889 ph/pixel

Table 7-7: Estimation of the number of generated luminescence photons

The estimation of the total photonic flux including Čerenkov and luminescence effects is given in Table 7-9:

	Dose rate	Energy	Tilt	Fluence per pulse	Generated photons per pulse	Detected photons per pulse
RUN 22	100 UM/min	12 MeV	0°	2.51E6 e-/cm²	3.96E9 ph/cm²	1078 ph/pixel
RUN 25	100 UM/min	22 MeV	0°	2.72E6 e-/cm²	4.24E9 ph/cm²	1153 ph/pixel

Table 7-8: Estimation of the number of generated luminescence photons

7.4.3.Experimental data and analysis

The methodology presented in section 7.4.3 has been applied to 12 MeV and 22 MeV runs at 100 UM/min, normal incidence. The difference of signal per pulse S_{diff} between the clear zone and the masked zone has been computed in Table 7-9. Runs 22 and 25 were the only ones during which the sensors were behind 9.5 mm of silica.

	Dose rate	Energy	Tilt	Config.	Hits per pulse	Clear – masked signal
RUN 22	100 UM/min	12 MeV	0°	Window	8.14 e-/pixel	16.8 LSB/pulse
RUN 25	100 UM/min	22 MeV	0°	Window	8.82 e-/pixel	13.8 LSB/pulse
RUN TID_3	100 UM/min	12 MeV	0°	Bare	8.14 e-/pixel	-6.4 LSB/pulse
RUN TID_4	100 UM/min	22 MeV	0°	Bare	8.82 e-/pixel	-7.9 LSB/pulse

Table 7-9: Summary of the secondary photonic effects analysis

Runs TID_3 and TID_4 were performed with the bare sensors. These runs allow us to take into account the beam spatial non-uniformity.
With this correction applied, the secondary photons induced signal for the 12 MeV beam (10 MeV in silica) is: 16.8 + 6.4 = 23.2 LSB, or 464 detected photons/pulse.

For the 22 MeV beam (20 MeV in silica), the corresponding signal is: 16.8 + 7.9 = 21.7 LSB, or 434 detected photons/pulse.

The measured signal is roughly a factor two under the estimation performed in section 7.4.2. The most probable explanation for this difference is an overestimation of the number of photons reaching the sensor, which has been computed using very basic photometry rules as stated in [RD 3].

8. CONCLUSIONS

The cumulative radiation test results are detailed in section 6.9. The gathered data are in line with radiation hardness properties of the HAS2 sensor. The most affected parameters are dark current and electrical offsets. Mean dark current and dark current non uniformities increase are in line with data obtained on previous wafer lot. A few additional hot pixels appear in the dark current histograms during irradiation meaning displacement damage contribution of the electron irradiation has a negligible effect on spike density. Odd/even offset in DR mode is sensitive to irradiation. A variation of 150 electrons is to be considered for EOL mission performances. Mean offsets drift observed in DR and NDR mode are without impact on STR application.

The SEE test results are detailed in section 7. The mean interaction thickness of 10 µm has been assessed through several configurations of test. A very good fit is observed between experimental data and theoretical distribution obtained through different methods of calculation. Figure 8-1 summarizes the improvement achieved by Straggling model distribution in comparison to Poisson distribution.

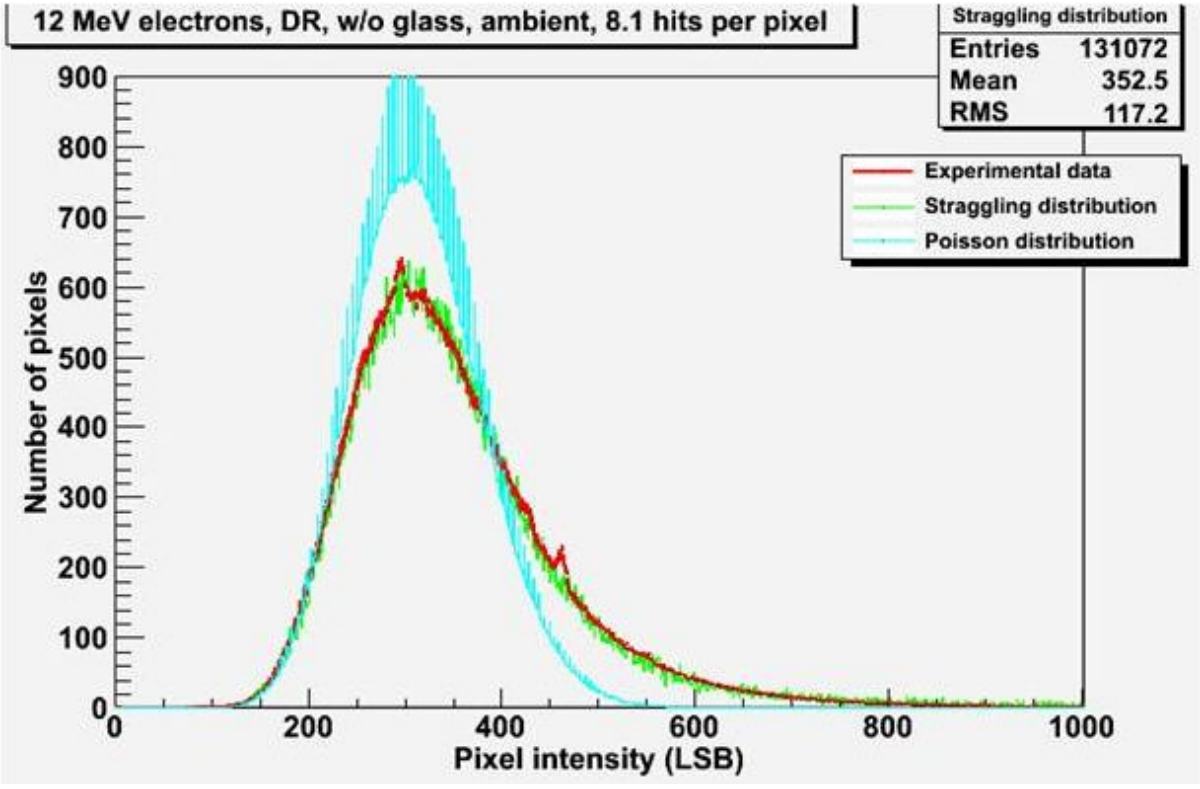

Figure 8-1: Mean electron pulse distribution at 12 MeV, normal incidence compared to theoretical Poisson and Straggling distribution on a linear scale

Secondary photonic effect has been also investigated showing a small discrepancy compared to theoretical expectation.